ISSN 1881-7831 Online ISSN 1881-784X

# DD&T

## Drug Discoveries & Therapeutics

Volume 20, Number 4
August 2026

IRCA BSSA

IACMHR

www.ddtjournal.com

DD&T
Drug Discoveries & Therapeutics

**ISSN:** 1881-7831
**Online ISSN:** 1881-784X
**CODEN:** DDTRBX
**Issues/Year:** 6
**Language:** English
**Publisher:** IACMHR Co., Ltd.

**Drug Discoveries & Therapeutics** is one of a series of peer-reviewed journals of the International Research and Cooperation Association for Bio & Socio-Sciences Advancement (IRCA-BSSA) Group. It is published bimonthly by the International Advancement Center for Medicine & Health Research Co., Ltd. (IACMHR Co., Ltd.) and supported by the IRCA-BSSA.

**Drug Discoveries & Therapeutics** publishes contributions in all fields of pharmaceutical and therapeutic research such as medicinal chemistry, pharmacology, pharmaceutical analysis, pharmaceutics, pharmaceutical administration, and experimental and clinical studies of effects, mechanisms, or uses of various treatments. Studies in drug-related fields such as biology, biochemistry, physiology, microbiology, and immunology are also within the scope of this journal.

**Drug Discoveries & Therapeutics** publishes Original Articles, Brief Reports, Reviews, Policy Forum articles, Case Reports, Communications, Editorials, News, and Letters on all aspects of the field of pharmaceutical research. All contributions should seek to promote international collaboration in pharmaceutical science.

# Editorial Board



## Editorial and Head Office:

Pearl City Koishikawa 603,
2-4-5 Kasuga, Bunkyo-ku,
Tokyo 112-0003, Japan
E-mail: office@ddtjournal.com

# Drug Discoveries & Therapeutics

## Editorial and Head Office

Pearl City Koishikawa 603, 2-4-5 Kasuga, Bunkyo-ku,
Tokyo 112-0003, Japan

E-mail: office@ddtjournal.com
URL: www.ddtjournal.com

# CONTENTS

*Volume 20, Number 4, 2026*

## Review



## Original Article



## Brief Report



## Correspondence

***Review***

DOI: 10.5582/ddt.2026.01042

# Advances in multimodal data integration for drug efficacy prediction: Methodological evolution and clinical translation

**Jingwen Fang[1], Zihan Wang[1], Junhao Shao[3], Jiewei Fan[1], Qichao Luo[2,*]**

[1] School of Health Management, Anhui Medical University, Hefei, Anhui, China;
[2] School of Pharmacy, Anhui Medical University, Hefei, Anhui, China;
[3] The Second Affiliated Hospital of Anhui Medical University, Hefei, Anhui, China.

**SUMMARY**: Drug efficacy prediction remains a cornerstone of drug development and precision therapy. However, integrating heterogeneous biomedical data, including multi-omics profiles, pathological imaging, electronic health records, and pharmacokinetic-pharmacodynamic (PK/PD) time-series, faces three fundamental barriers, namely cross-domain distribution shifts between preclinical and clinical data, relational mismatches between isolated vector representations and biological networks, and feature heterogeneity across disparate modalities. To address these challenges, three AI paradigms have emerged, transfer learning for cross-domain alignment, graph neural networks for structured relational modeling, and Transformers for global cross-modal feature interaction. Importantly, these techniques form a many-to-many complementary system rather than a one-to-one correspondence, a key insight that this review explicitly formalizes. We further elaborate encoding workflows for PK/PD data to bridge static molecular signatures with dynamic *in vivo* exposure trajectories. Four graded clinical applications are outlined, including personalized monotherapy, combination optimization, drug repurposing, and preclinical-to-clinical evaluation of novel candidates. We also dissect persistent bottlenecks such as data harmonization, model interpretability, and prospective validation, and propose five actionable directions, namely privacy-preserving benchmarks, causally interpretable models, temporal dynamic frameworks, cross-domain generalization, and lightweight clinical tools. By integrating theoretical rationales, methodological synergies, and hierarchical translational scenarios, this review provides a unified roadmap to accelerate the clinical deployment of multimodal drug response prediction.

***Keywords***: Multimodal fusion, drug efficacy prediction, transfer learning, graph neural network, transformer, PK/PD modeling, clinical translation

## 1. Introduction

Drug efficacy prediction critically influences drug development, clinical decision-making, and precision medicine. Conventional pipelines relying on *in vitro* assays, animal models, and small-scale trials are time-consuming, costly, and prone to high attrition. In clinical practice, "one-size-fits-all" regimens often fail owing to profound inter-patient genetic, phenotypic, and physiological heterogeneity, leading to suboptimal responses, adverse events, and accelerated resistance (*1-3*). Computational biology and artificial intelligence (AI) have offered powerful alternatives. Early models primarily used single-omics data, including genomics, transcriptomics, proteomics, and metabolomics, to decipher molecular mechanisms, enabling pharmacogenomic-guided dosing (*4-6*). However, biological systems are dynamic, multi-scale networks spanning molecules to organisms. Drug responses are modulated by gene expression, the tumor microenvironment, tissue architecture, and systemic factors, information that single-omics approaches cannot fully capture. This fragmented view largely explains the poor translational success of preclinical findings (*7,8*).

Multimodal data integration has thus emerged as a transformative paradigm, unifying multi-omics profiles, pathology images, electronic health records (EHRs), molecular structures, and pharmacokinetic/pharmacodynamic (PK/PD) time-series. Yet such integration confronts three intertwined bottlenecks, namely the cross-domain gap, systematic distribution shifts between *in vitro* cell lines and clinical patients; the relational gap, the mismatch between isolated feature vectors and the networked nature of biological interactions; and the feature gap, the inherent heterogeneity in semantics, scale, and distribution across modalities (9). Three mainstream AI modeling paradigms have been widely adopted to resolve these fusion

challenges, with each addressing one core statistical gap as its primary advantage while simultaneously mitigating multiple auxiliary limitations. Transfer learning mainly alleviates cross-domain covariate shift and limited labeled sample sizes. Graph neural networks (GNNs) provide natural structural frameworks to quantify networked biological correlations among genes, proteins, small-molecule drugs, and disease phenotypes. Transformer architectures leverage self-attention mechanisms to capture global feature interactions and long-range biological dependencies, strengthening cross-modal information aggregation. Collectively, the three methodologies primarily target three core gaps in multimodal drug response modeling, namely the cross-domain gap, the relational gap, and the feature gap, and form a mutually complementary technical system with overlapping functional boundaries (*10-12*).

This review establishes a complete logical chain covering multimodal heterogeneous data integration, optimized statistical modeling *via* AI algorithms, and real-world clinical translational deployment. Centered on transfer learning, graph neural networks, and Transformer architectures, we systematically summarize the methodological evolution, integrated fusion frameworks, hierarchical clinical application scenarios, and unresolved bottlenecks of multimodal drug efficacy prediction. The manuscript elaborates on three core integration barriers, three mainstream technical pathways, four layered clinical translational scenarios, and three categories of systematic practical challenges. Despite remarkable progress in algorithmic design, prominent obstacles remain unresolved, including the standardized harmonization of heterogeneous multimodal datasets, model interpretability, and the scarcity of prospective clinical validation cohorts, all of which demand further targeted research. This review aims to construct a systematic, forward-looking overview for researchers and clinical practitioners, and to accelerate the translational transformation of computationally predicted drug efficacy from theoretical modeling to routine clinical practice.

## 2. Literature search and study selection

This manuscript is a narrative review rather than a systematic or scoping review; accordingly, we did not follow the standardized PRISMA-ScR reporting framework. To ensure full transparency in literature collection and selection, we detail the retrieval strategies and screening procedures below. Literature retrieval was performed across four authoritative biomedical databases, namely PubMed, Web of Science Core Collection, CNKI, and Embase, with the search time window set from January 2018 to April 2026 to capture cutting-edge advances in multimodal fusion and AI-driven drug efficacy prediction over the past decade. Landmark foundational papers published before 2018 were manually supplemented by tracing the citation chains of highly cited works. Three groups of combinatorial English keywords were used for retrieval, covering drug efficacy prediction (drug response prediction, drug efficacy forecasting, personalized pharmacotherapy, drug repurposing, and combination drug synergy), multimodal data integration (multi-omics fusion, pathological imaging, electronic health records, molecular structures, and multimodal learning), and artificial intelligence algorithms (transfer learning, graph neural networks, Transformers, covariate shift, domain adaptation, and biological graph modeling). Corresponding Chinese keywords were adopted for CNKI retrieval to incorporate domestic pharmaceutical and biostatistical research.

Clear inclusion and exclusion criteria were established for literature filtering. Eligible studies included original research articles, reviews, and methodological papers concentrating on multimodal fusion modeling for drug response prediction; studies that constructed or validated transfer learning, graph neural network, or Transformer architectures using pharmaceutical datasets; and research involving clinical translational analysis, PK/PD multimodal integration, or cross-domain distribution calibration of drug prediction models. Excluded works comprised pure single-omics studies without multimodal fusion design; papers merely introducing basic AI theories without pharmaceutical or clinical validation; conference abstracts, case reports, editorials, letters, and other non-peer-reviewed grey literature; as well as duplicate publications and articles with incomplete experimental data or ambiguous model descriptions. The screening workflow consisted of two rounds of assessment: titles and abstracts were first scanned to remove irrelevant records, then all remaining full texts were independently evaluated by two authors against the inclusion criteria, with any disagreements resolved through group discussion. Ultimately, 84 representative studies were selected to build the literature foundation of this narrative review.

## 3. Three core gaps in multimodal data integration

Multimodal data provide comprehensive multi-scale information for drug efficacy prediction, spanning from molecular to phenotypic levels and from microscopic to macroscopic perspectives. However, inherent differences in the sources, structures, and semantics of various data types mean that simple concatenation or shallow fusion fails to achieve effective integration and may even introduce noise and bias. Three fundamental bottlenecks underlie this challenge, as illustrated in Figure 1. The first major barrier is the cross-domain gap, manifested as systematic distribution differences among datasets from distinct biological backgrounds, experimental conditions, and patient populations. The most typical example is the irreducible discrepancy between *in vitro* cell line data and clinical patient data. During long-term

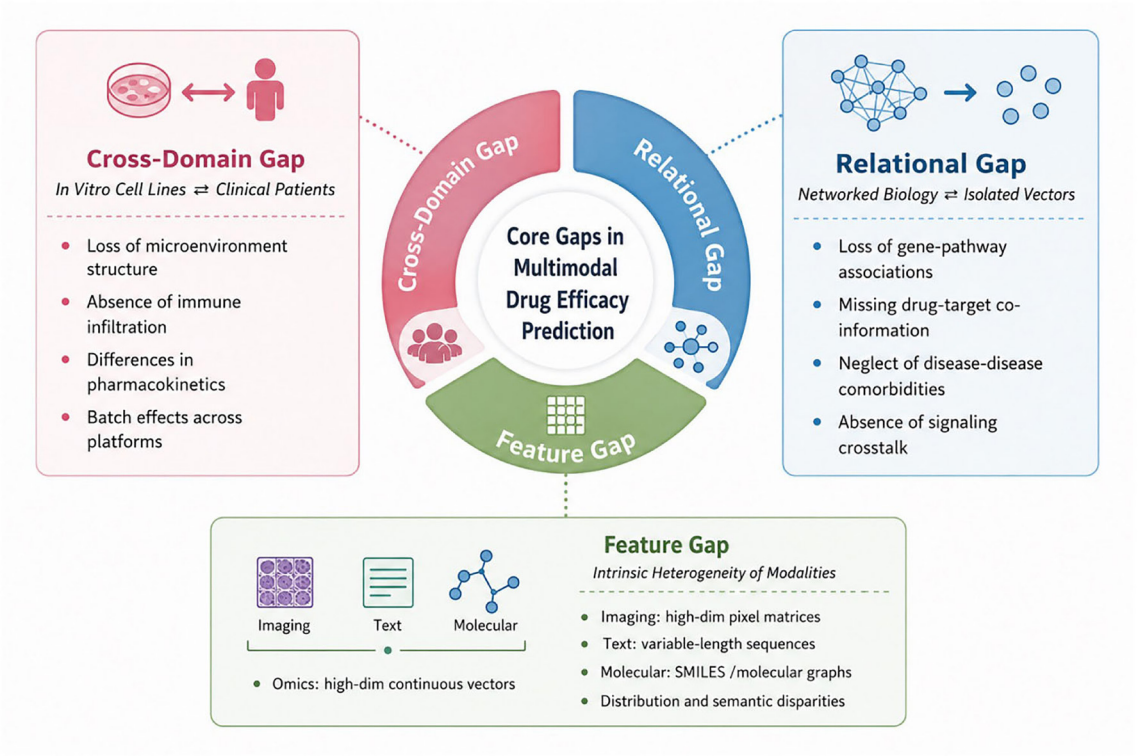


**Figure 1. Core gaps in multimodal drug efficacy prediction.** The three main challenges include the cross-domain gap between in vitro cell line data and clinical patients, the relational gap between networked biological systems and isolated vector representations, and the feature gap caused by intrinsic heterogeneity across different data modalities (omics, imaging, molecular structures, and text).

passage, cell lines lose the microenvironmental structure, immune infiltration, stromal interaction, and pharmacokinetic characteristics of the original tumor, leading to systematic deviations in their gene expression profiles and drug response spectra compared with patients' primary tumors. Models trained on cell line databases such as the Cancer Cell Line Encyclopedia (CCLE) and the Cancer Therapeutics Response Portal (CTRP) often show significant performance decline when applied to patient-derived xenograft (PDX) models or clinical cohorts (*12,13*). This gap is not merely a statistical distribution difference but also stems from incomplete biological information: cell line data lacks key dimensions such as microenvironment and immune status, which cannot be compensated for by simple data alignment. Similar cross-domain issues also exist between different sequencing platforms, laboratory batches, and population cohorts, severely limiting the generalization ability of predictive models.

The second key obstacle is the relational gap, arising from the mismatch between the network structure of biological systems and conventional isolated data representation. Life activities are not linear superpositions of isolated entities but dynamic networks coupled by multi-level relationships such as gene regulation, protein-protein interactions, and signaling pathway crosstalk (*14*). Drug responses often involve coordinated expression of multiple genes and feedback regulation of pathways. However, traditional data representation methods treat each sample as an independent vector, completely losing association information between entities, such as whether two genes are located in the same pathway, whether drugs share targets, or whether there are comorbidity relationships between diseases. These are precisely the key prior knowledge constraints for predicting drug efficacy. The essence of the relational gap is the structural contradiction between isolated data representation and the networked characteristics of biological systems, which prevents models from using relational priors to constrain the prediction space.

Beyond cross-domain and relational barriers, multimodal integration is further constrained by the feature gap, which arises from inherent heterogeneity across data modalities in terms of physical meaning, dimensional scale, statistical distribution, and semantic level. For instance, drug molecular structures can be encoded as SMILES sequences, molecular fingerprints, or molecular graphs; pathological images are presented as high-dimensional pixel matrices; and clinical data exist as structured electronic health records or free-text narratives. These different modalities vary significantly in their structural forms, dimensional scales, and statistical distributions, making direct feature alignment and fusion difficult (*15-17*). Traditional shallow fusion methods, such as simple feature concatenation or weighted averaging, often fail to exploit the complementary advantages of heterogeneous data and may even introduce noise or dilute key biological signals,

thereby limiting improvement in prediction accuracy.

These three gaps are not isolated but closely coupled and mutually interactive. The cross-domain gap exacerbates distribution discrepancies across different data modalities; the lack of relational information undermines the stability of cross-domain alignment; and semantic barriers at the feature level further hinder the effective integration of multi-source data. Accordingly, systematic advances in multimodal drug efficacy prediction require simultaneous resolution of all three core challenges, along with the construction of an integrated framework that accommodates multi-source data, characterizes biological interactions, and unifies heterogeneous feature representations.

## 4. Core technical methods for multimodal drug efficacy prediction

Facing the cross-domain gap, relational gap, and feature gap inherent in multimodal data integration, transfer learning, GNNs, and Transformer models provide targeted technical support from different dimensions. Together they form a complete methodological system that realizes horizontal integration of heterogeneous data, structured modeling of biological relationships, and in-depth interaction of multimodal features. Transfer learning mainly addresses the cross-domain discrepancy and bridges data from cell lines and clinical patients *via* knowledge migration. GNNs focus on the relational gap, constructing structured biological frameworks through heterogeneous graphs and hypergraphs. The Transformer architecture targets the feature gap, unifying multimodal representation and cross-modal alignment by leveraging global self-attention. Multimodal fusion relies on the above three techniques to achieve deep feature aggregation and semantic consistency. These methods develop hierarchically and complement one another, driving drug efficacy prediction from single-data analysis toward comprehensive multi-dimensional information fusion. Representative technical methods for addressing these core challenges are summarized in Table 1, and their many-to-many relationships with the three integration gaps are further visualized in Table 2.

### 4.1. Transfer learning: horizontal knowledge transfer across data sources

Transfer learning serves as the primary paradigm to alleviate the cross-domain gap by constructing knowledge migration pipelines that link *in vitro* cell line source domains with clinical patient target cohorts. Its methodological evolution follows two threads: from homogeneous single-modality migration to cross-domain generalization across distinct distributions, and from bulk-level alignment to cross-scale adaptation at single-cell resolution (*18-20*). The central challenge remains

**Table 1. Representative technical methods for addressing core challenges in multimodal drug efficacy prediction**

| Technical Method | Addressed Core Gap | Core Idea | Key Technical Points |
|---|---|---|---|
| Transfer Learning | Cross-domain gap (cell line → clinical patient distribution shift) | Achieve cross-domain data alignment through knowledge transfer mechanisms | Adversarial domain adaptation; multi-task learning; triplet loss; progressive transfer; cross-resolution integration; contrastive domain regularization |
| Graph Neural Network | Relational gap (biological network *vs.* isolated feature representation) | Construct structured relational frameworks to model complex associations | Heterogeneous GNN; hypergraph learning; cross-layer graph fusion; graph attention; graph contrastive learning; graph autoencoder-based representation disentanglement. |
| Transformer | Feature gap (cross-modal heterogeneity and semantic disparity) | Enable cross-modal alignment and long-range dependency modeling *via* self-attention. | Self-attention mechanism; pre-trained language models; multi-head attention; GNN-Transformer fusion; equivariant geometric GNN + Transformer co-modeling. |

**Table 2. Many-to-many correspondence between mainstream modeling methods and three core integration gaps**

| Method Category | Cross-Domain Gap | Relational Gap | Feature Gap |
|---|---|---|---|
| Transfer Learning | ● Primary | ○ Auxiliary | ○ Auxiliary |
| GNN | ○ Auxiliary | ● Primary | ○ Auxiliary |
| Transformer Architectures | ○ Auxiliary | ○ Auxiliary | ● Primary |
| Contrastive Learning | ○ Auxiliary | ○ Auxiliary | ● Primary |
| Adversarial Domain Adaptation | ● Primary | — | ○ Auxiliary |
| Graph Autoencoders | — | ● Primary | ○ Auxiliary |
| Multi-Task Learning | ○ Auxiliary | ○ Auxiliary | ● Primary |
| Meta-Learning | ● Primary | ○ Auxiliary | — |

Symbol definitions: ● Primary: The technique is fundamentally developed to address this gap and provides dominant, core resolution strategies. ○ Auxiliary: The method yields secondary, indirect benefits to relieve the gap as an additional functionality. — No direct contribution: The technique exhibits no explicit mitigating effect on the gap, and published evidence supporting such functionality is insufficient at present.

how to reliably extrapolate drug response knowledge from cultured cell lines to clinical populations.

For preclinical translation, ScreenDL leverages patient-derived organoids (PDOs) as intermediate carriers and designs a three-stage progressive workflow covering cell lines, PDX models, and clinical samples (*21*). Pharmaformer validates this strategy using retrospective colorectal and bladder cancer datasets, confirming that intermediate models reduce cross-domain bias (*22*). DTLCDR integrates chemical descriptors, molecular graphs, drug-target interaction profiles, and single-cell transcriptomics to boost out-of-distribution performance (*23*). TransCDR extracts unified latent drug representations *via* cross-domain transfer and achieves stable generalization toward unseen scaffolds (*24*). Clinically, transfer learning repurposes large-scale cell-line screening data for personalized therapy, offering advantages for rare malignancies. MODAE jointly optimizes autoencoder reconstruction, domain adaptation, response regression, and survival prediction (*25*). In renal cell carcinoma studies, deep transfer learning unifies single-cell, spatial transcriptomics, and metabolomics to identify tyrosine kinase inhibitor-tolerant subpopulations (*26*). scXDR enables cross-dataset harmonization *via* graph message passing and domain-invariant alignment (*27*). However, cell lines cannot fully recapitulate the tumor microenvironment, setting an upper bound on accuracy (*28*). Severe domain divergence may cause negative transfer, yet most methods align only marginal distributions without preserving causal structures (*29*). Quantitative metrics for detecting and mitigating negative transfer remain underdeveloped (*30*).

### 4.2. Graph neural networks: Structured modeling of biological relationships

GNNs construct topological frameworks of multi-type biological entities and accomplish vertical multi-scale aggregation from molecular profiles to clinical phenotypes. Their evolution follows three directions: from homogeneous to heterogeneous graphs, from pairwise to high-order interaction mining, and from flat to hierarchical architectures. Heterogeneous GNNs dominate drug response modeling. MTGNN unifies compounds, targets, and disease phenotypes within one graph and leverages direction-sensitive meta-paths to trace drug-target-disease associations (*11*). MRDDA expands entity sets to include drugs, diseases, proteins, genes, and pathways, combining mixed convolution layers for local and global feature extraction (*31*). GraphTCDR maintains stable fusion performance under partial node feature missing (*32*). Heterogeneous pipelines have also been extended to traditional Chinese medicine research (*33*). Hypergraph neural networks capture collective synergistic effects beyond pairwise graphs. MRHGNN encodes high-order drug-target-protein complex interactions (*34*). HCLGT-DRP constructs modality-specific hypergraphs followed by cross-hypergraph attention aggregation (*35*). Many works incorporate molecular pre-trained models such as ChemBERTa for node feature initialization (*36*). Heterogeneous graphs rely on meta-path reasoning, whereas hypergraphs naturally describe multi-molecule group interactions.

Cross-layer fusion strategies align with biological hierarchy. DeepKGI builds multi-tier gene graphs covering molecule, pathway, and functional module layers, using cross-layer attention to capture cross-scale links (*37*). GLASynergy constructs global-local dual views, extracting local topological signatures *via* GCNs and generating holistic drug-pair representations *via* adaptive attention (*38*). Clinically, GNNs integrate mutation profiles, drug-drug interactions, and signaling crosstalk to guide combinatorial regimen design (*39*). Graph contrastive learning and adaptive attention refine feature screening: AGRL-DSE enables weighted multi-scale aggregation (*40*); RSGCL-DTI mitigates bias on imbalanced datasets (*41*); MOLGAECL combines autoencoder pre-training with contrastive fine-tuning (*42*). Nevertheless, heterogeneous and hypergraph GNNs face scalability bottlenecks, as computational cost grows rapidly with node types and hyperedge orders, limiting deployment on large patient cohorts. Designing lightweight architectures that retain relational expressiveness remains a key engineering challenge for clinical translation.

### 4.3. Transformer: global alignment of multimodal feature interaction

Transformers mitigate the feature gap *via* self-attention, overcoming the sequential limitations of RNNs and CNNs while delivering a global receptive field. Unlike GNNs that encode explicit topologies, Transformers excel at holistic context modeling and cross-modal semantic alignment. Clinically, Transformers unify multi-omics, pathology images, and EHRs to construct complete patient phenotypic profiles. DualPG-DTA uses pre-trained language encoders to process SMILES strings and protein sequences, with cross-attention enabling bidirectional interaction for binding affinity prediction (*43*). MTEGDRP integrates Transformer with equivariant GNNs: the Transformer captures long-range omics dependencies while equivariant GNNs retain 3D conformational geometry (*44*). For high-order association mining, HCLGT-DRP combines multi-head attention with hypergraphs in a unified Graph Transformer (*35*). Beyond prediction, Transformers improve interpretability; visualized attention maps pinpoint binding residues and functional fragments, guiding clinical decisions (*43*). Hybrid GNN-Transformer architectures preserve topological constraints while harnessing global context, forming a standardized pipeline: the GNN branch aggregates relational

information, the Transformer branch encodes cross-modal dependencies, and bidirectional cross-attention fuses both streams (*44*). Nevertheless, pure Transformers cannot fully encode biomolecular topologies, and stacked attention layers incur high computational costs; attention pruning and graph-Transformer co-design are thus critical for deployment efficiency.

### 4.4. Synergistic mechanisms and fusion paradigms

These three methodologies form complementary rather than rigid one-to-one relationships, and their organic integration is essential for thorough multimodal fusion. Three fusion paradigms differ in execution order and aggregation logic. Sequential fusion executes modules stepwise: transfer learning first aligns cell-line knowledge, GNNs then build heterogeneous graphs, and Transformers finally perform cross-modal interaction (*10,45*). This offers clear division but risks error propagation. Drug-target affinity prediction typically follows this design (*43,45-47*). Parallel fusion operates modules concurrently within a unified architecture, with attention gating dynamically fusing multi-source representations (*44*). This maximizes complementarity but imposes stricter convergence constraints, and has become mainstream for synergy prediction (*20,34,35*). Hierarchical fusion maps biological layers onto tiered networks; bottom transfer learning harmonizes cross-domain data, middle GNNs preserve relational priors, and top Transformers enable global semantic communication (*20,35*). This best matches the hierarchical nature of biological regulatory systems and represents a leading research direction (*38,48,49*).

Auxiliary algorithms, including contrastive learning, adversarial domain adaptation, graph autoencoders, multi-task learning, and meta-learning, are embedded into these paradigms to resolve sub-problems, each alleviating multiple gaps simultaneously. Table 2 visualizes the many-to-many mapping between all modeling methods and the three core gaps. Nearly all current frameworks assume temporal consistency of multimodal data, yet real-world clinical data exhibit temporal heterogeneity: EHRs are irregular sparse time series, imaging spans multiple visits, and omics are mostly baseline-only. Dynamic GNNs and time-aware Transformers represent promising directions to model longitudinal trajectories and response evolution.

### 4.5. Integration of pharmacokinetic and pharmacodynamic multimodal data

Pharmacokinetic (PK) and pharmacodynamic (PD) readouts are indispensable multimodal clinical covariates bridging preclinical modeling and individualized outcomes. PK profiles quantify ADME behaviors, while PD signatures capture dose-dependent target inhibition and phenotypic responses. Combined PK-PD datasets contain continuous concentration-time curves, longitudinal dosing records, and graded adverse event biomarkers, which cannot be fully characterized by static omics or molecular graphs alone. Their integration mitigates the feature gap and partially alleviates cross-domain shift from incomplete *in vivo* signals in cell line data (*50,51*). Time-aware Neural-ODE encoders map concentration trajectories into compact embeddings, accommodating irregular sampling (*52-55*). Dose-response regression extracts descriptors such as maximum efficacy and half-maximal concentration, appended as node attributes in GNNs (*56,57*). Categorical treatment records are processed *via* multi-task learning with auxiliary toxicity and efficacy branches (*58,59*). Toxicity endpoints are encoded as ordinal features or integrated into multi-objective losses (*60*). This multi-layer encoding unifies PK-PD temporal signals with static molecular features within shared latent manifolds (*61*).

The three fusion paradigms can incorporate PK/PD branches with differentiated optimization. In sequential fusion, transfer learning harmonizes preclinical omics, GNNs model drug-target-PD associations, and Transformers integrate longitudinal PK trajectories with static signatures (*62*). In parallel fusion, independent encoding branches for molecular graphs, pathology, multi-omics, and PK/PD time-series are dynamically weighted *via* cross-attention, as in MMPK for oral PK prediction (*63*). In hierarchical fusion, the bottom layer calibrates cross-species PK *via* transfer learning, the middle layer encodes drug-pathway relationships *via* GNNs, and the top layer integrates dynamic trajectories *via* Transformers (*64,65*). Empirical validations confirm that PK/PD-integrated models reduce bias, particularly for compounds with high inter-individual variability, and distinguish true synergy from additive effects (*66,67*). Three bottlenecks persist: animal PK parameters exhibit covariate shift relative to human profiles (*50,68*); few graph frameworks explicitly link dosage, PK exposure, and PD phenotypes *via* hyperedges (*69,70*); and PK time-series, PD curves, and static vectors possess vastly different distributions, with simple concatenation diluting temporal signals (*71*). Sparse clinical sampling further introduces noise. Future work should combine dynamic GNNs with time-equivariant Transformers to jointly encode static networks and time-varying trajectories (*72,73*).

## 5. Clinical translation scenarios of multimodal drug efficacy prediction

The clinical translational value of multimodal artificial intelligence in drug efficacy prediction can be interpreted from two progressive dimensions: the increasing complexity of clinical decision-making and the full life cycle of drug research and development (R&D). It covers four hierarchical application scenarios: selecting

optimal single-drug regimens for individual patients, optimizing combined therapeutic strategies, discovering new indications for approved drugs, and conducting early clinical evaluation of novel drug candidates. Collectively, these scenarios form a closed-loop ecosystem spanning new drug development, personalized medication, and drug repurposing. This section systematically elaborates the above four scenarios, focusing on the enabling logic, implementation pathways, and remaining translational bottlenecks of multimodal drug efficacy prediction technologies. The core clinical application scenarios are illustrated in Figure 2.

### 5.1. Personalized monotherapy selection

Personalized monotherapy selection aims to identify the optimal single-drug regimen for individual patients. Multimodal models integrate multi-omics, imaging, and clinical data to match patient profiles with drug properties, outperforming population-based approaches and reducing reliance on expensive molecular assays. Chu *et al.* developed the MDD-CoD framework, which adopts a three-stage cascaded decision workflow that unifies clinical phenotypic readouts and multi-attribute drug descriptors to output individualized medication suggestions, surpassing classical baseline models across test cohorts of chronic kidney disease, rheumatoid arthritis, and colorectal carcinoma (*49*). For clear cell renal cell carcinoma, integrated pipelines incorporating germline and somatic genomic variants, histopathological phenotypes, and longitudinal follow-up records have been established to construct recurrence risk scoring systems, supporting joint modeling of molecular biomarkers, tissue morphological traits, and long-term clinical endpoints (*74,75*). The MMPCC architecture combines hematoxylin and eosin (H&E) whole-slide imaging, somatic mutation profiles, and routine clinical records to predict patient-specific drug responses, representing a viable alternative for resource-limited settings where comprehensive genetic testing is not universally accessible (*76,77*).

Despite encouraging retrospective results, personalized prediction frameworks face substantial translational barriers. Most models are trained on single-center, demographically homogeneous retrospective cohorts, resulting in limited out-of-distribution generalization across multi-regional populations and disparate hospital systems, a challenge that directly mirrors the cross-domain gap defined in Section 2. Current pipelines predominantly focus on static pre-treatment risk stratification and rarely incorporate dynamic longitudinal biomarkers, limiting their capacity to support real-time adaptive dosing consistent with PK/PD temporal modeling (Section 4.5). Moreover, most reported performances are validated solely on retrospective datasets, whereas rigorous prospective clinical trial evidence remains scarce. The paucity of high-quality randomized controlled trial (RCT) datasets constitutes the primary bottleneck to large-scale clinical adoption.

### 5.2. Combination therapy optimization

When monotherapy fails due to tumor heterogeneity or acquired resistance, clinical decision-making shifts to multi-drug regimen optimization (*78-80*). GNNs and hypergraph architectures capture high-order synergies among compounds, targets, and pathways, advancing

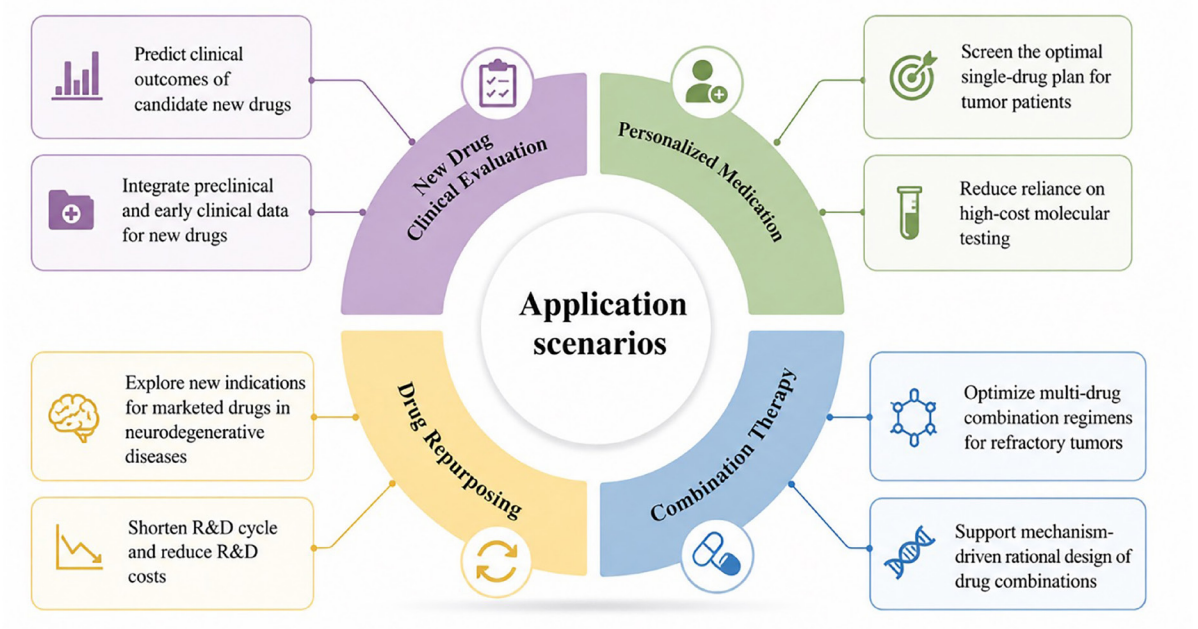


**Figure 2. Clinical application scenarios of multimodal drug efficacy prediction.** The four core scenarios include personalized medication, combination therapy, drug repurposing, and new drug clinical evaluation, each addressing distinct clinical and translational needs.

combination design from empirical screening to mechanism-guided rational development (*11,45,46*). Huang *et al.* constructed the Madrigal system, which extracts unified latent embeddings from molecular scaffolds, signaling cascade maps, cellular functional readouts, and transcriptomic profiles to quantify combinatorial effects. Validated against a dataset comprising 953 clinical endpoints and 21,842 small molecules, the framework simultaneously predicts adverse pharmacokinetic interactions and maintains concordance with head-to-head clinical trial observations, supplying actionable evidence for combined interventions in type 2 diabetes and metabolic dysfunction-associated steatohepatitis (MASH) (*81*). For synergy regression, Saeed *et al*. proposed MMDGNN, which fuses molecular fingerprint descriptors and SMILES representations within an adaptive graph learning backbone (*80*). Zhang *et al*. developed MOSAIC, a multi-granularity cross-modal encoding framework that accounts for global molecular topology and local substructure fragments, with bidirectional cross-attention gates facilitating information exchange across heterogeneous feature spaces (*81*). Chen *et al.* introduced MRHGNN, a dual-branch hypergraph architecture that mines compound physicochemical attributes and multi-agent high-order interaction topology (*34*). To address data sparsity in rare malignancies, Feng *et al.* proposed MetaSynergy, which implements fast cross-layer meta-adaptive optimization by integrating molecular graph topologies and cell-line multi-omics signatures, effectively mitigating performance degradation arising from limited *in vitro* screening data (*82*).

Despite methodological advances, prominent translational bottlenecks remain. Most computational synergy outputs lack systematic validation in high-fidelity preclinical models, and prospective cohort evidence remains insufficient to establish a complete pipeline from algorithmic prediction to experimental validation and clinical confirmation. Many models output scalar synergy scores without interpretable mechanistic decomposition of molecular interactions, limiting clinical adoption. Current research also displays a strong oncological bias, with far fewer investigations addressing chronic inflammatory and autoimmune disorders. Importantly, only a small proportion of published algorithms have undergone the full translational chain from *in silico* forecasting and laboratory validation to prospective patient verification. High-throughput preclinical platforms based on patient-derived organoids (PDOs) and humanized mouse models have yet to form iterative co-optimization workflows with multimodal prediction architectures. These limitations, spanning insufficient mechanistic interpretability, incomplete disease pathway coverage, and inadequate validation infrastructure, collectively reflect the relational, feature, and cross-domain gaps elaborated in Section 3.

5.3. Drug repurposing

Drug repurposing substantially shortens R&D timelines and reduces costs by identifying new indications for approved agents. GNNs decode drug–disease–target links, multi-omics dissects regulatory cascades, and transfer learning extrapolates knowledge from data-rich to rare diseases, transforming random screening into targeted repurposing (*83*). Gunther *et al.* constructed a multi-stage biologically informed workflow combining transcriptomic profiling, proteomic measurement, and PDO phenotypic functional assays for endometriosis, a chronic disorder with limited non-hormonal options. The framework confirmed elevated ROR1 expression, computationally shortlisted candidates, and completed *in vitro* verification in organoid systems, identifying the marketed agent rimegepant as a promising repurposed candidate (*84*). Beyond wet-lab validation, computational architectures have been deployed across diverse diseases. In neurodegenerative disorders, interpretable deep learning systems incorporating genome-wide association study (GWAS) genotypes and multi-omics signatures prioritize repurposing leads and elucidate molecular pathological cascades (*85,86*). For metabolic and hepatic diseases, multi-omics workflows have uncovered anti-fibrotic bioactivity of existing agents, with compounds validated to modulate the EGR1/STAT3 transcriptional axis (*87*). During viral emergencies, rapid integration of viral genomic signatures and drug-target interaction mechanisms supports high-throughput identification of broad-spectrum repurposed antivirals (*86,88*). The DeepSeq2Drug framework demonstrates the performance gains achieved through multimodal embedding and cross-domain transfer learning for antiviral repurposing (*89*). AI pipelines built on aging hallmark biomarkers enable batch identification of multi-functional agents for chronic disorders and senescence, while also providing a paradigm for discovering clinical indications of herbal constituents from traditional Chinese medicine (TCM) (*90,91*). Despite translational promise, existing repurposing frameworks exhibit structural limitations. Most drug-disease association pipelines rely on phenotypic resemblance or transcriptomic correlation without robust causal molecular evidence. Screened candidates rarely undergo large-sample real-world cohort analysis to confirm long-term efficacy and safety. Current architectures tend to overemphasize therapeutic potency while neglecting clinically critical PK/PD covariates such as optimal dosing, treatment duration, and combinative compatibility. Most critically, many preclinically validated leads fail in late-stage evaluation due to suboptimal pharmacokinetic profiles, off-target toxicities, or inadequate dose-response adaptability. This high attrition rate indicates that the positive predictive value of existing multimodal systems requires substantial enhancement to meet rigorous clinical translational standards.

5.4. Clinical evaluation of novel drug candidates

The core bottleneck in drug development is the predictive discrepancy between preclinical results and clinical outcomes. Multimodal fusion integrates multi-scale preclinical readouts and early-phase clinical data to prospectively forecast efficacy, toxicity, and dose–response profiles before full-scale human trials are initiated (*92,93*). For preclinical efficacy prediction, multi-scale frameworks unify compound topological structures, cellular sensitivity signatures, organoid phenotypic readouts, and *in vivo* PK parameters to build hierarchical modeling architectures spanning molecular, cellular, tissue, and organismal layers. Causal GNNs serve as interpretable backbones to disentangle directional regulatory pathways driving therapeutic responses. The ScreenDL pipeline adopts a staged transfer learning workflow that chains cell line screening, PDX and PDO intermediate platforms, and human clinical cohorts, systematically mitigating prediction bias from interspecies covariate shift (*21*). For early safety and dose optimization, digital twin simulation combined with cross-modal fusion enables preemptive identification of adverse event signals in early trial design, providing quantitative evidence for first-in-human dose escalation strategies (*94*). Beyond efficacy and toxicity forecasting, integrated pipelines incorporating target molecular attributes, historical R&D records of analogous scaffolds, and disease subtype signatures leverage causal reasoning modules to stratify predicted response probabilities across patient subpopulations (*95*).

Three interlinked constraints restrict the maturity of this field. First, stringent proprietary data access barriers and fragmented cross-pharma data standards impede large-scale multi-institutional collaborative dataset construction (*69*). Second, the absence of uniform global benchmark specifications, with divergent normalization rules for molecular encoding, toxicological endpoint quantification, and clinical outcome readouts, hampers cross-dataset transferability and robust out-of-distribution generalization. Third, emerging preclinical models including organoids and organs-on-chips lack systematically curated standardized multimodal training cohorts, restricting iterative model refinement. To address these bottlenecks, industry-academia data-sharing consortia should be established, with privacy-preserving federated learning architectures deployed to support collaborative modeling without raw data exchange. Concurrent development of unified global preclinical-clinical benchmark datasets is an essential prerequisite for scaling the clinical deployment of multimodal novel drug evaluation systems.

## 6. Core challenges and future breakthrough directions

Despite transformative performance, systematic obstacles persist across data, modeling, and deployment layers, including data heterogeneity and privacy conflicts, model opacity and poor generalization, and incompatibility with clinical workflows. The field lacks unified benchmark standards, interpretability methods remain post-hoc rather than causally embedded, static paradigms cannot capture disease dynamics (*96*), and regulatory frameworks for AI medical tools are still nascent. To address these layered bottlenecks, systematic advances are required across five interconnected dimensions.

**Data dimension**. Standardized, privacy-preserving multi-center data consortia should be constructed, with federated learning and differential privacy deployed to enable collaborative modeling without raw patient data exchange. Continuous curation of benchmark cohorts derived from organoid and organ-on-a-chip preclinical systems is essential to fundamentally mitigate multimodal heterogeneity and data scarcity limitations (*92,98*).

**Model dimension.** Causal inference frameworks should be fused with domain-specific biological priors to design natively interpretable graph-based architectures. Simultaneously, biomedical foundation models trained *via* large-scale self-supervised pre-training must be developed to boost cross-distribution generalization capacity (*97,99,100*).

**Dynamic temporal dimension.** Longitudinal time-series multimodal readouts should be fully exploited to build integrated dynamic GNN-transfer learning pipelines. Such architectures facilitate a paradigm shift from static snapshot efficacy prediction to continuous simulation of progressive disease trajectories and time-variant drug response kinetics (*96*).

**Generalization dimension.** Large-scale pre-training schemes and cross-domain knowledge transfer modules require further refinement to strengthen model adaptability across variable patient populations, disease spectrums, and real-world clinical settings.

**Clinical translational dimension.** Lightweight, clinician-friendly analytical modules tailored to hospital IT infrastructure need to be engineered. Closed-loop iterative validation workflows linking preclinical laboratory research and prospective clinical trials ought to be established, alongside gradual refinement of regulatory frameworks governing medical AI devices (*85*).

Beyond these five core directions, deeper integration of cutting-edge architectures including graph Transformers, dynamic graph neural networks, geometric GNNs, and self-supervised graph learning will further expand the methodological boundary of multimodal drug efficacy prediction. Iterative optimization of this integrated technical ecosystem tightens the linkage between early-stage pharmaceutical R&D and individualized clinical treatment. Ultimately, this system can furnish more robust and efficient therapeutic decision schemes for complex malignancies, rare disorders, and emergent public health crises, catalyzing the paradigm

transition from universal "one-size-fits-all" empirical medication to patient-specific precision therapy, and lay solid methodological foundations for fundamental and translational biomedical innovation.

## 7. Conclusion

This review establishes a unified theoretical framework centered on three core integration bottlenecks, the cross-domain gap, the relational gap, and the feature gap, and comprehensively surveys three mainstream modeling paradigms, transfer learning, graph neural networks, and Transformers, along with their synergistic fusion strategies. A dedicated section on pharmacokinetic and pharmacodynamic (PK/PD) multimodal integration extends the methodological scope to include *in vivo* longitudinal signals, an aspect often underrepresented in previous reviews, while four hierarchical translational scenarios, namely personalized monotherapy, combination optimization, drug repurposing, and novel drug clinical evaluation, form a complete research chain from preclinical modeling to clinical decision-making. Critically, we clarify the many-to-many complementary relationships between modeling algorithms and the three core gaps, moving beyond the oversimplified one-to-one mapping logic adopted in previous summaries, and elaborate three canonical fusion paradigms, sequential, parallel, and hierarchical, with embedded PK/PD time-series trajectory modeling to bridge static multi-omics data and dynamic *in vivo* therapeutic signals. Five targeted breakthrough directions are proposed, including privacy-preserving multi-center benchmark datasets, causally interpretable graph-Transformer architectures, dynamic temporal modeling frameworks, cross-domain generalization strategies, and lightweight clinical tools, with deeper integration of graph Transformers, dynamic hypergraphs, and self-supervised foundation models poised to further expand predictive capabilities. Collectively, this integrated theoretical framework, comprehensive methodological system, and hierarchical clinical application scenarios offer standardized guidance and actionable routes for future multimodal drug response modeling and translational research, with future work prioritizing organ-on-chip combined PK/PD cohorts, causally interpretable dynamic fusion models, and multi-center prospective clinical validation to accelerate the shift from empirical universal medication to individualized precision therapy.

*Funding*: This work was supported by the Youth Science Fund of the National Natural Science Foundation of China (No.82304382) and University Students' Innovation and Entrepreneurship Training Program (to Junhao Shao).

*Conflict of Interest*: The authors have no conflicts of interest to disclose.

## References

1. Yang X, Kui L, Tang M, Li D, Wei K, Chen W. High-throughput transcriptome profiling in drug and biomarker discovery. Front Genet. 2020; 11:19.
2. Han R, Yoon H, Kim G, Lee H, Lee Y. Revolutionizing medicinal chemistry: the application of artificial intelligence (AI) in early drug discovery. Pharmaceuticals (Basel). 2023; 16:1259.
3. Zahra MA, Al-Taher A, Alquhaidan M, Hussain T, Ismail I, Raya I. The synergy of artificial intelligence and personalized medicine for the enhanced diagnosis, treatment, and prevention of disease. Drug Metab Pers Ther. 2024; 39:47-58.
4. Li X, Wang Z, Wang Q, Xu Q, Lv Q. Clopidogrel-associated genetic variants on inhibition of platelet activity and clinical outcome for acute coronary syndrome patients. Basic Clin Pharmacol Toxicol. 2019; 124:84-93.
5. Chauhan M, Kumar S, Biswas A. A comprehensive review of the advancement in omic technologies in the field of drug discovery and development. Lett Drug Des Discov. 2024; 21:3319-3331.
6. van den Broek WWA, Ingraham BS, Pereira NL, Lee CR, Cavallari LH, Swen JJ, Angiolillo DJ, Ten Berg JM. Genotype-Guided Antiplatelet Therapy: JACC Review Topic of the Week. J Am Coll Cardiol. 2024; 84:1107-1118.
7. Dong M, Wang L, Zhang Y. Integration of multi-omics approaches in exploring intra-tumoral heterogeneity. Cancer Cell Int. 2025; 25:317.
8. Huang S, Shi D, Dai S, Jiang X, Wang R, Yang M. RNF31 induces paclitaxel resistance by sustaining ALYREF cytoplasmic-nuclear shuttling in human triple-negative breast cancer. Clin Transl Med. 2025; 15:e70203.
9. Ktena I, Willsch D, Böhle M. Challenges and opportunities in multimodal prediction for clinical decision support. Nat Mach Intell. 2024; 6:1425-1435.
10. Zheng L, Zhang S, Li Y, Liu Y, Ge Q, Gu L, Xie Y, Wang X, Ma Y, Liu J, Lu M, Chen Y, Zhu Y, Liu H. MTGNN: a drug-target-disease triplet association prediction model based on multimodal heterogeneous graph neural networks and direction-aware metapaths. J Chem Inf Model. 2025; 65:5921-5933.
11. Liu WZ, Lu PL, Chen YT. MMT-fgMDI: Metapath-driven multimodal transformer framework for predicting fine-grained metabolite-drug interactions. Knowl Based Syst. 2026; 332:114899.
12. Partin A, Brettin TS, Zhu YT, Overbeek J, *et al.* Systematic evaluation and comparison of drug response prediction models: a case study of prediction generalization across cell lines datasets. Cancer Res. 2023; 83(7 Suppl):Abstract 5380.
13. Partin A, Brettin TS, Zhu YT, Shukla M, Xia FF, Yoo HS, Dolezal JM, Kochanny S, Pearson AT, Evrard YA, Doroshow JH, Stevens RL. Drug response prediction in patient-derived xenografts with data augmentation and multimodal deep learning. J Clin Oncol. 2022; 40(16 Suppl):e13572.
14. Ohnuki Y, Akiyama M, Sakakibara Y. Deep learning of multimodal networks with topological regularization for drug repositioning. J Cheminform. 2024; 16:103.
15. Xia XQ, Zhu CY, Zhong F, Liu Y. MDTips: a multimodal-data-based drug-target interaction prediction system fusing knowledge, gene expression profile, and structural data.

Bioinformatics. 2023; 39:btad411.
16. Li Y, Ding JX, Du FQ. Deep learning-based multimodal prediction of NAC response in LARC by integrating MRI and proteomics. Cancer Res Treat. 2025. doi: 10.4143/crt.2025.707
17. Chen G, Sun KX. Leveraging multimodal learning for enhanced drug-target interaction prediction. Front Pharmacol. 2025; 16:1639979.
18. Hua Y, Feng ZH, Song XN, Wu XJ, Kittler J. MMDG-DTI: Drug-target interaction prediction *via* multimodal feature fusion and domain generalization. Pattern Recognit. 2025; 157:110887.
19. Velez-Arce A, Li MM, Gao W, Lin X, Huang K, Fu T. Signals in the cells: multimodal and contextualized machine learning foundations for therapeutics. bioRxiv. 2024:2024.06.12.598655.
20. Chen Y, Zhang Y, Niu M, Wang J, Ren Z, Zou Q. UniSyn: a multi-modal framework with knowledge transfer for anti-cancer drug synergy prediction. Genome Biol. 2026; 27:74.
21. Sederman C, Di Sera T, Qiao Y, *et al*. ScreenDL: a transfer learning framework integrating tumor omics and functional drug screening for personalized clinical drug response prediction. Cancer Res. 2024; 84(6 Suppl):Abstract 907.
22. Zhou Y, Dai Q, Xu Y, Wu S, Cheng M, Zhao B. PharmaFormer predicts clinical drug responses through transfer learning guided by patient derived organoid. NPJ Precis Oncol. 2025; 9:282.
23. Yu J, Shi C, Zhou Y, Liu N, Zong X, Liu Z, Zhang L. DTLCDR: a target-based multimodal fusion deep learning framework for cancer drug response prediction. J Pharm Anal. 2025; 15:101315.
24. Xia XQ, Zhu C, Zhong F, Liu L. TransCDR: a deep learning model for enhancing the generalizability of drug activity prediction through transfer learning and multimodal data fusion. BMC Biol. 2024; 22:227.
25. Rintala TJ, Napolitano F, Fortino V. Multi-task deep latent spaces for cancer survival and drug sensitivity prediction. Bioinformatics. 2024; 40(Suppl 2):ii182-ii189.
26. Xie B, Zhang C, Yan Q. Deep transfer learning in clear cell renal cell carcinoma multi-omics unveils a novel tyrosine kinase inhibitor-tolerant cell subgroup for precision therapy. Res Sq [Preprint]. 2025.
27. Qi G, Wang L, Nan M, Fu Y, Ren Q, Zhang Y, Sun Z, Shi Z, Lu J, Gao J. scXDR: drug response prediction across single-cell datasets *via* heterogeneous network transfer learning. Commun Biol. 2026; 9:139.
28. Zhai J, Liu H. Cross-domain feature disentanglement for interpretable modeling of tumor microenvironment impact on drug response. IEEE J Biomed Health Inform. 2024; 28:4382-4392.
29. Pearl J, Bareinboim E. Generalizing experimental results by leveraging knowledge of mechanisms. Eur J Epidemiol. 2021; 36:149-164.
30. Mera A, Vogt M, Bajorath J. A meta-learning framework to mitigate negative transfer in transfer learning applicable to drug design. Sci Rep. 2025; 15:35236.
31. Chen C, Zhou Y, Li Y. MRDDA: a multi-relational graph neural network for drug-disease association prediction. J Transl Med. 2025; 23:753.
32. Zhang J, Xiong S, Xu Y, Zhang Y. Prediction of cancer drug response based on heterogeneous graph neural networks and multi-omics data. Neural Netw. 2026; 193:108001.
33. Li Y, Shen Y, Cai Y, Zhang Y, Gao J, Huang L. Integrating transcriptomic data with a novel drug efficacy prediction model for TCM active compound discovery. Sci Rep. 2025; 15:7688.
34. Chen M, Zhang M, Yan G, Wang G, Qu C. MRHGNN: enhanced multimodal relational hypergraph neural network for synergistic drug combination forecasting. IEEE Trans Neural Netw Learn Syst. 2025; 36:17086-17098.
35. Yang Y, Li P. GPDRP: a multimodal framework for drug response prediction with graph transformer. BMC Bioinformatics. 2023; 24:484.
36. Chithrananda S, Grand G, Ramsundar B. ChemBERTa: large-scale self-supervised pretraining for molecular property prediction. In: Proceedings of the Machine Learning for Molecules Workshop, NeurIPS; 2020.
37. Inoue Y, Fu T, Luna A. GraphPINE: Graph Importance Propagation for Interpretable Drug Response Prediction. Bioinformatics. 2026; 42:btad745.
38. Deng L, Yan S, Yang J, Li M, Ding P. GLA-synergy: an interpretable global-local adaptive framework for drug synergy prediction in cancer treatment. J Chem Inf Model. 2025; 65:11385-11399.
39. Zhang H, Sun X, Wang J, Li M, Tang J. A causal inference framework for identifying essential genes to enhance drug synergy prediction. Bioinformatics. 2026; 42:btag010.
40. Tan H, Ji X, Xu CZ, Zhao X, Hou J, Liu M, Ren Y. AGRL-DSE: adaptive graph representation learning on a heterogeneous graph for drug side effect prediction. ACS Omega. 2025; 10:38753-38765.
41. Bian J, Lu H, Wei L, Li Y, Wang G. Relational similarity-based graph contrastive learning for DTI prediction. Brief Bioinform. 2025; 26:bbaf122.
42. Li Y, Hou LX, Yi HC. MOLGAECL: molecular graph contrastive learning *via* graph auto-encoder pretraining and fine-tuning based on drug-drug interaction prediction. J Chem Inf Model. 2025; 65:3104-3116.
43. Chen Y, Huang J, Liu C, Zhang S, Li X, Zhang Z. DualPG-DTA: a large language model-powered graph neural network framework for enhanced drug-target affinity prediction and discovery of novel CDK9 inhibitors exhibiting *in vivo* anti-leukemia activity. Adv Sci (Weinh). 2026; e13099.
44. Liu Z, Lyu K, Li Y, Sun X, Gao X, Yu B. MTEGDRP: interpretable molecular self-attention transformer and equivariant graph neural network based on multi-omics fusion for drug response prediction in cancer cell lines. J Med Chem. 2026; 69:4771-4788.
45. Chen Q, Nie G, Li X, Xu Y, Tan CSH. BioFusionDTI: assimilating graph and sequence modalities for generalizable drug-target interaction prediction. J Chem Inf Model. 2025; 65:13187-13202.
46. Xu W, Liu Y, Li Z. UAMRL: multi-granularity uncertainty-aware multimodal representation learning for drug-target affinity prediction. Bioinformatics. 2025; 41:btaf512.
47. Peng L, Liu X, Chen M, Liao W, Mao J, Zhou L. MGNDTI: A Drug-Target Interaction Prediction Framework Based on Multimodal Representation Learning and the Gating Mechanism. J Chem Inf Model. 2024; 64:6684-6698.
48. Teoh JR, Sarker IH, Sultana N. Advancing healthcare through multimodal data fusion: a comprehensive review of techniques and applications. PeerJ Comput Sci. 2024; 10:e2298.

49. Chu X, Ye Y, Tang S, Han M, Wang G, Lin S. Personalized medication for chronic diseases using multimodal data-driven chain-of-decisions. Adv Sci (Weinh). 2025; 12:e04079.
50. Chou WC, Lin Z. Machine learning and artificial intelligence in physiologically based pharmacokinetic modeling. Toxicol Sci. 2023; 191:1-14.
51. Tanihata S, Iwata H. Next-Generation Artificial Intelligence for ADME Prediction in Drug Discovery: From Small Molecules to Biologics. Yonago Acta Med. 2026; 69:1-13.
52. Lu J, Deng K, Zhang X, Liu G, Guan Y. Neural-ODE for pharmacokinetics modeling and its advantage to alternative machine learning models in predicting new dosing regimens. iScience. 2021; 24:102804.
53. Giacometti T, Rocchi E, Cojutti PG, Magnani F, Remondini D, Pea F, Castellani G. Leveraging Neural ODEs for Population Pharmacokinetics of Dalbavancin in Sparse Clinical Data. Entropy (Basel). 2025; 27:602.
54. Lu J, Bender B, Jin JY, Guan Y. Deep learning prediction of patient response time course from early data *via* neural-pharmacokinetic/pharmacodynamic modelling. Nat Mach Intell. 2021; 3:696-704.
55. Bräm DS, Nahum U, Schropp J, Pfister M, Koch G. Low-dimensional neural ODEs and their application in pharmacokinetics. J Pharmacokinet Pharmacodyn. 2024; 51:123-140.
56. Fonseca LL, Laubenbacher RC, Böttcher L. Learning dynamical systems with biochemically informed neural ordinary differential equations. bioRxiv. 2026.
57. Ahmadi N, Cao Q, Humphrey JD, Karniadakis GE. Physics-Informed Machine Learning in Biomedical Science and Engineering. Annu Rev Biomed Eng. 2026; 28:309-336.
58. Lee K, Cho D, Jang J, Choi K, Jeong HO, Seo J, Jeong WK, Lee S. RAMP: response-aware multi-task learning with contrastive regularization for cancer drug response prediction. Brief Bioinform. 2023; 24:bbac504.
59. Li YY, Chen L, Pu C, Zang CD, Yan YC, Chen YC, Zhang YM, Liu HC. Co-model for chemical toxicity prediction based on multi-task deep learning. Mol Inform. 2023; 42:e2200257.
60. Sharma B, Chenthamarakshan V, Dhurandhar A, Pereira S, Hendler JA, Dordick JS, Das P. Accurate clinical toxicity prediction using multi-task deep neural nets and contrastive molecular explanations. Sci Rep. 2023; 13:4908.
61. Gu Y, Yu Z, Wang Y, Chen L, Lou C, Yang C, Li W, Liu G, Tang Y. admetSAR3.0: a comprehensive platform for exploration, prediction and optimization of chemical ADMET properties. Nucleic Acids Res. 2024; 52:W432-W438.
62. Cheng Y, Hu H, Dong X, Hao X, Li Y. Exploring Transformer Model in Longitudinal Pharmacokinetic/Pharmacodynamic Analyses and Comparing with Alternative Natural Language Processing Models. J Pharm Sci. 2024; 113:1368-1375.
63. Li X, Zhan M, Fang J, Liu G, Tang Y, Li W. MMPK: A Multimodal Deep Learning Framework to Predict Human Oral Pharmacokinetic Parameters. J Med Chem. 2025; 68:16678-16690.
64. Cui Y, Ji X, Guo W, Chen S, Shen T, Chen L, Ke G, Jin C, Gao Z, Sun W. Toward Generalizable Data-Driven Pharmacokinetics with Interpretable Neural ODEs. J Chem Inf Model. 2026; 66:2640-2650.
65. Chen Y, Zhang Y, Niu M, Wang J, Ren Z, Zou Q, Song J, Luo X. Hierarchical multi-omics data integration and modeling predict cell-specific chemical proteomics and drug responses. Cell Rep Methods. 2023; 3:100452.
66. Chen Y, Zhang Y, Niu M, Wang J, Ren Z, Zou Q, Song J, Luo X. UniSyn: a multi-modal framework with knowledge transfer for anti-cancer drug synergy prediction. Genome Biol. 2026; 27:74.
67. CA H, AS J. PerturbSynX: Deep learning framework for predicting drug combination synergy scores using drug induced gene perturbation data. Comput Biol Chem. 2026; 120:108736.
68. Ota R, Yamashita F. Application of machine learning techniques to the analysis and prediction of drug pharmacokinetics. J Control Release. 2022; 352:961-969.
69. Peng W, Xu X, Lin J, Chen G, Dai W, Fu X, Li L, Liu L, Yu N. Predicting Anti-Cancer Drug Response Based on Hypergraph Representation Learning. IEEE Trans Comput Biol Bioinform. 2025; 22:2430-2441.
70. Ma H, Wang Z, Jia Y, Li Z, Zhao Y, Yu C. Prediction of Cancer Drug Response Based on Hypergraph Convolutional Network and Contrastive Learning. IEEE Trans Comput Biol Bioinform. 2026; 23:1463-1474.
71. Chen Y, Zhang L. Hi-GeoMVP: a hierarchical geometry-enhanced deep learning model for drug response prediction. Bioinformatics. 2024; 40:btae204.
72. Bräm DS, Steiert B, Pfister M, Steffens B, Koch G. Low-dimensional neural ordinary differential equations accounting for inter-individual variability implemented in Monolix and NONMEM. CPT Pharmacometrics Syst Pharmacol. 2025; 14:5-16.
73. Bräm DS, Steiert B, Steffens B, Pfister M, Koch G. Automated Pharmacometric Model Development by Leveraging Low-Dimensional Neural ODEs and LASSO Regression. CPT Pharmacometrics Syst Pharmacol. 2026; 15:e70285.
74. Gui CP, Chen YH, Zhao HW, *et al*. Multimodal recurrence scoring system for prediction of clear cell renal cell carcinoma outcome: a discovery and validation study. Lancet Digit Health. 2023; 5:e515-e524.
75. Zheng QY, Mei HN, Weng XD, Yang R, Jiao PP, Ni XM, Yang XX, Wu JJ, Fan J, Yuan JP, Liu XH, Chen ZY. Artificial intelligence-based multimodal prediction for nuclear grading status and prognosis of clear cell renal cell carcinoma: a multicenter cohort study. Int J Surg. 2025; 111:3722-3730.
76. Arslan S, Schmidt J, Bass C, Mehrotra D, Geraldes A, Singhal S, Hense J, Li X, Raharja-Liu P, Maiques O, Kather JN, Pandya P. A systematic pan-cancer study on deep learning-based prediction of multi-omic biomarkers from routine pathology images. Commun Med (Lond). 2024; 4:48.
77. Partin A, Brettin T, Zhu Y, Dolezal JM, Kochanny S, Pearson AT, Shukla M, Evrard YA, Doroshow JH, Stevens RL. Data augmentation and multimodal learning for predicting drug response in patient-derived xenografts from gene expressions and histology images. Front Med (Lausanne). 2023; 10:1058919.
78. Saeed D, Xing H, Feng L. A scalable multimodal graph neural network for drug combination response prediction. Mol Divers. 2026; 30:1695-1708.
79. Luo T, Zhang Z, Chen XG, Li Z. Multi-modal contrastive drug synergy prediction model guided by single modality. J Cheminform. 2025; 17:146.
80. Li ML, Cao C, Zou Q, Wei LY, Wang YS. MHAFR-

DDI: a multimodal hierarchical attention fusion and relation-aware architecture for drug-drug interaction event prediction. Brief Bioinform. 2026; 27:bbag077.
81. Zhang L, Kang X, Yang X, Wang L, Yang G, Chu J. MOSAIC: a multi-granularity cross-modal framework for predicting synergistic drug combinations in personalized healthcare. IEEE J Biomed Health Inform. 2025. doi: 10.1109/JBHI.2025.3605313.
82. Feng YH, Feng ZL, Yan XY, Zhang SW, Shi JY. Few-shot drug synergy prediction *via* rapid cross-tier adaptation meta-optimization. Brief Bioinform. 2025; 26:bbaf683.
83. Zeng P, Zhang B, Liu A, Meng Y, Tang X, Yang J, Xu J. Drug repositioning based on tripartite cross-network embedding and graph convolutional network. Expert Syst Appl. 2024; 252:124152.
84. Gunther K, Liu D, Stannard G, Holmes M, Loo C, Guo B, Bowden N, Abbott J, Ford CE. An integrated multimodal approach to drug repurposing in endometriosis, using ROR1 as a target. Front Pharmacol. 2025; 16:1716062.
85. Qiu Y, Cheng F. Artificial intelligence for drug discovery and development in Alzheimer's disease. Curr Opin Struct Biol. 2024; 85:102776.
86. Xu J, Mao C, Hou Y, *et al.* Interpretable deep learning translation of GWAS and multi-omics findings to identify pathobiology and drug repurposing in Alzheimer's disease. Cell Rep. 2022; 41:111717.
87. Mijit A, Zhang YZ, Wu Y, Li M, Wang Z, Cheng LF. Dual inhibition of EGR1/STAT3 transcriptional hubs suppresses macrophage-driven liver fibrosis: a multi-omics-guided drug repurposing strategy. Biochem Pharmacol. 2025; 240:117120.
88. Hwang W, Han N. Identification of potential pan-coronavirus therapies using a computational drug repurposing platform. Methods. 2022; 203:214-225.
89. Xie W, Yu J, Huang L, For LS, Zheng Z, Chen X, Wang Y, Liu Z, Peng C, Wong KC. DeepSeq2Drug: a multimodal deep learning framework with transfer learning for antiviral drug repurposing. Comput Biol Med. 2024; 175:108487.
90. Pun FW, Leung GHD, Leung HW, Liu BHM, Long X, Ozerov IV, Wang J, Ren F, Aliper A, Izumchenko E, Moskalev A, de Magalhães JP, Zhavoronkov A. Hallmarks of aging-based dual-purpose disease and age-associated targets predicted using PandaOmics AI-powered discovery engine. Aging (Albany NY). 2022; 14:2475-2506.
91. Wu Y, Huang J, Guo J, Lian W, Suo M. Drug repurposing in traditional Chinese medicine: from empirical wisdom to modern therapeutic strategies. Front Pharmacol. 2025; 16:1631727.
92. Sahu M, Gupta R, Ambasta RK, Kumar P. Artificial intelligence and machine learning in precision medicine: a paradigm shift in big data analysis. Prog Mol Biol Transl Sci. 2022; 190:57-100.
93. Singh Y, Andersen JB, Hathaway QA, Vera-Garcia DV, Keishing V, Venkatesh SK, Salehi S, Povero D, Wallace MB, Gores GJ, Wei Y, Horvat N, Erickson BJ, Quaia E. Leveraging multimodal foundation models in biliary tract cancer research. Tomography. 2025; 11:96.
94. Ren Y, Pieper AA, Cheng F. Utilization of precision medicine digital twins for drug discovery in Alzheimer's disease. Neurotherapeutics. 2025; 22:e00553.
95. Gonzalez G, Lin X, Herath I, Veselkov K, Bronstein M, Zitnik M. Combinatorial prediction of therapeutic perturbations using causally inspired neural networks. Nat Biomed Eng. 2026; 10:1008-1025.
96. Yang H, Tong X. MDEbert-DTA: drug-target affinity prediction using multimodal contrastive learning and dynamic graph aggregation. Appl Intell. 2026; 56:191.
97. Cong Y, Endo T. Multi-omics and artificial intelligence-guided drug repositioning: prospects, challenges, and lessons learned from COVID-19. OMICS. 2022; 26:361-371.
98. Fu C, Chen Q. The future of pharmaceuticals: artificial intelligence in drug discovery and development. J Pharm Anal. 2025; 15:101248.
99. Li Z, Tu X, Chen Y, Lin W. HetDDI: a pre-trained heterogeneous graph neural network model for drug-drug interaction prediction. Brief Bioinform. 2023; 24:bbad385.
100. Sun C, Man XF, Li N, Liu ZH, Chen Z, Yu B. FG-PromptNet: cross-modal prompt learning for explainable molecular property prediction. Comput Biol Chem. 2026; 124:109096.

Received June 15, 2026; Revised August 9, 2026; Accepted August 15, 2026.

**Address correspondence to:*
Qichao Luo, School of Pharmacy, Anhui Medical University, Hefei 230032, Anhui, China.
E-mail: luoqichao@ahmu.edu.cn

Released online in J-STAGE as advance publication August 23, 2026.

*Original Article*

DOI: 10.5582/ddt.2026.01045

# Duzhong Fang (DZF) alleviates rotenone-induced Parkinson's disease-like pathological alterations through regulation of the gut-brain axis *via* the intestinal TPH1/5-HT pathway

**LiLi Li[1], Anran Lv[2], Jibao Yang[1], Xiran Li[1], Zishu Yan[1], Ziyi Zhong[1], Wenqing Tian[1], Bin Jia[1], Yanjun Zhang[3,4], Pengwei Zhuang[3,4,*], Hong Guo[1,*]**

[1] State Key Laboratory of Component-based Chinese Medicine, Tianjin University of Traditional Chinese Medicine, Tianjin, China;
[2] School of Medical Technology, Tianjin University of Traditional Chinese Medicine, Tianjin, China;
[3] First Teaching Hospital of Tianjin University of Traditional Chinese Medicine, Tianjin, China;
[4] National Clinical Research Center for Chinese Medicine, Tianjin, China.

**SUMMARY**: The gut-brain axis is increasingly recognized as a critical pathway in Parkinson's disease (PD), but the gut-targeted mechanisms underlying the therapeutic effects of herbal formulas remain poorly understood. In this study, an enterogenic PD-like mouse model was established by long-term rotenone gavage and treated with Duzhong Fang (DZF) to investigate whether DZF acts through intestinally retained components to influence gut-brain α-synuclein pathology. DZF markedly improved motor dysfunction, increased nigral tyrosine hydroxylase (TH)-positive cell density, alleviated colonic inflammation, and reduced α-Syn accumulation in the vagus nerve and brain, while colonic α-Syn showed a decreasing trend. Mechanistically, DZF downregulated colonic TPH1 and 5-HT3A expression, reshaped gut microbiota composition, and modulated fecal metabolites related to tryptophan metabolism and the 5-HT biosynthetic pathway. Molecular docking predicted potential interactions between TPH1 and gut-retained gingerol-related compounds, including 6-shogaol, 10-gingerdione, 10-gingerol, and 4-gingerol. These findings suggest that DZF ameliorates rotenone-induced PD-like phenotypes and may act by modulating the intestinal TPH1/5-HT-related pathway and α-Syn pathology along the gut-brain axis. This study supports a gut-targeted, neural-regulated therapeutic paradigm for traditional Chinese medicine and provides potential lead compounds for gut-directed anti-PD intervention.

***Keywords***: Duzhong Fang, Parkinson's disease, gut-brain axis, α-synuclein

## 1. Introduction

Parkinson's disease (PD) is the second most common neurodegenerative disorder worldwide. Its main pathological features include progressive loss of dopaminergic neurons in the substantia nigra pars compacta of the midbrain and abnormal aggregation of α-synuclein (α-Syn) (*1*). Clinically, in addition to motor symptoms such as resting tremor, bradykinesia, rigidity, and postural instability, patients often present with non-motor symptoms, including hyposmia, depression, constipation, and gastrointestinal dysfunction (*2*). More importantly, by the time typical motor symptoms emerge, more than 50% of dopaminergic neurons in the substantia nigra have already been lost, indicating that the disease has reached an irreversible stage (*3*). Therefore, investigating the early origin of PD and developing etiology-targeted intervention strategies have become central scientific challenges in the field.

Accumulating evidence suggests that pathological changes in PD may originate outside the central nervous system (*4*). Among these, gastrointestinal dysfunction, as one of the most common and earliest non-motor symptoms of PD, can precede motor symptoms by several years or even more than a decade (*5*). Prospective cohort studies have confirmed that functional gastrointestinal disorders, such as constipation, are associated with a significantly increased risk of developing PD (*6*). These findings strongly support the hypothesis that the gut may be the initial site of PD pathogenesis (*4,7*). Therefore, elucidating the gut-brain connection is of critical importance for developing early intervention strategies for PD.

In 2003, based on a systematic pathological analysis of autopsy specimens from patients with sporadic PD, Braak and colleagues first proposed that pathological

α-synuclein (α-Syn) appears initially in the dorsal motor nucleus of the vagus nerve and the enteric nervous system, and then propagates retrogradely along neuroanatomical pathways to the substantia nigra of the midbrain (*4*). This seminal work formally established the "gut-origin hypothesis" of PD. Subsequently, numerous studies have confirmed that pathogenic α-Syn is not only present in the midbrain substantia nigra, but is also widely distributed in other brain regions, the spinal cord, the gastrointestinal tract, and even the blood, where it acts as an initiating factor in early PD pathogenesis (*8,9*). Experimental evidence further demonstrates that injection of α-Syn preformed fibrils into the gut of animal models induces the propagation of this protein along the vagus nerve to the brainstem, leading to damage of dopaminergic neurons (*7,9,10*). Notably, pathogenic α-Syn is predominantly enriched in enteric neurons under inflammatory conditions, and its expression level positively correlates with the severity of tissue inflammation (*11*). Collectively, these findings suggest that the intestinal inflammatory microenvironment is a key driver triggering local abnormal α-Syn aggregation in the gut.

During the initiation and progression of intestinal inflammation, dysregulation of the gut microbiota and its metabolites play a central regulatory role (*12*). In recent years, the critical role of the gut microbiota as a key modulator of gut-brain signaling has become increasingly recognized, giving rise to the concept of the "microbiota-gut-brain axis" (*13*). Accumulating evidence indicates that the gut microbiota contributes importantly to PD through this axis (*14*). Patients with PD commonly exhibit structural dysbiosis, characterized by an increase in opportunistic pathogens and a decrease in short-chain fatty acid-producing bacteria. These microbial alterations are closely correlated with the severity of motor symptoms and the burden of non-motor symptoms (*15*). Dysbiosis not only disrupts the integrity of the intestinal epithelial barrier and exacerbates local inflammatory responses but also influences host neuroendocrine functions by modulating pathways such as tryptophan metabolism (*16*). Intervention studies targeting the microbiota using antibiotics, probiotics, or fecal microbiota transplantation have confirmed a causal relationship between the gut microbiota and PD, and have demonstrated beneficial effects on host health (*17-22*). Bidirectional communication between the nervous system and the gastrointestinal tract is achieved through multiple pathways, including the vagus nerve, the immune system, and bacterial metabolites (*23*). Therefore, targeting the gut microbiota and its metabolic network represents a promising strategy for early intervention in PD.

Duzhong Fang (DZF) is composed of *Eucommia ulmoides* Oliv. (Duzhong), *Dendrobium nobile* Lindl. (Shihu), *Rehmannia glutinosa* Libosch. (Dihuang), and *Zingiber officinale* Roscoe (Ganjiang). Our previous studies have shown that DZF significantly improves motor coordination and protects dopaminergic-related markers in acute and chronic mouse models of PD (*24,25*). Notably, while some components of DZF can enter the brain, others persist in fecal matter and intestinal contents as parent compounds (*e.g.*, 4-, 6-, 8-, and 10-gingerol; 6-shogaol; 10-gingerdione; scopoletin; pyroglutamic acid; cinnamic acid; and palmitoleic acid), exhibiting distinct intestinal-retention characteristics (*26*). This finding suggests that the effects of DZF may not rely solely on direct entry into the central nervous system but may also involve modulation of gut-related pathways. To test this hypothesis, the present study employed a low-dose rotenone oral gavage-induced gut-origin PD-like mouse model. We aimed to investigate whether DZF ameliorates established PD-like motor and pathological phenotypes through gut-related mechanisms, thereby providing experimental evidence for gut-targeted intervention in PD.

## 2. Materials and Methods

### 2.1. Experimental animals and drugs

Male SPF C57BL/6J mice, aged 8 weeks and weighing 23-25 g, were obtained from Beijing Weitong Lihua Biotechnology Co., Ltd. (License No.: SCXK (Jing) 2019-0008). All experimental procedures were approved by the Animal Ethics Committee of Tianjin University of Traditional Chinese Medicine (Approval No. TCM-LAEC2020084).

To establish the enterogenic PD-like model, 40 mice were randomly divided into four groups: Control, 1 M, 3 M, and 5 M ($n$ = 10 per group). According to Pan-Montojo *et al.* (*27*), mice in the 1 M, 3 M, and 5 M groups were administered rotenone (5 mg/kg; 0.1mL/10g) by daily gavage for 1, 3, or 5 consecutive months, respectively. The Control group received the same volume of vehicle (1% sodium carboxymethyl cellulose containing 1.25% chloroform), underwent the same handling procedures.

To evaluate the effects of DZF on established PD-like phenotypes, 30 mice were randomly divided into control, model, and DZF groups ($n$ = 10 per group). Mice in the model and DZF groups received rotenone (5 mg/kg; 0.1 mL/10g) daily by gavage, whereas the control group received the same volume of vehicle (1% sodium carboxymethyl cellulose containing 1.25% chloroform). Rotenone or vehicle administration continued throughout the 8-month experimental period. Beginning in month 6, after completion of 5 months of rotenone exposure, mice in the DZF group additionally received DZF extract (20 g crude drug/kg; 0.1mL/10g) by gavage 1 h after rotenone administration; control and model mice received an equal volume of normal saline. The dosage of DZF was based on our previous study (*25*).

Duzhong Fang (DZF) was prepared according to the

proportional composition described in Bei Ji Qian Jin Yao Fang (Essential Prescriptions Worth a Thousand Pieces of Gold for Emergency). For experimental preparation, the herbal materials were scaled according to this proportional relationship as follows: *Eucommia ulmoides* (1,000 g), *Dendrobium nobile* (10 g), *Zingiber officinale* (15 g), and *Rehmannia glutinosa* (15 g). These amounts represent scaled experimental quantities rather than the original dosages described in the classical text. The crude herbal materials were mixed and processed for subsequent experiments. The administered crude drug dose was calculated according to the proportional relationship of the experimental formulation. The herbs were reflux-extracted twice with 75% ethanol, first with 10 volumes for 2 h and then with 8 volumes for 2 h. The two extracts were combined, concentrated under reduced pressure, aliquoted, and stored at − 20°C. Before administration, the concentrated extract was diluted with distilled water to the required concentration, corresponding to a dose of 20 g crude drug/kg. The preparation procedure was consistent with our previously reported DZF preparation and chemical characterization (*26*).

2.2. Behavioral tests

Behavioral tests were performed according to previously described methods (*25*). Mice were subjected to behavioral training for three days prior to the formal experiment. During the formal test, each mouse was tested three times, and the average value was used for statistical analysis.

2.3. Immunohistochemistry (IHC) staining

Mice were perfused transcardially, and the brain, colon, and vagus nerve were collected, fixed in 4% paraformaldehyde, embedded in paraffin, and sectioned. Following deparaffinization and rehydration, sections were treated with 3% $H_2O_2$ to quench endogenous peroxidase activity. Antigen retrieval was performed in sodium citrate buffer, and sections were blocked with goat serum. The sections were incubated overnight at 4°C with primary antibodies against tyrosine hydroxylase (TH) (rabbit, Proteintech, 1:500) and α-Syn (rabbit, Abcam, 1:200). The next day, sections were incubated with goat anti-rabbit IgG secondary antibody for 1 h at 37°C. After DAB visualization, images were captured under a light microscope. TH-positive cells in the substantia nigra pars compacta were counted, and α-Syn expression in the brain, vagus nerve, and colon was analyzed.

2.4. Immunofluorescence (IF) staining

Brain and colon sections were permeabilized with 0.03% Triton X-100 and blocked with 10% donkey serum for 1 h at room temperature. Sections were incubated overnight at 4°C with primary antibodies against α-Syn (goat, Abcam, 1:400), TPH1 (rabbit, Affinity, 1:200), 5-HT3A (rabbit, Affinity, 1:200). After washing, sections were incubated for 1 h at room temperature with corresponding secondary antibodies. Nuclei were counterstained with DAPI. Sections were mounted with anti-fade mounting medium and imaged under a fluorescence microscope (Nikon, Japan). Images were analyzed using NIS Elements software (Nikon).

2.5. Hematoxylin and eosin (H&E) staining

Colon tissue samples were collected and fixed in 4% formaldehyde solution. After fixation, the tissues were rinsed under running tap water for 24 h, dehydrated through a graded ethanol series (70%, 80%, 95%, and absolute ethanol), cleared in xylene, and embedded in paraffin. Sections were cut at a thickness of approximately 5 μm, baked at 73°C to enhance adhesion, and then stained with H&E. Histopathological changes in the colon were observed and compared among experimental groups under a light microscope.

2.6. Western blotting

Colon tissues were collected from euthanized mice and weighed. Proteins were extracted by homogenizing the tissues in RIPA lysis buffer (10 μL per mg of tissue) on ice. The homogenate was centrifuged at 15,000 rpm for 10 min at 4°C, and the supernatant was collected for protein quantification using the BCA method. Equal amounts of protein were separated by SDS-PAGE and transferred onto PVDF membranes. The membranes were blocked with 5% skim milk in TBST for 1 h at room temperature, followed by overnight incubation at 4°C with primary antibodies against β-actin (proteintech, 66009-1-Ig, 1:1,000), Clathrin (abcam, ab21679, 1:1,000), IL-1β (Abcam, ab234437, 1:1,000), IL-6 (Abcam, ab290735, 1:1,000), TNF-α (Abcam, ab183218, 1:1,000), and IL-10 (Abcam, ab9969, 1:1,000). After washing, the membranes were incubated with HRP-conjugated goat anti-rabbit or anti-mouse secondary antibodies (Beyotime, a0208, a0216, 1:1,000) for 1 h at room temperature. Protein bands were visualized using a chemiluminescence imaging system, and band intensities were quantified using ImageJ software for statistical analysis.

2.7. Quantitative real-time PCR (qRT-PCR) analysis

Total RNA was extracted from fresh colon tissues using the Eastep™ Super Total RNA Extraction Kit (LS1040, Promega, China) according to the manufacturer's instructions. Briefly, freshly collected colon tissues were homogenized in RNA lysis buffer, and the lysates were processed through silica membrane-based spin

columns. After DNase I treatment to remove genomic DNA contamination, purified RNA was eluted with nuclease-free water. The concentration and purity of RNA were determined using a spectrophotometer, and qualified RNA samples were used for subsequent reverse transcription.

Complementary DNA (cDNA) was synthesized using the GoScript™ Reverse Transcription Mix (A2790, Promega, China) according to the manufacturer's protocol. Quantitative real-time PCR was performed using the SuperReal PreMix Plus (SYBR Green) (FP205-02, Tiangen Biotech, China) on a CFX Connect Real-Time PCR Detection System (Bio-Rad Laboratories, Singapore). The amplification conditions were as follows: initial denaturation at 95°C for 15 min, followed by 40 cycles of denaturation at 95°C for 10 s and annealing/extension at 60°C for 32 s.

The expression levels of target genes were normalized to the endogenous reference gene β-actin. Relative gene expression levels were calculated using the $2^{-\Delta\Delta Ct}$ method. The primer sequences used for qRT-PCR analysis are listed in Table 1.

2.8. 16S rRNA gene sequencing

Total genomic DNA was extracted from fecal samples using the CTAB/SDS method, and its purity and concentration were determined. The V3–V4 hypervariable region of the 16S rRNA gene was amplified by PCR using barcoded specific primers and a high-fidelity DNA polymerase. PCR products were separated by electrophoresis on a 2% agarose gel, and the target bands were excised and purified using the AxyPrep DNA Gel Extraction Kit (Axygen Biosciences, Union City, CA, USA). Purified amplicons were initially quantified by agarose gel electrophoresis and subsequently accurately quantified using the QuantiFluor™-ST Blue Fluorescence Quantitation System (Promega Corporation, Madison, WI, USA). Based on the required sequencing depth, purified products were pooled in equimolar ratios, and sequencing libraries were constructed using the New England Biolabs (NEB, Ipswich, MA, USA). Library quality was assessed using the Agilent 2100 Bioanalyzer and the Qubit system, and only qualified libraries were subjected to sequencing.

After sequencing, microbial community composition was analyzed based on taxonomic annotation. Differential microbial taxa between the model and DZF groups were identified by comparing genus-level relative abundances using Welch's *t*-test implemented in STAMP software. Significantly altered bacterial genera were determined based on differences in mean relative abundance, 95% confidence intervals, and corresponding *P* values. Spearman correlation analysis was performed to evaluate the associations between differential bacterial genera and tryptophan-related metabolites. Correlation coefficients (*r*) and corresponding *P* values were calculated.

**Table 1. Primer sequences for RT-qPCR analysis**

| Gene Name | Primer Sequence | |
|---|---|---|
| β-actin | forward | GTGCTATGTTGCTCTAGACTTCG |
| | reverse | ATGCCACAGGATTCCATACC |
| Tph1 | forward | TCCGTCCTGTGGCTGGTTACC |
| | reverse | AGGTGTCTGGCTCTGGAGTGTAG |

2.9. Untargeted metabolomics analysis

Fresh fecal samples were collected from mice and homogenized with ice-cold methanol-acetonitrile-water (2:2:1). The mixture was vortexed, ultrasonicated at low temperature for 30 min, and then incubated at − 20°C for 10 min. After centrifugation at 14,000 g for 20 min at 4°C, the supernatant was collected and vacuum-dried. The dried extract was reconstituted in acetonitrile-water (1:1), vortexed, and centrifuged again at 14,000 g for 15 min at 4°C. The resulting supernatant was analyzed using ultra-high performance liquid chromatography coupled with Q Exactive mass spectrometry (UHPLC-Q Exactive MS) for data acquisition.

2.10. Molecular docking

The three-dimensional structures of the intestinally retained DZF components identified in our previous study were obtained from the PubChem database, including 6-shogaol (CID: 5281794), 10-gingerdione (CID: 5317591), 10-gingerol (CID: 168115), 4-gingerol (CID: 5317596), 6-gingerol (CID: 442793), 8-gingerol (CID: 168114), cinnamic acid (CID: 444539), palmitoleic acid (CID: 445638), pyroglutamic acid (CID: 7405), scopoletin (CID: 5280460).

The crystal structure of human tryptophan hydroxylase 1 (TPH1) was retrieved from the RCSB Protein Data Bank (PDB ID: 8CJK; UniProt accession: P17752; *https://www.rcsb.org/*). Molecular docking simulations were performed using AutoDock Tools (version 1.5.6; *https://autodock.scripps.edu/*). The binding affinity of each ligand with TPH1 was evaluated based on the predicted binding energy. Docking conformations with favorable binding energies were selected for visualization. The interaction modes between TPH1 and representative compounds were visualized using PyMOL (*https://pymol.org/2/*). The ligand structures were energy minimized before docking.

2.10. Statistical analysis

Continuous data are presented as mean ± standard error of the mean (SEM). Comparisons between two groups were performed using an unpaired *t*-test, and comparisons among multiple groups were conducted

using one-way analysis of variance followed by Tukey's post hoc test when the assumptions of parametric testing were satisfied. Ordinal outcomes, including colonic histopathological scores and traction-test scores, were analyzed using the Kruskal–Wallis test followed by Dunn's multiple-comparison test. $P < 0.05$ was considered statistically significant.

## 3. Results

### 3.1. Low-dose rotenone gavage for five months successfully establishes an enterogenic PD mouse model

To establish a gut-derived PD-like model, mice were administered rotenone (5 mg/kg) by gavage for 1, 3, or 5 months, while control mice received vehicle administration throughout the experimental period. H&E staining revealed progressive colonic damage in rotenone-treated mice, which was most pronounced after 5 months of rotenone exposure (Figure 1A-B). α-Syn expression in the colon, vagus nerve, and brain gradually increased with prolonged rotenone exposure and was significantly elevated after 5 months (Figure 1C-F). Motor-function assessment showed prolonged pole-test time, reduced grip strength, and decreased traction-test scores following rotenone exposure, with the most prominent impairments observed at 5 months (Figure 1G-I). Collectively, these findings indicate that 5 months of rotenone gavage established PD-like intestinal, pathological, and motor phenotypes in mice.

### 3.2. DZF ameliorates motor deficits and preserves TH-positive cell density in a gut-derived PD mouse model

After 5 months of low-dose rotenone exposure, mice exhibited PD-like pathological alterations and motor deficits. Therefore, DZF administration was initiated from month 6 onward while rotenone exposure was continuously maintained to evaluate its effects on established PD-like phenotypes. DZF treatment significantly improved motor performance, as evidenced by reduced pole-test descent time, increased rotarod latency, and amelioration of rotenone-induced gait abnormalities (Figure 2B-G). Consistent with the behavioral improvement, TH immunostaining showed that DZF attenuated the rotenone-induced reduction in TH-positive cell density in the substantia nigra (Figure 2H-I). These findings demonstrate that DZF exerts a protective effect against PD-like pathology in a gut-derived mouse model.

### 3.3. DZF attenuates intestinal pathology and inflammation in rotenone-induced PD mice

DZF not only ameliorated the behavioral deficits but also improved intestinal pathological alterations and the inflammatory microenvironment in rotenone-induced PD mice. As shown in Figure 3A-B, compared with the model group, DZF intervention improved intestinal injury, accompanied by a downward trend in the colonic pathological score. Western blot analysis further revealed that DZF treatment suppressed the aberrant elevation of pro-inflammatory cytokines IL-6, TNF-α and IL-1β in the colon of model mice, while restoring the expression level of the anti-inflammatory cytokine IL-10 to near normal (Figure 3C-G).

### 3.4. DZF alleviates α-Syn-related pathology along the gut-brain axis

Chronic intestinal inflammation has been associated with abnormal α-Syn accumulation in the gut and its involvement in gut-brain communication through the vagus nerve (*9*). We therefore examined α-Syn expression in the colon, vagus nerve, and brain (Figure 4A-C). Rotenone exposure markedly increased α-Syn accumulation in these tissues. Following DZF treatment, α-Syn expression was significantly decreased in the vagus nerve and brain, while a downward trend was observed in the colon (Figure 4D-F). These findings indicate that DZF effectively alleviates rotenone-induced α-Syn-associated pathological alterations along the gut-vagus-brain axis, suggesting a potential regulatory role of DZF in modulating α-Syn-related pathology.

### 3.5. DZF ameliorates gut microbiota dysbiosis in rotenone-induced PD mice

To further investigate the impact of DZF on the intestinal microenvironment, the composition and abundance of gut microbiota in fecal samples from each group were analyzed. A Venn diagram was used to illustrate the distribution of operational taxonomic units (OTUs) among the groups. As shown in Figure 5A, a total of 915 shared OTUs were identified among the control, model, and DZF groups, with 725, 41, and 201 unique OTUs in each group, respectively. Principal coordinate analysis (PCoA) based on unweighted UniFrac distance was performed to visualize the similarity of fecal microbiota structure in a reduced-dimensional space. The results in Figure 5B showed that samples with similar microbial composition clustered more closely, indicating that while certain similarities existed among groups, their microbiota structures were clearly distinguishable.

Further genus-level differential-abundance analysis (Figure 5C-D) identified 11 genera that differed between the DZF and model groups, including *Anaerotruncus*, *Devosia*, Family XIII AD3011 group, *Muribaculum*, *Parafrigoribacter*, and *Pedobacter*.

### 3.6. DZF modulates the gut microbiota-tryptophan metabolism axis in PD model mice

Given that DZF treatment significantly reshaped the

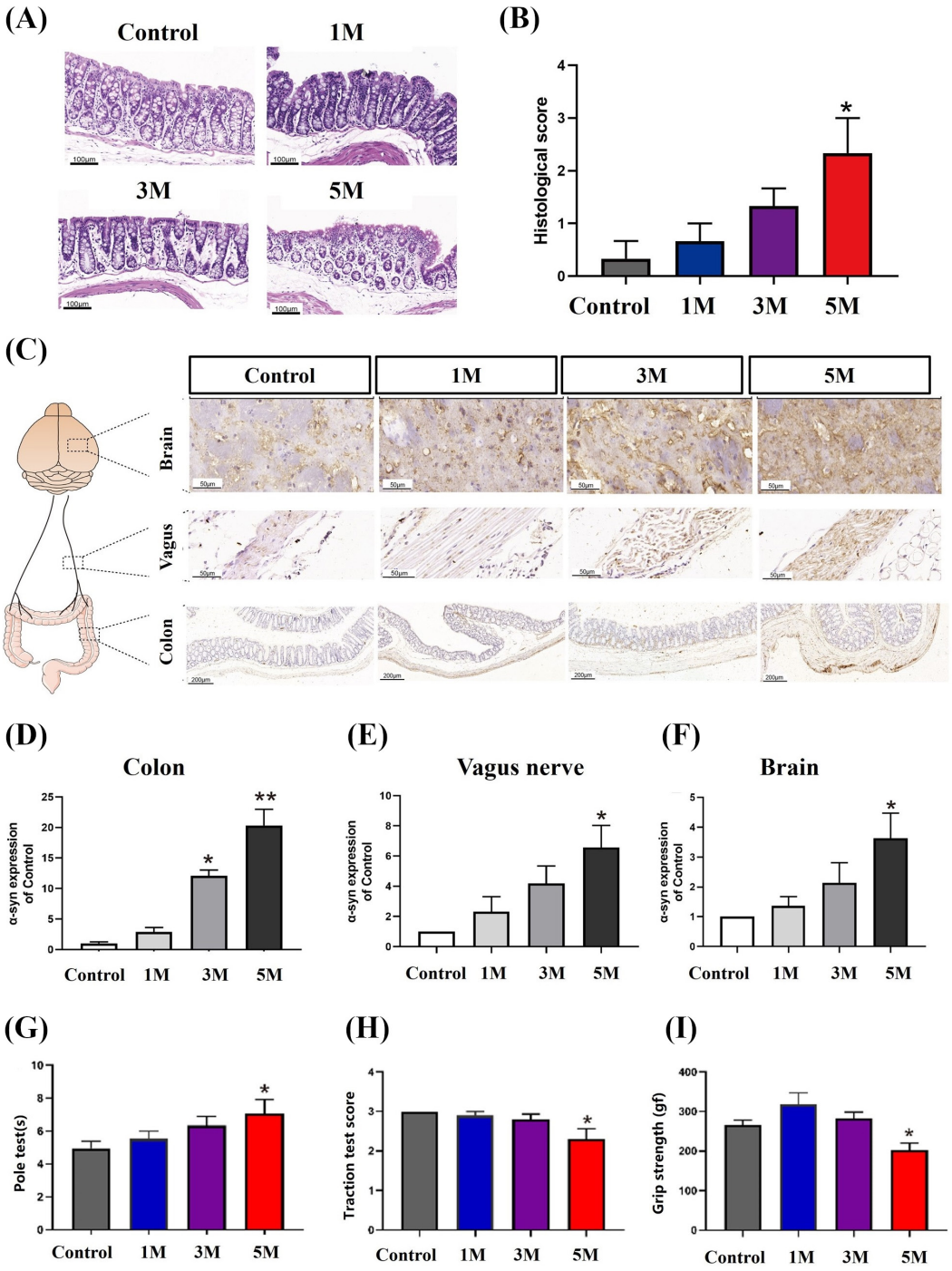


**Figure 1. Rotenone treatment induces intestinal injury and motor dysfunction in mice after 5 months.** Five months of rotenone treatment exacerbated intestinal tissue damage, as evidenced by structural abnormalities in H&E-stained colon sections (**A**) and increased histological injury scores (**B**). α-Syn expression increased in the colon, brain, and vagus nerve (**C-F**), accompanied by motor dysfunction characterized by impaired pole-test performance, reduced traction-test scores, and decreased grip strength (**G-I**). Data are presented as mean ± SEM. For (**A-F**), $n = 3$ per group; for (**G-I**), $n = 10$ per group. The traction test scores (**H**) were analyzed using the Kruskal–Wallis test followed by Dunn's multiple comparisons test. *$P < 0.05$ and **$P < 0.01$ compared with the control group.

gut microbiota composition, we further investigated whether these microbial alterations were accompanied by changes in intestinal metabolic profiles. Untargeted metabolomics was therefore performed to evaluate the effects of DZF on fecal metabolites in the rotenone-induced PD-like mouse model. The orthogonal partial least squares discriminant analysis (OPLS-DA) score plot demonstrated a clear separation between the DZF and model groups, indicating that DZF treatment altered the overall fecal metabolic profile (Figure 6A). KEGG pathway analysis revealed that tryptophan metabolism was significantly enriched and exhibited a relatively high pathway-impact value among the altered metabolic pathways (Figure 6B). Further analysis of

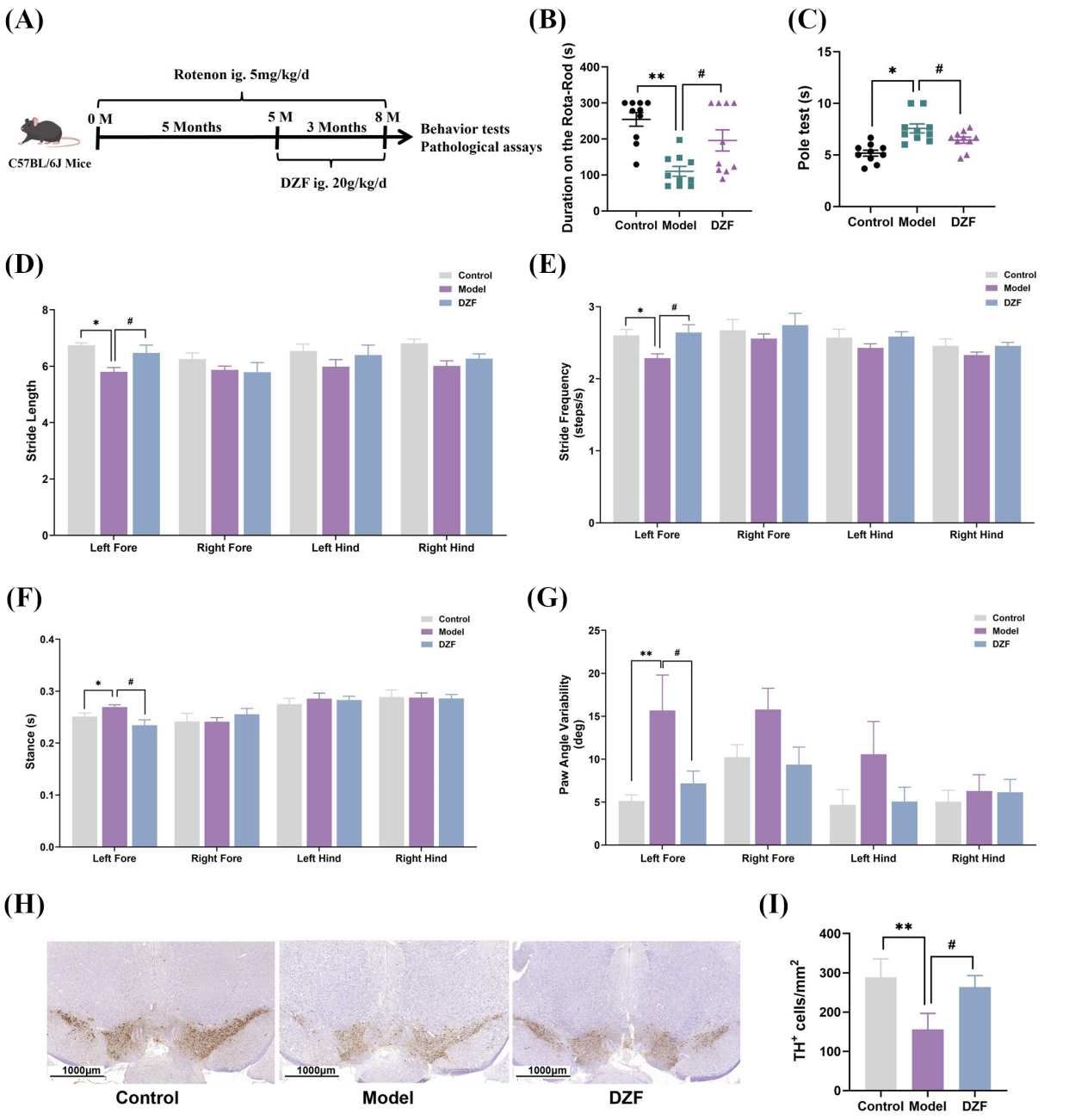


**Figure 2. Effects of DZF on motor dysfunction and nigral TH immunoreactivity in rotenone-induced PD-like mice.** (**A**) Experimental timeline showing that rotenone administration continued through month 8 and that DZF treatment began in month 6. DZF improved rotarod performance (**B**), pole-test performance (**C**), and gait parameters (**D-G**). DZF also attenuated the reduction in TH-positive cell density and TH immunoreactivity in the substantia nigra pars compacta (**H-I**). Data are presented as mean ± SEM. For (**B-G**), $n = 10$ per group; for (**H-I**), $n = 3$ per group. $^{*}P < 0.05$, $^{**}P < 0.01$ compared with the control group; $^{\#}P < 0.05$ compared with the model group.

tryptophan-related metabolites revealed alterations in L-tryptophan and 5-hydroxy-L-tryptophan (5-HTP), key intermediates involved in serotonin biosynthesis. These findings suggested a potential involvement of intestinal tryptophan metabolism in the effects of DZF and provided a basis for further investigation of TPH1/5-HT-related signaling (Figure 6C). Furthermore, Spearman correlation analysis demonstrated significant associations between differential bacterial genera and tryptophan-related metabolites. Notably, Pedobacter and Anaerotruncus showed significant correlations with these metabolites (Figure 6D). Collectively, these findings suggest that DZF-induced microbiota remodeling is associated with alterations in tryptophan-related metabolic profiles, highlighting a potential microbiota–metabolite interaction underlying the effects of DZF.

### 3.7. DZF modulates intestinal TPH1/5-HT-related signaling in rotenone-induced PD-like mice

Based on the alterations in tryptophan-related

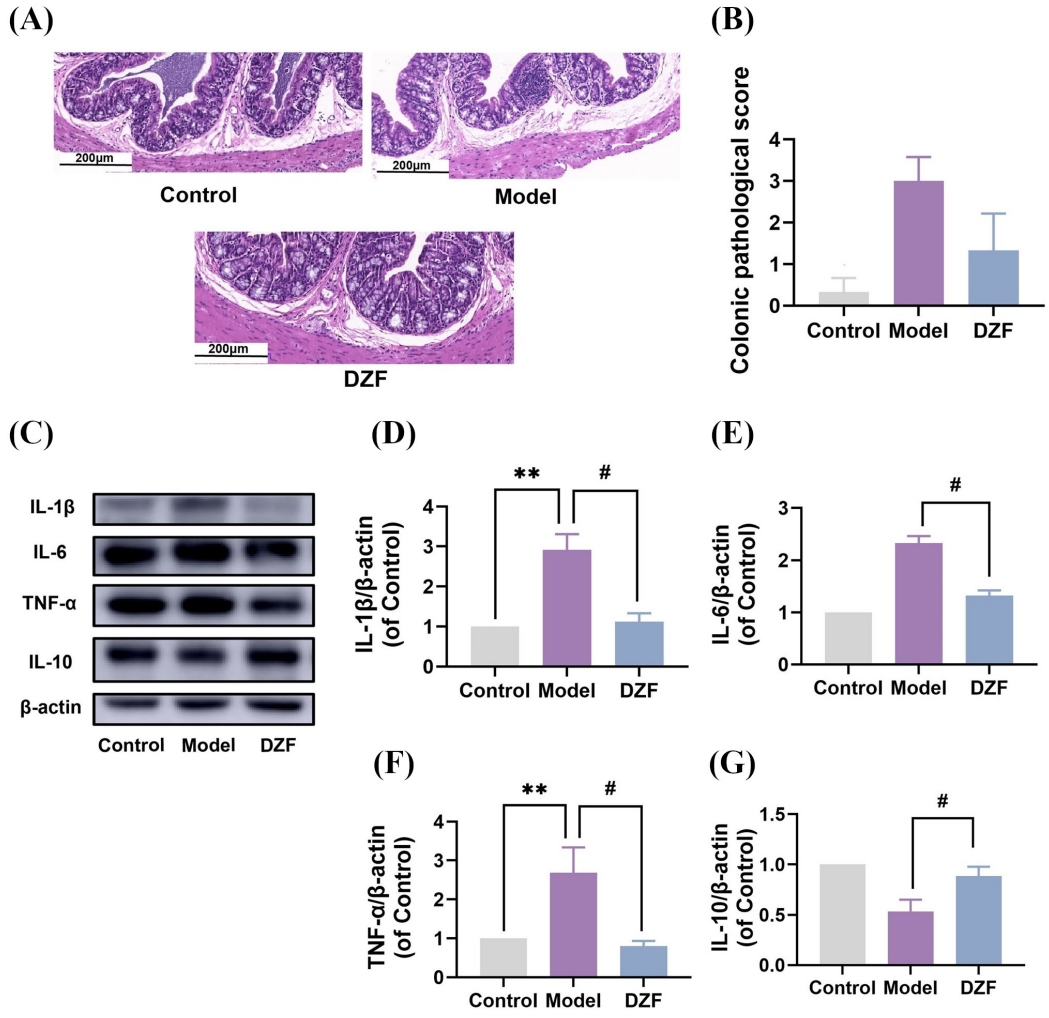


**Figure 3. DZF ameliorates colonic histopathology and attenuates intestinal inflammation in PD mice.** DZF treatment showed a tendency to alleviate colonic histopathological damage, as evaluated by H&E staining (**A**) and corresponding histological injury scores (**B**). Western blot analysis showed that DZF treatment modulated the colonic inflammatory microenvironment by decreasing the protein expression of pro-inflammatory cytokines, including IL-1β (**D**), IL-6 (**E**), and TNF-α (**F**), while upregulating the anti-inflammatory cytokine IL-10 (**G**). Representative western blot images are shown in (**C**). Data are presented as mean ± SEM, $n = 3$ per group. The colonic pathological scores (**B**) were analyzed using the Kruskal–Wallis test followed by Dunn's multiple comparisons test. $^{*}P < 0.05$, $^{**}P < 0.01$ compared with the control group; $^{\#}P < 0.05$ compared with the model group.

metabolites identified by metabolomics analysis, we further investigated whether DZF treatment affected intestinal TPH1/5-HT-related signaling. TPH1 is the rate-limiting enzyme responsible for converting L-tryptophan into 5-hydroxy-L-tryptophan (5-HTP), an intermediate precursor involved in 5-HT biosynthesis. Immunofluorescence staining showed that rotenone exposure significantly increased TPH1 fluorescence intensity in the colon, whereas DZF treatment markedly reduced TPH1 expression (Figure 7A-B). Similarly, the expression of the serotonin receptor 5-HT3A was elevated in the model group and decreased following DZF administration (Figure 7C-D). Consistently, qPCR analysis further demonstrated that intestinal TPH1 mRNA expression was increased after rotenone exposure and was attenuated by DZF treatment (Figure 7E). In addition, western blot analysis revealed that DZF treatment reduced the elevated expression of Clathrin induced by rotenone exposure (Figure 7F-G). Collectively, these findings suggest that DZF may regulate intestinal TPH1/5-HT-related signaling and associated intracellular transport processes in rotenone-induced PD-like mice.

### 3.8. Molecular docking predicts potential interactions between DZF components and TPH1

To further validate the mechanism of action of DZF, molecular docking analysis was performed between TPH1 and the intestinal active components of DZF identified in our previous study. Figure 8A presents a heatmap of the binding affinities of ten major intestinal active components of DZF with TPH1. Among them, 6-shogaol, 10-gingerdione, 10-gingerol, and 4-gingerol exhibited stable binding conformations and low binding energies with TPH1 (Figure 8B). These findings suggest

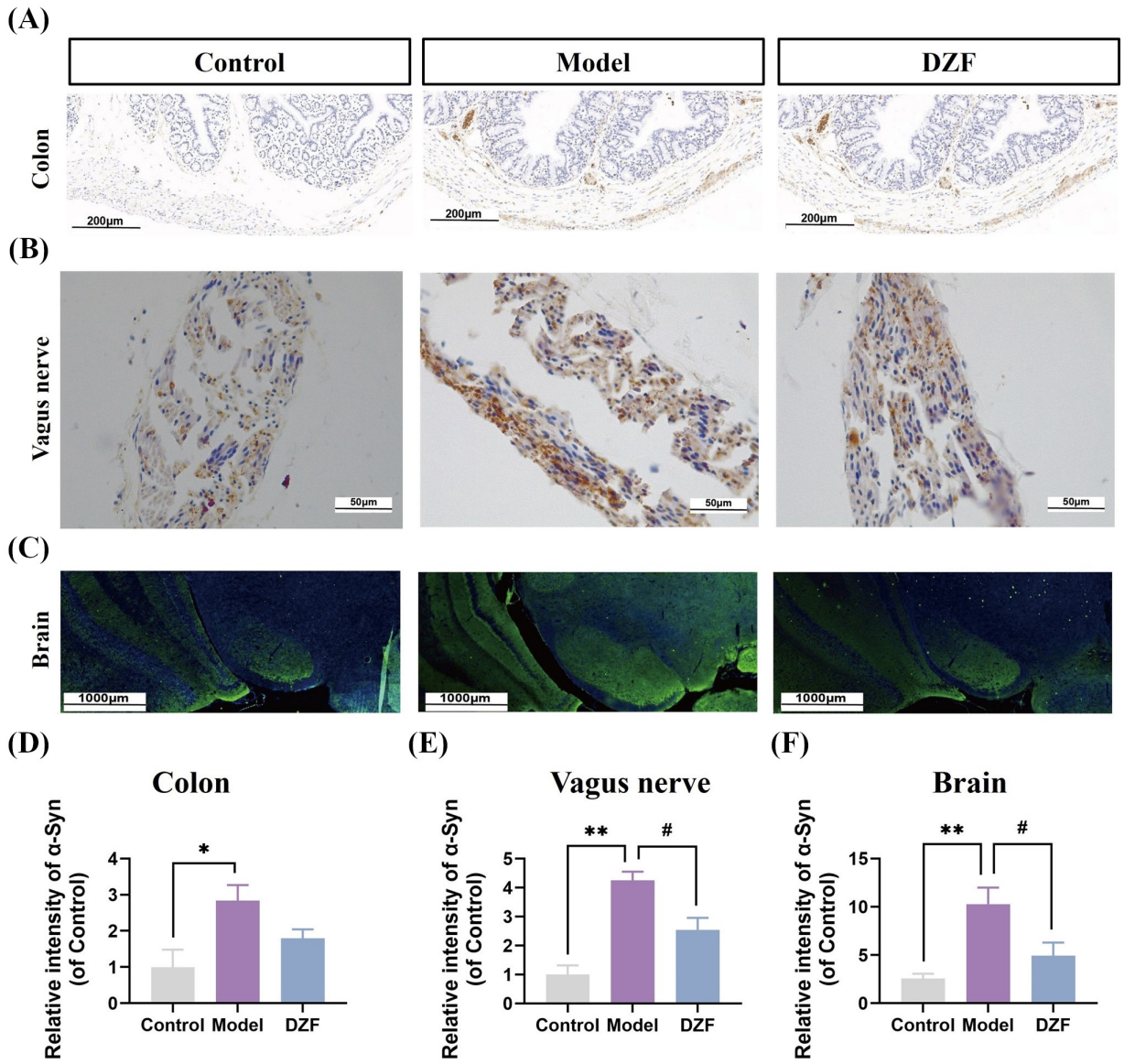


**Figure 4. Effects of DZF on α-Syn-related pathology along the gut-brain axis.** Representative immunohistochemical/immunofluorescence images and quantitative analyses show α-Syn expression in the colon (**A**, **D**), vagus nerve (**B**, **E**), and brain (**C**, **F**). DZF significantly reduced α-Syn expression in the vagus nerve and brain, whereas the reduction in the colon represented a non-significant downward trend. Data are presented as mean ± SEM, $n = 3$ per group. $^{*}P < 0.05$, $^{**}P < 0.01$ compared with the control group; $^{\#}P < 0.05$ compared with the model group.

that several intestinally active components of DZF may have potential interactions with TPH1, supporting the possible involvement of TPH1-related signaling in the biological effects of DZF.

## 4. Discussion

In recent years, the gut-brain axis has emerged as an important regulatory network in PD pathogenesis, linking intestinal homeostasis with central neurodegenerative changes (*28-30*). Within this framework, our findings indicate that DZF ameliorates established rotenone-induced PD-like phenotypes and may act by modulating the intestinal TPH1/5-HT-related pathway and α-Syn-related pathology along the gut-brain axis. These observations support further investigation of gut-targeted mechanisms underlying the effects of traditional Chinese medicine in PD models.

The low-dose rotenone gavage model employed in this study provides a unique experimental platform for investigating enterogenic PD. Unlike systemic neurotoxins, rotenone (5 mg/kg) is highly lipophilic and poorly absorbed from the gastrointestinal tract, allowing it to act preferentially on the gut without direct entry into the central nervous system (*27*). This rotenone induced enterogenic PD model has been widely used in related research (*31,32*). Based on this, we designed a gradient administration regimen of 1, 3, and 5 months. The results showed that after five months of gavage, the model mice exhibited sequential accumulation of pathological

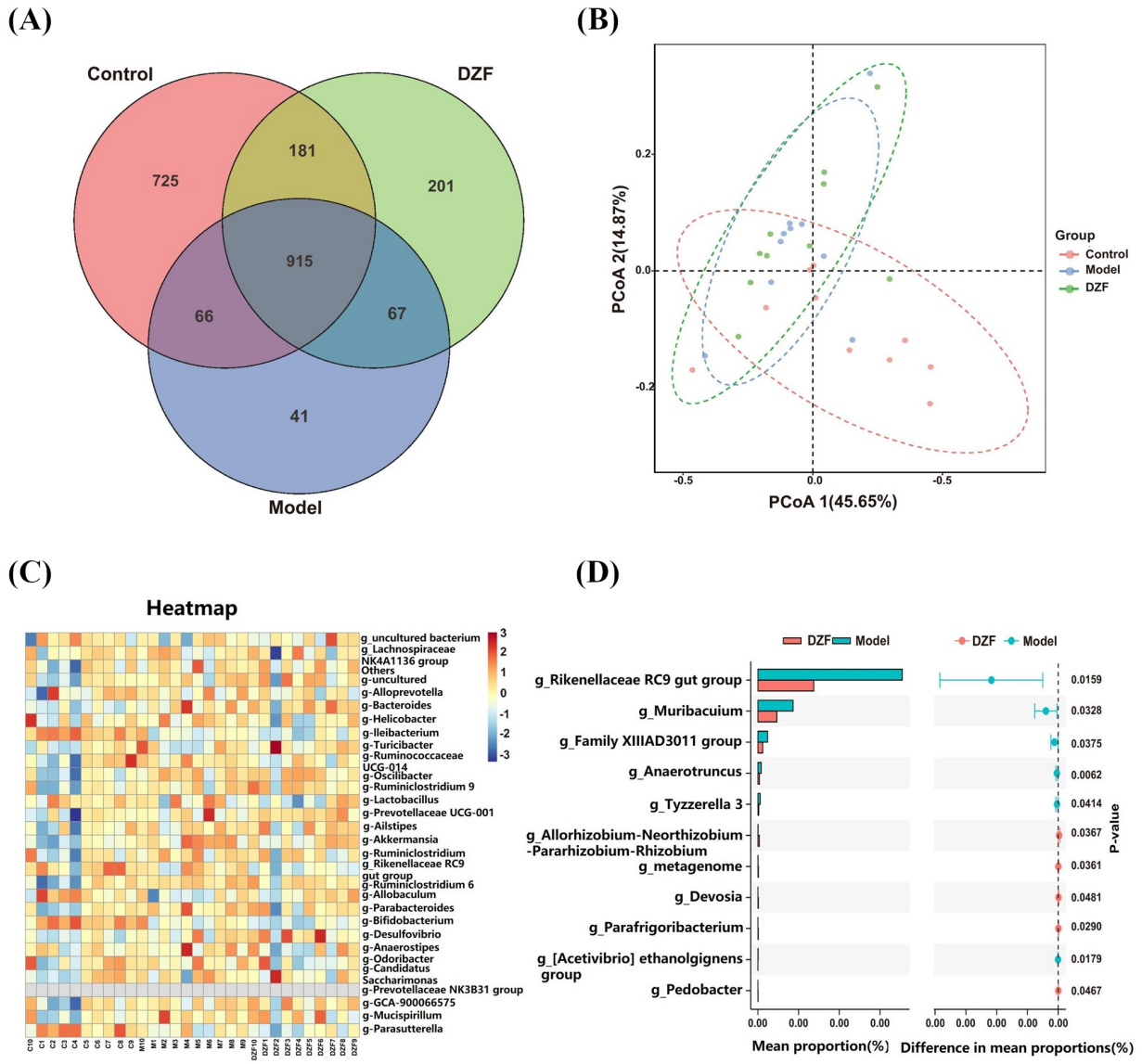


**Figure 5. DZF intervention alters gut microbiota composition in PD-like mice.** The Venn diagram (**A**) summarizes shared and unique OTUs among the control, model, and DZF groups. PCoA based on unweighted UniFrac distance (**B**) shows differences in microbial-community structure. The heatmap (**C**) and between-group genus-level differential-abundance analysis (**D**) identify genera that differ between the model and DZF groups; panel D presents mean relative abundance, the between-group difference, and the corresponding *P* value.

α-Syn in the colon, vagus nerve, and substantia nigra, accompanied by motor dysfunction, thereby faithfully recapitulating the temporal "gut→vagus→brain" pathological cascade. Importantly, this model closely replicates the "body first" PD subtype, which accounts for approximately 46% of patients presenting with early gastrointestinal dysfunction (*33*), providing an ideal animal platform for evaluating early intervention strategies targeting the gut.

In this study, low-dose rotenone gavage successfully induced PD-like phenotypes accompanied by pronounced intestinal microenvironment disturbances, including colonic inflammatory-cell infiltration, an imbalance in inflammatory cytokine profiles characterized by increased pro-inflammatory cytokines IL 1β, IL 6, and TNF α and decreased IL-10, as well as gut microbiota dysbiosis. These findings are consistent with those of Sampson *et al.* (*12*), who demonstrated that gut microbiota dysbiosis is necessary for motor deficits and neuroinflammation in PD models (*12*). Following DZF intervention, intestinal pathological damage and inflammatory abnormalities were markedly alleviated, accompanied by restoration of gut microbial homeostasis, improved motor performance, and attenuation of the reduction in nigral TH-positive cell density. Together, these results suggest that DZF exerts protective effects across the gut–brain axis by simultaneously improving intestinal microenvironmental disorders and central PD-like pathological changes.

Pathological α Syn transmission from the gut to the brain *via* the vagus nerve is a hallmark event in enterogenic PD (*7-10*). Therefore, we further investigated

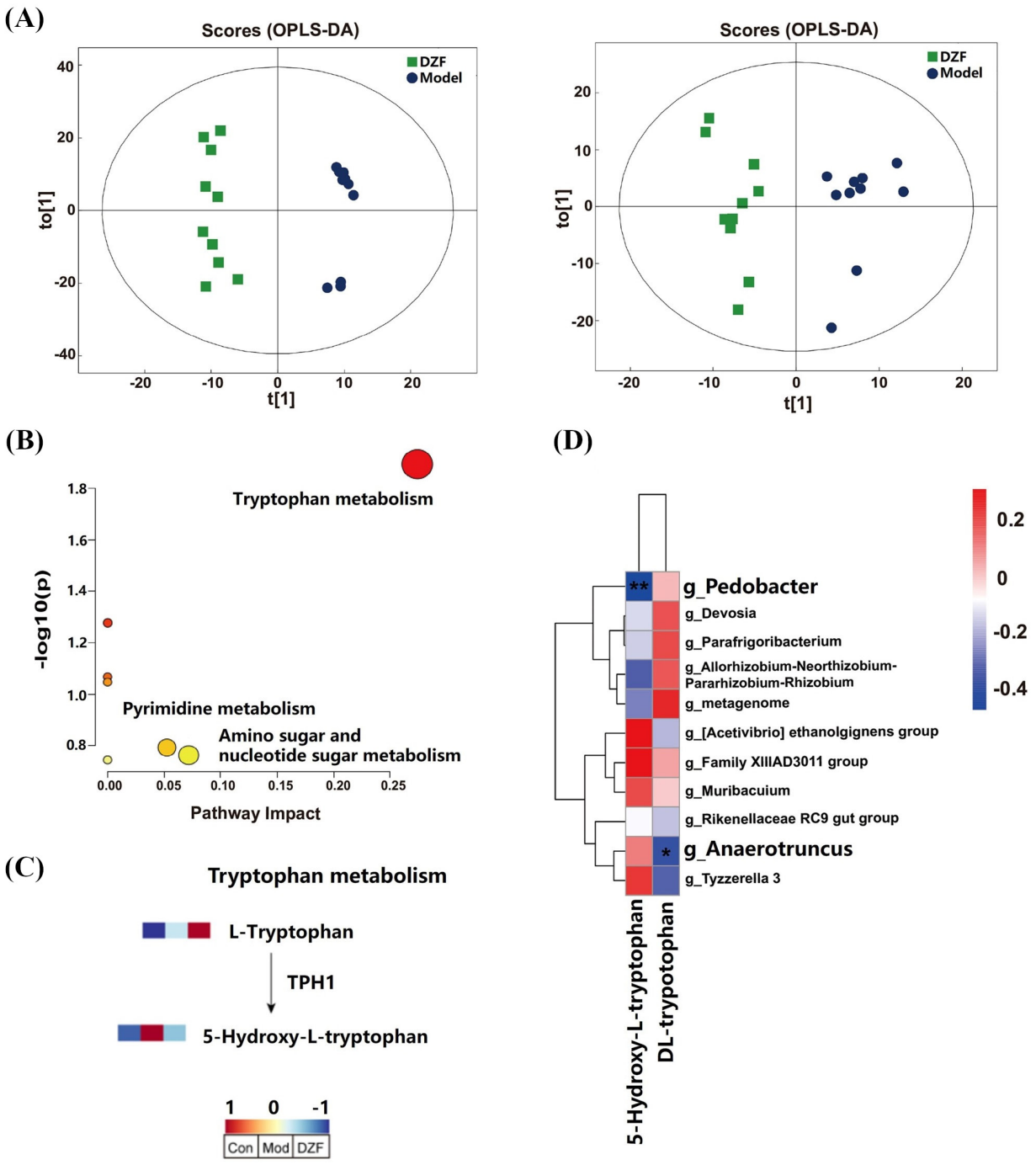


**Figure 6. DZF-associated changes in fecal metabolites and tryptophan-related metabolism in PD-like mice.** The OPLS-DA score plot (**A**) shows separation between the DZF and model groups. Pathway enrichment analysis (**B**) revealed that tryptophan metabolism was significantly enriched among the altered metabolic pathways and exhibited a relatively high pathway-impact value. The L-tryptophan–TPH1–5-hydroxytryptamine (5-HT) metabolic axis was summarized based on the identified tryptophan-related metabolites (**C**). Spearman correlation analysis shows associations between differential genera and tryptophan-related metabolites, including significant correlations involving *Pedobacter* and *Anaerotruncus* (**D**).

the effect of DZF on α Syn transfer along the gut brain axis to clarify its gut brain mechanistic linkage. In the present study, DZF treatment markedly reduced α-Syn expression in the vagus nerve and brain, while colonic α-Syn levels also showed a decreasing trend following DZF administration. This finding is in full agreement with the Braak hypothesis (*4*) and the study by Kim *et al.* (*9*), who showed that vagotomy completely prevents α Syn propagation to the brainstem. Of note, although colonic α Syn showed a clear decreasing trend in our study, the reduction did not reach statistical significance, possibly due to the small sample size ($n$ = 3). These findings suggest that DZF may alleviate α-Syn-related pathology along the gut–vagus–brain axis, potentially

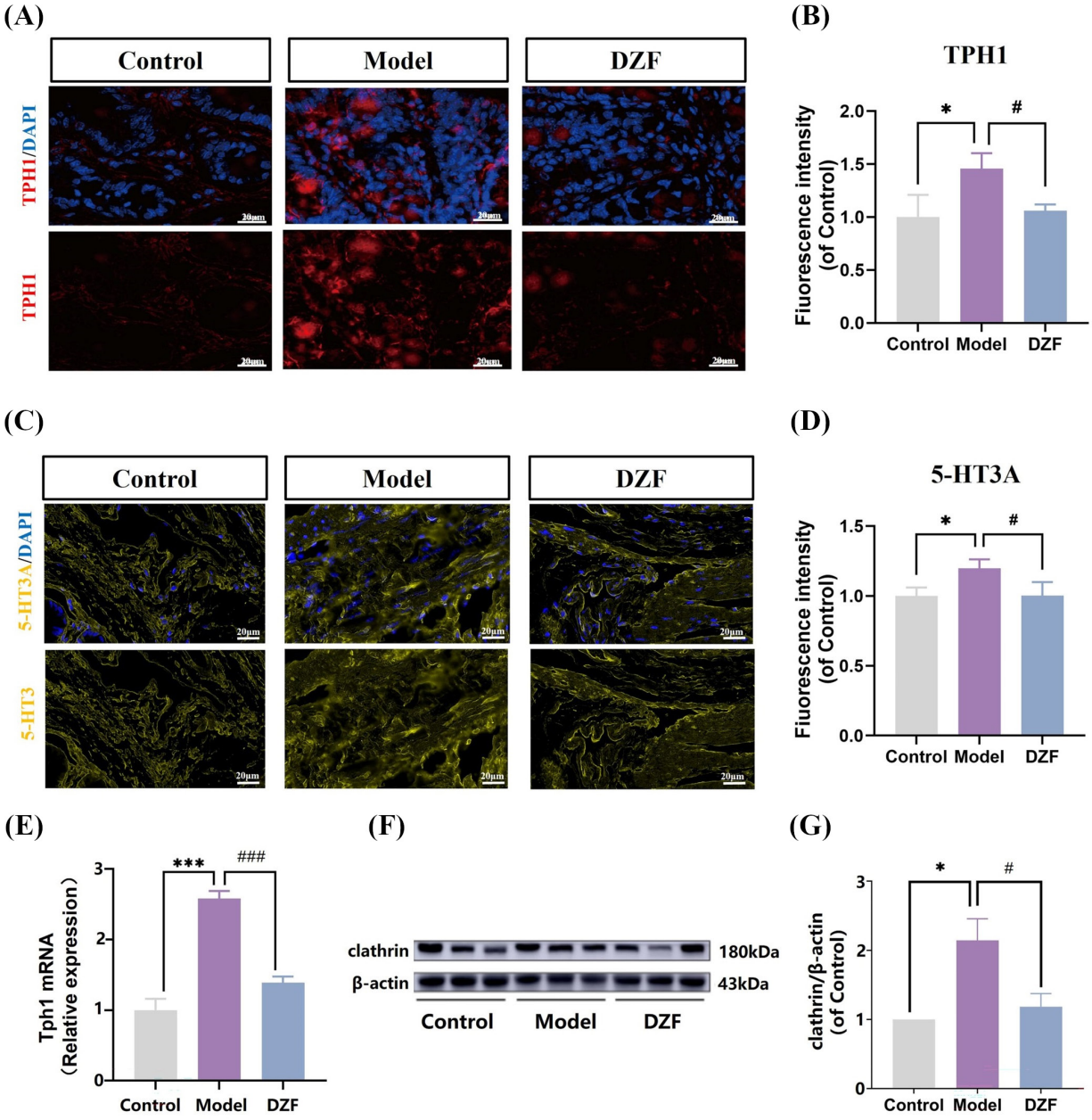


**Figure 7. Immunofluorescence staining and quantification showed that rotenone exposure increased TPH1 fluorescence intensity in the colonic epithelium, whereas DZF treatment attenuated this increase (A-B).** Similarly, 5-HT3A expression was elevated in the model group and reduced following DZF administration (**C-D**). qPCR analysis further confirmed the changes in intestinal TPH1 mRNA expression after rotenone exposure and DZF treatment (**E**). Western blot analysis showed that DZF treatment decreased the rotenone-induced elevation of Clathrin expression (**F-G**). Data are presented as mean ± SEM, $n = 3$ per group. $^{*}P < 0.05$, $^{**}P < 0.01$ compared with the control group; $^{\#}P < 0.05$, $^{\#\#}P < 0.01$ compared with the model group.

affecting α-Syn accumulation and its associated pathological processes rather than directly demonstrating clearance of established intestinal α-Syn aggregates.

Of interest, untargeted metabolomics analysis revealed that tryptophan metabolism was among the metabolic pathways potentially influenced by DZF intervention. The enrichment analysis identified tryptophan metabolism as a significantly enriched pathway. Consistently, alterations in tryptophan-related metabolites, including L-tryptophan and 5-HTP, further supported the involvement of this pathway in DZF-mediated metabolic regulation. Given that the gut microbiota is considered an important upstream regulator of intestinal tryptophan metabolism (*34*), these findings suggest a potential link between microbiota remodeling and tryptophan-related metabolic changes following DZF treatment. Integrative correlation analysis of microbiome sequencing and metabolomics data showed that specific bacterial genera, particularly *Anaerotruncus* and *Pedobacter*, were significantly correlated with tryptophan-related metabolites, suggesting that DZF-induced microbiota remodeling may be associated with

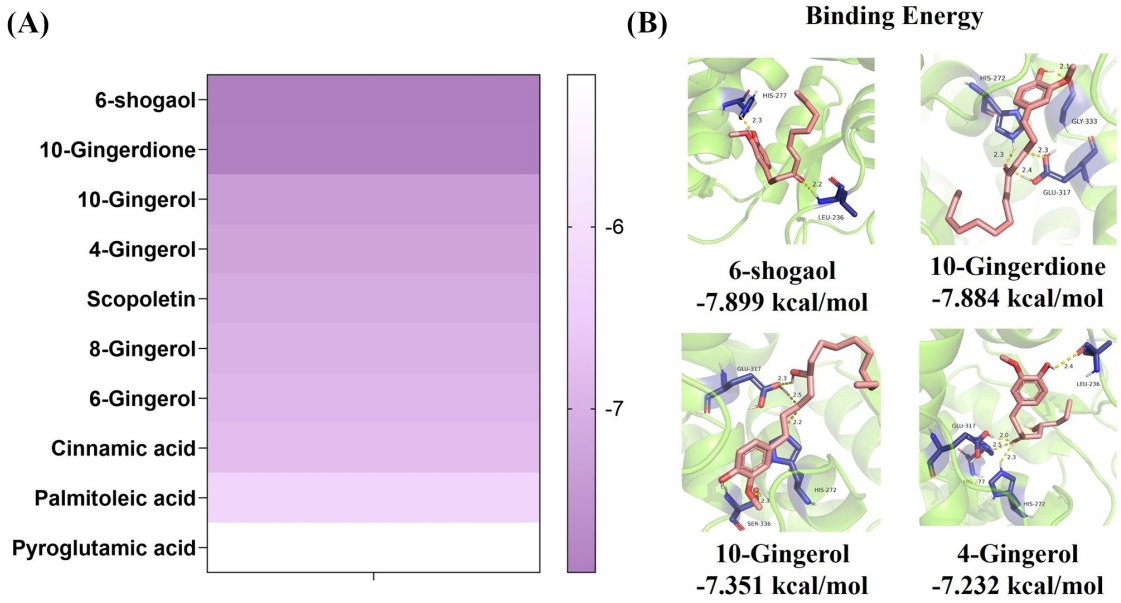


**Figure 8. Predicted molecular interactions between intestinal active components of DZF and TPH1.** (**A**) Heatmap showing the predicted binding energies of ten intestinal active components of DZF with TPH1 based on molecular docking analysis. (**B**) Representative predicted binding poses of 6-shogaol, 10-gingerdione, 10-gingerol, and 4-gingerol with TPH1.

changes in the intestinal tryptophan metabolic network. Literature reports indicate that *Anaerotruncus* is enriched in the gut of PD patients and is associated with motor and non-motor symptoms (*35*), whereas the functional significance of *Pedobacter* remains to be further explored. These findings suggest that DZF may influence host metabolic regulation through microbiota-associated modulation of tryptophan metabolism.

It has been reported that approximately 95% of peripheral 5 HT is synthesized by intestinal enterochromaffin cells *via* TPH1 (*34,36,37*), and 5 HT is intimately associated with α Syn pathology. Jinsmaa *et al.* found that the 5 HT metabolite 5 hydroxyindole acetaldehyde (5 HIAL) potently promotes α Syn oligomerization; Tripathi *et al.* reported that a 5 HT1b/1d receptor agonist reduces α Syn deposition in the brain of PD rats. Mechanistically, 5 HT promotes Clathrin mediated endocytosis (*38-40*), a key pathway for α Syn entry into neurons. Based on the alterations in L-tryptophan and 5-HTP identified by metabolomics, we further examined intestinal TPH1/5-HT-related signaling. DZF treatment reduced colonic TPH1 protein expression and mRNA levels, accompanied by decreased 5-HT3A expression and attenuation of rotenone-induced Clathrin upregulation (Figure 7). Together, these findings suggest that DZF may modulate intestinal TPH1/5-HT-related signaling and associated intracellular transport processes, thereby contributing to the improvement of gut-derived PD-like pathology. However, because intestinal 5-HT levels and TPH1 enzymatic activity were not directly measured, our findings indicate a potential involvement of TPH1/5-HT-related signaling rather than demonstrating direct regulation of 5-HT synthesis or α-Syn propagation. This suggests that the role of intestinal 5-HT signaling in PD may extend beyond its traditional association with constipation (*41*).

Furthermore, a recent study reported that the antidepressant vortioxetine alleviates rotenone induced intestinal inflammation by enhancing 5 HT signaling (*42*), which appears opposite to the 5 HT suppressing effect of DZF. This apparent contradiction may be explained by the biphasic or context dependent nature of 5 HT signaling: under physiological conditions, appropriate levels of 5 HT help maintain intestinal homeostasis and motor function, whereas in the chronic inflammatory microenvironment of PD, excessive 5 HT may drive α Syn propagation by overactivating endocytosis or promoting immune cell activation. Thus, both enhancing 5 HT (to correct a possible deficiency) and inhibiting 5 HT (to curb excess) may be beneficial under different pathological states. The action of DZF tends to restore 5 HT system homeostasis rather than simply suppressing or activating it. This mechanism still requires further validation in enterochromaffin cell neuron co culture systems.

Previous pharmacokinetic studies have shown that some components of DZF can enter the brain and exert neuroprotective effects. In contrast, other components remain as parent compounds in feces and intestinal contents after administration, exhibiting an "intestinal retention" property (*26*). This phenomenon suggests that these components may exert biological effects through local modulation of intestinal functions. Based on this observation, we further performed molecular docking analysis between these intestinally retained components and TPH1. Several gingerol-like compounds, including 6-shogaol, 10-gingerdione, 10-gingerol, and 4-gingerol, exhibited favorable predicted binding affinities with

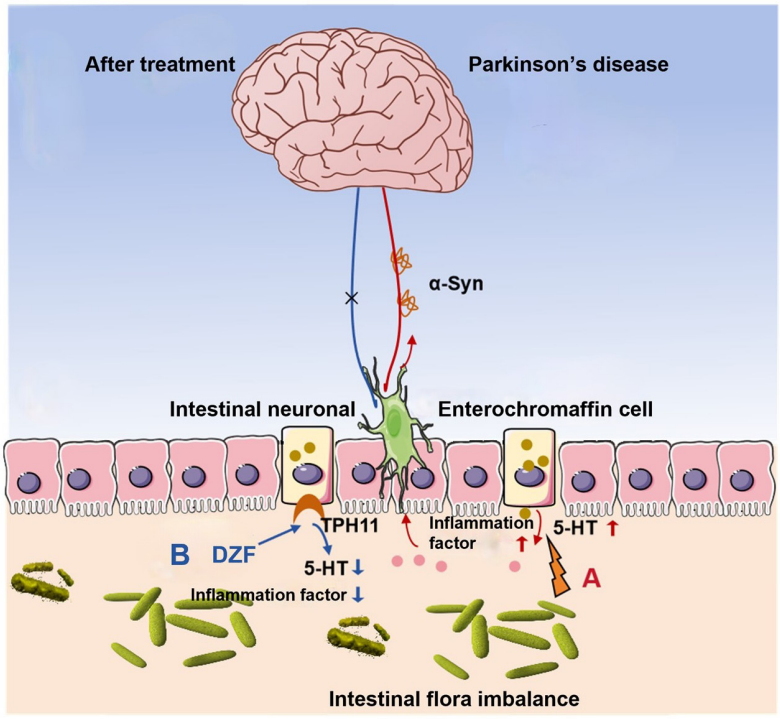


**Figure 9. Proposed mechanism underlying the protective effects of DZF against rotenone-induced PD-like pathology through gut-brain axis regulation.**

TPH1 (Figure 8). These findings suggest that intestinally retained DZF components may potentially participate in the regulation of TPH1-related signaling and contribute to the intestinal effects of DZF. However, molecular docking analysis alone cannot establish direct binding, TPH1 inhibition, effective intestinal exposure, or therapeutic efficacy. Further biophysical binding assays, enzyme activity measurements, and intestinal pharmacokinetic studies are required to validate these potential interactions.

This study provides evidence that DZF alleviates PD-like pathology through modulation of gut-related abnormalities and TPH1/5-HT-related signaling, while also suggesting a potential role for the gut microbiota–tryptophan metabolism network in its therapeutic effects. However, the precise mechanisms linking intestinal 5-HT-related signaling with α-Syn pathology remain to be further clarified. Future studies involving direct measurement of intestinal 5-HT levels, evaluation of TPH1 enzymatic activity, and functional validation of 5-HT-mediated effects on α-Syn-related processes will help elucidate this mechanism. In addition, the microbiome and metabolomics analyses performed in this study reveal associations rather than causal relationships. Longitudinal studies and interventions such as fecal microbiota transplantation will be valuable for determining whether specific microbial taxa, including *Anaerotruncus* and *Pedobacter*, directly contribute to tryptophan metabolism and DZF-mediated effects. These investigations will further advance our understanding of the gut–brain regulatory mechanisms underlying the protective effects of DZF.

It should be noted that the present study was conducted using a rotenone-induced gut-origin PD mouse model, which reproduces only certain pathological features of human PD and cannot fully recapitulate the complexity of the human disease. Therefore, the neuroprotective effects of DZF require further validation of their efficacy and safety in future clinical studies.

## 5. Conclusion

In conclusion, this study demonstrates that DZF ameliorates established rotenone-induced PD-like motor dysfunction, intestinal abnormalities, and nigral pathological changes in mice. The findings suggest that intestinally retained DZF components may contribute to these protective effects through modulation of gut microbiota, tryptophan-related metabolism, and TPH1/5-HT-related signaling, accompanied by reduced intestinal inflammation and α-Syn-associated pathology along the gut–brain axis. Molecular docking analysis identified several DZF-derived compounds with potential interactions with TPH1, providing a basis for further investigation of their molecular mechanisms. Overall, this study highlights the potential role of gut-targeted regulation in the protective effects of DZF against PD-like pathology and provides new insights into the gut–brain mechanisms underlying traditional Chinese medicine intervention (Figure 9).

**Acknowledgements**

The authors would like to express their sincere appreciation to the State Key Laboratory of Component-based Chinese Medicine at Tianjin University of Traditional Chinese Medicine for providing essential experimental platform support. We also thank the technicians at the Animal Experiment Center for their assistance with animal care and behavioral testing. Our gratitude further extends to all members of the research group for their valuable discussions and technical support throughout the study.

*Funding*: The authors gratefully acknowledge the financial support from the Tianjin Key Program in Traditional Chinese Medicine (Grant No. 2024008) and the Natural Science Foundation of Henan Province (Grant No. 252300420528), which made this study possible.

*Conflict of Interest*: The authors have no conflicts of interest to disclose.

**References**

1. Jankovic J, Tan EK. Parkinson's disease: etiopathogenesis and treatment. J Neurol Neurosurg Psychiatry. 2020; 91:795-808.
2. Armstrong MJ, Okun MS. Diagnosis and treatment of Parkinson disease: A review. JAMA. 2020; 323:548-560.
3. Lee JY, Martin-Bastida A, Murueta-Goyena A, Gabilondo I, Cuenca N, Piccini P, Jeon B. Multimodal brain and retinal imaging of dopaminergic degeneration in Parkinson disease. Nat Rev Neurol. 2022; 18:203-220.
4. Braak H, Del Tredici K, Rüb U, de Vos RAI, Jansen Steur ENH, Braak E. Staging of brain pathology related to sporadic Parkinson's disease. Neurobiol Aging. 2003; 24:197-211.
5. Warnecke T, Schäfer KH, Claus I, Del Tredici K, Jost WH. Gastrointestinal involvement in Parkinson's disease: pathophysiology, diagnosis, and management. NPJ Parkinsons Dis. 2022; 8:31.
6. Zhang J, Shi M, Zhang Q, Chen Y, Yin X, Wang X, Zhang Y. Association between constipation and the risk of Parkinson's disease among participants in the UK Biobank. Neuroepidemiology. 2025; 59:381-390.
7. Uemura N, Yagi H, Uemura MT, Hatanaka Y, Yamakado H, Takahashi R. Inoculation of α-synuclein preformed fibrils into the mouse gastrointestinal tract induces Lewy body-like aggregates in the brainstem *via* the vagus nerve. Mol Neurodegener. 2018; 13:21.
8. Holmqvist S, Chutna O, Bousset L, Aldrin-Kirk P, Li W, Björklund T, Wang ZY, Roybon L, Melki R, Li JY. Direct evidence of Parkinson pathology spread from the gastrointestinal tract to the brain in rats. Acta Neuropathol. 2014; 128:805-820.
9. Kim S, Kwon SH, Kam TI, *et al.* Transneuronal propagation of pathologic α-synuclein from the gut to the brain models Parkinson's disease. Neuron. 2019; 103:627-641.e7.
10. Ahn EH, Kang SS, Liu X, Chen G, Zhang Z, Chandrasekharan B, Alam AM, Neish AS, Cao X, Ye K. Initiation of Parkinson's disease from gut to brain by δ-secretase. Cell Res. 2020; 30:70-87.
11. Limanaqi F, Zecchini S, Ogno P, Artusa V, Fenizia C, Saulle I, Vanetti C, Garziano M, Strizzi S, Trabattoni D, Clerici M, Biasin M. Alpha-synuclein shapes monocyte and macrophage cell biology and functions by bridging alterations of autophagy and inflammatory pathways. Front Cell Dev Biol. 2024; 12:1421360.
12. Sampson TR, Debelius JW, Thron T, *et al.* Gut microbiota regulate motor deficits and neuroinflammation in a model of Parkinson's disease. Cell. 2016; 167:1469-1480.e12.
13. Tan AH, Lim SY, Lang AE. The microbiome-gut-brain axis in Parkinson disease: from basic research to the clinic. Nat Rev Neurol. 2022; 18:476-495.
14. Wang L, Cui Y, Han B, Du Y, Salewala KS, Wang S, Zhao W, Zhang H, Wang S, Xu X, Ma J, Zhu Y, Tuo H. Gut microbiota and Parkinson's disease. Chin Med J (Engl). 2025; 138:289-297.
15. Bedarf JR, Hildebrand F, Coelho LP, Sunagawa S, Bahram M, Goeser F, Bork P, Wüllner U. Functional implications of microbial and viral gut metagenome changes in early stage L-DOPA-naïve Parkinson's disease patients. Genome Med. 2017; 9:39.
16. Liang Y, Zhao Y, Fasano A, Su CW. Gut permeability and microbiota in Parkinson's disease: mechanistic insights and experimental therapeutic strategies. Int J Mol Sci. 2025; 26:9593.
17. Radisavljevic N, Metcalfe-Roach A, Cirstea M, Tabusi MM, Bozorgmehr T, Bar-Yoseph H, Finlay BB. Microbiota-mediated effects of Parkinson's disease medications on Parkinsonian non-motor symptoms in male transgenic mice. mSphere. 2024; 9:e0037923.
18. Ramadan ME, Mostafa TM, Ghali AA, El-Afify DR. Randomized controlled trial evaluating synbiotic supplementation as an adjuvant therapy in the treatment of Parkinson's disease. Inflammopharmacology. 2025; 33:3897-3908.
19. Leta V, Zinzalias P, Batzu L, *et al.* Effects of a four-strain probiotic on gut microbiota, inflammation, and symptoms in Parkinson's disease: A randomized clinical trial. Mov Disord. 2025; 40:2710-2721.
20. Wang J, Xue L, Zhang M, Shen P, Zhao W, Tong Q, Wu S, Dai W, Yang X, Wang H. Colonoscopic fecal microbiota transplantation for mild-to-moderate Parkinson's disease: a randomized controlled trial. Brain Behav Immun. 2025; 130:106086.
21. DuPont HL, Suescun J, Jiang ZD, Brown EL, Essigmann HT, Alexander AS, DuPont AW, Iqbal T, Utay NS, Newmark M, Schiess MC. Fecal microbiota transplantation in Parkinson's disease: a randomized repeat-dose, placebo-controlled clinical pilot study. Front Neurol. 2023; 14:1104759.
22. Zhang R, Feng R, Wang J, Chen Y, Liu H, Zhu Q, Tian H, Qin C, Teng J, Tang B, Wu M, Zeng J, Wu E, Ding X, Wang X. Gut microbiota modulation *via* repeated donor fecal transplantation improves motor and gastrointestinal symptoms in drug-naïve Parkinson's disease: a randomized phase 2 trial. Signal Transduct Target Ther. 2026; 11:94.
23. Park JC, Chang L, Kwon HK, Im SH. Beyond the gut: decoding the gut-immune-brain axis in health and disease. Cell Mol Immunol. 2025; 22:1287-1312.
24. Shen Q, Liu RT, Wang Y, Zhuang PW, Yang WH, Guo H. Duzhong Fang ameliorates cognitive impairment of Parkinsonian mice by suppressing neuronal apoptotic pathway. Drug Discov Ther. 2024; 18:229-239.

25. Li L, Fan S, Zhang W, Li D, Yang Z, Zhuang P, Han J, Guo H, Zhang Y. Duzhong Fang attenuates the POMC-derived neuroinflammation in Parkinsonian mice. J Inflamm Res. 2021; 14:3261-3276.
26. Song L, Yin H, Han R, Li J, Ma N, Wang Y, Guo H. Metabolism of Du Zhong Formula in rats using UPLC-Q-TOF/MS. J Mass Spectrom. 2022; 57:e4795.
27. Pan-Montojo F, Anichtchik O, Dening Y, Knels L, Pursche S, Jung R, Jackson S, Gille G, Spillantini MG, Reichmann H, Funk RHW. Progression of Parkinson's disease pathology is reproduced by intragastric administration of rotenone in mice. PLoS One. 2010; 5:e8762.
28. Hajare S, Kulkarni YA. Parkinson's disease and the gut-brain connection: Unveiling pathways, mechanisms and promising therapies. Brain Res. 2025; 1868:149975.
29. Jin X, Wei J, Min X, Fan Y, Yuan Z, Du Z, Su Z, Xun T, Du Q, Liang T, He X, Tang W. Gut microbiota and Parkinson's disease: exploring pathogenesis and potential therapeutic strategies from a gut-brain axis perspective. iScience. 2026; 29:114185.
30. Ratajczyk K, Kaczorowska E, Wyka K, Tarasiuk-Zawadzka A, Fichna J, Gajos A. Gut-brain signaling in Parkinson's disease: a narrative review. Int J Mol Sci. 2026; 27:3531.
31. Klingelhoefer L, Reichmann H. Pathogenesis of Parkinson disease: the gut-brain axis and environmental factors. Nat Rev Neurol. 2015; 11:625-636.
32. Pan-Montojo F, Schwarz M, Winkler C, Arnhold M, O'Sullivan GA, Pal A, Said J, Marsico G, Verbavatz JM, Rodrigo-Angulo M, Gille G, Funk RHW, Reichmann H. Environmental toxins trigger PD-like progression *via* increased alpha-synuclein release from enteric neurons in mice. Sci Rep. 2012; 2:898.
33. Camacho M, Greenland JC, Daruwalla C, Scott KM, Patel B, Apostolopoulos D, Ribeiro J, O'Reilly M, Hu MT, Williams-Gray CH. The profile of gastrointestinal dysfunction in prodromal to late-stage Parkinson's disease. NPJ Parkinsons Dis. 2025; 11:123.
34. Agus A, Planchais J, Sokol H. Gut microbiota regulation of tryptophan metabolism in health and disease. Cell Host Microbe. 2018; 23:716-724.
35. Heintz-Buschart A, Pandey U, Wicke T, Sixel-Döring F, Janzen A, Sittig-Wiegand E, Trenkwalder C, Oertel WH, Mollenhauer B, Wilmes P. The nasal and gut microbiome in Parkinson's disease and idiopathic rapid eye movement sleep behavior disorder. Mov Disord. 2018; 33:88-98.
36. Hummerich R, Schloss P. Serotonin: more than a neurotransmitter: transglutaminase-mediated serotonylation of C6 glioma cells and fibronectin. Neurochem Int. 2010; 57:67-75.
37. Wei L, Singh R, Ghoshal UC. Enterochromaffin cells-gut microbiota crosstalk: underpinning the symptoms, pathogenesis, and pharmacotherapy in disorders of gut-brain interaction. J Neurogastroenterol Motil. 2022; 28:357-375.
38. Jinsmaa Y, Cooney A, Sullivan P, Sharabi Y, Goldstein DS. The serotonin aldehyde, 5-HIAL, oligomerizes alpha-synuclein. Neurosci Lett. 2015; 590:134-137.
39. Tripathi AS, Fatima N, Tripathi P, Tripathi R, Alka, Zaki MEA, Mohapatra L, Yasir M, Maurya RK. Beneficial effect of 5-HT1b/1d agonist on Parkinson's disease by modulating glutamate and reducing deposition of α-synuclein. J Biochem Mol Toxicol. 2024; 38:e23627.
40. Shearer LJ, Petersen NO, Woodside MT. Internalization of α-synuclein oligomers into SH-SY5Y cells. Biophys J. 2021; 120:877-885.
41. Miquel-Rio L, Sarriés-Serrano U, Pavia-Collado R, Meana JJ, Bortolozzi A. The role of α-synuclein in the regulation of serotonin system: physiological and pathological features. Biomedicines. 2023; 11:541.
42. Samur DN, Yıldırım S, Maytalman E, Kalay M, Tanrıöver G, Özbey G. Vortioxetine attenuates rotenone-induced enteric neuroinflammation *via* modulation of the TLR2/S100B/RAGE signaling pathway in a rat model of Parkinson's disease. Neuropharmacology. 2025; 271:110385.

Received June 25, 2025; Revised August 20, 2026; Accepted August 21, 2026.

**Address correspondence to:*
Pengwei Zhuang, First Teaching Hospital of Tianjin University of Traditional Chinese Medicine, Tianjin 300381, China.
E-mail: zhuangpengwei@163.com

Hong Guo, State Key Laboratory of Component-based Chinese Medicine, Tianjin University of Traditional Chinese Medicine, Tianjin, 301617, China.
E-mail: cacti1983@163.com

Released online in J-STAGE as advance publication August 26, 2026.

*Original Article*

DOI: 10.5582/ddt.2026.01050

# Unveiling the allosteric inhibition mechanism of SARS-CoV-2 main protease and discovery of a novel allosteric inhibitor

**Quanling Zhang[1], Tingting Wen[1], Mengsi Li[1], Xiaowen Tang[1,2,*]**

[1] Department of Medicinal Chemistry, School of Pharmacy, Qingdao University, Qingdao, China;
[2] Shandong Key Laboratory of Pathogenesis and Prevention of Brain Diseases, Qingdao University, Qingdao, China.

**SUMMARY**: The severe acute respiratory syndrome coronavirus 2 (SARS-CoV-2) main protease (Mpro) is a crucial therapeutic target for anti-coronavirus disease 2019 (COVID-19) drug development, as it is essential for viral replication. However, mutations within the active site have compromised the efficacy of current competitive inhibitors, prompting the exploration of alternative inhibition strategies. In this study, we systematically investigated the allosteric inhibition mechanism of SARS-CoV-2 Mpro by pelitinib and leveraged this insight for new inhibitor discovery. Through extensive molecular dynamics simulations, we showed that pelitinib exerts allosteric inhibition *via* the L141-S144-C145-H41 interaction network: it restricts the flexibility of L141 through CH-π interactions, transmits this effect to C145 *via* S144, stabilizes the hydrogen bond between C145 and H41, and thereby reduces the flexibility of the S3 helix (residues 40–60). This series of conformational changes induces the contraction of the Mpro catalytic pocket from ~1200 Å³ to ~800 Å³, impairs substrate binding, and ultimately appears to impair Mpro activity. Based on this mechanism, we performed structure-based virtual screening and identified a novel compound (Cpd-1). Biological evaluations showed that Cpd-1 exhibits superior Mpro inhibitory activity compared to pelitinib, with negligible off-target binding to human EGFR and Myt1 kinase, low cytotoxicity (cell viability > 60% at 200 μM), and predicted inhibitory activity against clinically relevant Mpro-resistant mutants based on computational analysis. Our findings provide mechanistic insights into a key allosteric mechanism for Mpro inhibition but also provide a promising chemical scaffold for further development as an Mpro-targeting inhibitor.

***Keywords***: SARS-CoV-2 main protease, allosteric inhibition mechanism, molecular dynamics simulations

## 1. Introduction

The coronavirus disease 2019 (COVID-19) pandemic is caused by a novel human coronavirus, namely severe acute respiratory syndrome coronavirus 2 (SARS-CoV-2), which has resulted in an unprecedented number of infections and deaths globally (*1-3*). In response to this pandemic, extensive efforts have been devoted to the development of Mpro inhibitor. To date, multiple small-molecule drugs (*e.g.*, paxlovid (*4*), simnotrelvir (*5*), leritrelvir (*6*), and ensitrelvir (*7*)) and vaccines (*e.g.*, BNT162b2 (*8*), ZyCov-D (*9*), Ad5-nCov (*10*), and BBIBP-CorV (*11*)) have been approved for clinical use, contributing to the prevention and treatment of COVID-19. However, although vaccines can rapidly establish herd immunity, the inherent nature of SARS-CoV-2 as an RNA virus renders it highly prone to mutations. Such mutations significantly compromise the protective efficacy of vaccines (*12,13*), highlighting an urgent need for the development of effective small-molecule Mpro inhibitors.

SARS-CoV-2 is an enveloped, positive-sense single-stranded RNA virus classified within the genus *Betacoronavirus* of the family Coronaviridae (*14*). Its genome is approximately 30,000 nucleotides in length, sharing 79% and 50% sequence homology with severe acute respiratory syndrome coronavirus (SARS-CoV) and Middle East respiratory syndrome coronavirus (MERS-CoV), respectively (*15*). Similar to other viruses, the replication, expression, and assembly of the viral genetic material constitute the core stages of its infection cycle (*16*). Upon entry into host cells, SARS-CoV-2 releases its genomic RNA, which is then translated into polyproteins pp1a and pp1ab. These polyproteins are subsequently cleaved by papain-like protease (PLpro) and main protease (Mpro) to generate a series of non-structural proteins (Nsps), which further facilitate viral replication through assembly processes (*16,17*). Notably, Mpro is responsible for cleaving at 11 sites within the polyproteins, making it a key enzyme essential for viral replication (*16*). It is worth emphasizing that PLpro shares high structural similarity

with human deubiquitinating enzymes, raising the risk of off-target effects for its inhibitors (*12*). Conversely, Mpro has no homologous protein in human hosts (*18*), endowing it with great potential for highly selective inhibition (*19*). Thus, Mpro is recognized as an ideal therapeutic target for Mpro inhibitor development.

Current research on Mpro inhibitors primarily focuses on targeting its active site, aiming to block viral replication through direct competitive inhibition of enzymatic activity (*20*). For instance, nirmatrelvir, which exhibits potent inhibitory activity against SARS-CoV-2 Mpro, has been developed for COVID-19 treatment and received FDA approval on May 25, 2023 under the trade name Paxlovid (*4*). Other clinically approved Mpro-targeting inhibitors include simnotrelvir (*5*), leritrelvir (*6*), ensitrelvir (*7*), and atilotrelvir (*21*). However, under the selective pressure exerted by competitive inhibitors, SARS-CoV-2 Mpro has acquired adaptive mutations, leading to the emergence of various drug-resistant strains (*22*). For example, mutations at residues F140, M49, and E166 in SARS-CoV-2 Mpro can significantly reduce the inhibitory activity of competitive inhibitors against SARS-CoV-2. Specifically, the E166V mutation increases the half-maximal inhibitory concentration ($IC_{50}$) of nirmatrelvir and ensitrelvir by 300-fold and 78-fold (*23*), respectively. The occurrence of such drug resistance necessitates the exploration of alternative inhibitory strategies in the field of Mpro inhibitor development. Allosteric inhibitors, which bind to remote allosteric sites on enzymes to induce conformational changes and modulate the function of active sites, offer a promising solution to overcome the aforementioned challenges (*24-26*). Günther *et al.* and Samrat *et al.* have successfully identified a series of allosteric inhibitors of SARS-CoV-2 Mpro (*e.g.*, pelitinib, RS102895, ifenprodil (*27*), and JMX series compounds including JMX0286, JMX0301, and JMX0941 (*28*)) through allosteric modulation strategies targeting non-active sites of Mpro. Among these inhibitors, pelitinib exhibits the most prominent inhibitory activity against SARS-CoV-2 with a half-maximal effective concentration ($EC_{50}$) of 1.25 μM. (*27*). However, as a compound originally developed for antitumor activity, pelitinib can significantly inhibit human membrane-associated tyrosine/threonine protein kinase 1 (Myt1 kinase) and epidermal growth factor receptor (EGFR), leading to severe off-target effects (*29,30*). Additionally, the molecular mechanism underlying the allosteric inhibition of SARS-CoV-2 Mpro remains unclear, which has hindered the further development of its allosteric inhibitors.

In this study, we focused on the allosteric inhibition of SARS-CoV-2 Mpro by pelitinib. By using integrated molecular dynamics (MD) simulations, virtual screening, and bioassay strategies, we systematically investigated the allosteric inhibition mechanism of SARS-CoV-2 Mpro and further identified novel allosteric inhibitors based on this mechanism. Our results demonstrated that pelitinib regulates the conformation of the S3 helix through the L141-S144-C145-H41 interaction network, which induces the contraction of the catalytic pocket and blocks substrate binding, thereby inhibiting Mpro activity. Based on this mechanism, we successfully screened a novel compound (designated as Cpd-1). Biological activity assays showed that Cpd-1 exhibited significantly improved Mpro inhibitory activity ($IC_{50}$ = 74.3 μM) compared with pelitinib ($IC_{50}$ = 148.3 μM). Moreover, Cpd-1 displayed excellent target selectivity and low cytotoxicity. Furthermore, Cpd-1 retained potent inhibitory activity against multiple drug-resistant mutants of SARS-CoV-2 Mpro, demonstrating its potential to overcome drug resistance. Collectively, this study proposes a molecular mechanism for allosteric inhibition of Mpro and identifies a candidate compound with favorable activity, selectivity, and anti-resistance properties, providing a new strategy and theoretical basis for the development of Mpro-targeting inhibitors.

## 2. Materials and Methods

### 2.1. Molecular dynamics simulations

The initial structures of the SARS-CoV-2 Mpro, Myt1 kinase, and EGFR were retrieved from the RCSB Protein Data Bank (*31*) (detailed information is listed in Table S1, *https://www.ddtjournal.com/action/getSupplementalData.php?ID=315*). All receptor-ligand complexes were constructed based on co-crystal structures or through molecular docking. All Molecular Dynamics (MD) Simulations were performed with AMBER24 (*32,33*). The Amber ff19SB force field (*34*) was employed for the protein, and the TIP3P model (*35*) was used for the solvent water molecules. The force field parameters of ligands were generated from the general AMBER force field (GAFF), and the partial atomic charge was defined by the restrained electrostatic potential (RESP) (*36*) charge based on HF/6-31G* calculation with the Gaussian09 package.

The initial coordinates and topology files were generated by the tleap module with neutralization and solvation. The subsequent classical MD simulations were carried out by using the periodic boundary condition with the cubic model. After a series of energy minimization, programmed heating (0 to 310 K, NVT, 100 ps), density equilibrium (310 K, 1.0 atm, NPT, 100 ps), and pre-equilibrium (310 K, 1.0 atm, NPT, 2 ns), a final long-term scale MD simulation (200 or 500 ns as listed in Table S1, *https://www.ddtjournal.com/action/getSupplementalData.php?ID=315*) with a 2 fs time step were performed under the NVT ensemble to generate trajectories. During the MD simulation, the high-frequency stretching vibration of all hydrogen-

containing bonds was constrained by using the SHAKE algorithm (*37*), and a 12 Å cutoff was applied to van der Waals (LJ-12 potential) and electrostatic interactions (PME strategy). Finally, cpptraj was used for trajectories analysis and PyMOL was used for visualization.

Adaptively Biased Molecular Dynamics (ABMD) (*38*) simulations in AMBER24 were employed for the two systems (Mpro-nsp4/5, and Mpro-nsp4/5-Pelitinib) to map out the free energy profiles of natural substrate (nsp4/5) binding in different states. The distance between the sulfur atom in C145 and the carbon atom of the carbonyl group in Gln of nsp4/5 was defined as the collective variable (CV). The Gaussian bias with spatial directionality was used to drive the substrate from an initial position away from the catalytic site (CV = 27.0 Å) toward the active center (CV = 3.0 Å). The hills and widths were set to 0.1 kcal/mol and 0.5 Å, respectively. The Gaussian bias potential was added to the potential energy surface at every 5 ps. The time step of ABMD was set to 2 fs. In total, the ABMD simulation time were set to 100 ns for the two systems.

Pocket volumes of Mpro in various systems along the MD simulations were calculated using POVME3.0 (*39*). C145 was chosen to define the pocket, and the parameter GridSpacing was set to 1.0 Å. Additionally, the MM-PBSA (*40*) method was employed to calculate the binding free energy of the ligand to the receptor. The trajectory from the stable MD simulation stage was used to calculate the pocket volume and binding free energy. More than 2,000 frames were extracted from the stable MD trajectory at regular intervals for the calculations in each system.

### 2.2. Virtual screening

The screening library was constructed using the Drug-like and Lead-like subsets from the ZINC20 database. Subsequently, through molecular fingerprint similarity analysis based on Tanimoto coefficient in SwissSimilarity (*41*) platform, molecules with structural similarity to Pelitinib greater than 80% were retained to ensure that the candidate compounds maintain the known affinity to the target. It should be noted that the Tanimoto coefficient based molecular fingerprint similarity used here reflects similarities in local chemical environments rather than global 2D scaffold identity. Thus, the screened compounds could exhibit distinct scaffold from Pelitinib but retain the key pharmacophore features essential for allosteric inhibition. The three-dimensional (3D) pharmacophore model was constructed by using Molecular Operating Environment (MOE) (*42*) software, based on the Pelitinib-Mpro complex. Particular attention was paid to the amino acid L141, which is crucial to the allosteric inhibition mechanism. The 3D pharmacophore model was then employed to perform virtual screening against the screening library. Ultimately, 228 candidate compounds were identified and utilized for the subsequent docking-based virtual screening.

By selectively retaining the Apo-Mpro dimer (PDB ID: 6XHU) and integrating the Holo-Mpro monomer (pelitinib-bound complex, PDB ID: 7AXM), a pelitinib-bound SARS-CoV-2 Mpro dimer complex was obtained and utilized as the receptor model for molecular docking. The molecular docking was performed by using AutoDock Vina (*43*). The protonation states of titratable residues in receptor and ionizable groups in compounds were determined under conditions of pH 7.0 ± 0.2, mimicking the actual physiological environment. The ligand (pelitinib) in receptor model was used to define the center of the docking grid, with the grid dimensions set to 25 × 25 × 25 $Å^3$. The flexible docking strategy was ultimately executed based on the induced-fit theory, and the binding mode with the optimal docking score, along with the corresponding docking results, was recorded.

The pharmacokinetic properties and druggability (adsorption, distribution, metabolism, excretion, and toxicity, ADMET) of the screened compounds were predicted by using SwissADME (*44*) (*https://www.swissadme.ch/*), ADMETlab3.0 (*45*) (*https://admetlab3.scbdd.com/*), and ProTox-3.0 (*46*) (*https://tox-new.charite.de/*) platform.

The selected hit compound Cpd-1 (ZINC11613113, SMILES: C1=COC(=C1)CN2C(=O)C=C(C2=O)NC3=CC=C(C=C3)S(=O)(=O)N) was purchased from MCE (MedChemExpress, Monmouth Junction, NJ, USA, Cat. # HY-L0096V, Lot # 676256) as part of the Vitas-M Screening Compounds Library.

### 2.3. Enzymatic assays

The inhibitory activity of the identified compounds on Mpro was assessed using the 2019-nCoV Mpro/3CLpro Inhibitor Screening Kit (Beyotime, Shanghai, China, P0312S). The 2019-nCov Mpro/3CLpro enzyme, at a volume of 1 μL, was exposed to Dabcyl-KTSAVLQSGFRKME-Edansin a 96-well plate at 4ºC. Subsequently, negative control (DMSO) and positive control (Ebselen) were added to the plate, along with samples at concentrations ranging from 6.25 μM to 800 μM (6.25 μM, 12.5 μM, 25 μM, 50 μM, 100 μM, 200 μM, 400 μM, 800 μM). Finally, substrate with a volume of 2 μL was added, and the plate was incubated for 10 minutes at 37ºC. The fluorescence of the final system was measured at excitation and emission wavelengths of 340 nm and 490 nm, respectively, using a multifunctional fluorescence microplate reader (Thermo Fisher Scientific, Waltham, MA, USA).

### 2.4. Cytotoxicity measurement

Cell viability and cytotoxicity assays were conducted

in BEAS-2B cells (Beyotime, Shanghai, China; human bronchial epithelial cells) using the Cell Counting Kit-8 (CCK-8, MeilunBio, Dalian, Liaoning, China), following the manufacturer protocol. Initially, cells were seeded at a density of 6 × $10^3$ cells per well in a volume of 100 µL. After incubation overnight at 37°C in a humidified atmosphere with 5% $CO_2$. The cells were treated with protease inhibitors at different concentrations. After 16 hours of treatment, 10 µL of the CCK-8 solution was added to each well of the plate using a repeating pipette, and the plate was incubated for an additional 1 hours. Absorbance was measured at a wavelength of 450 nm using a BioTek Synergy HT microplate reader (BioTek Instruments, Winooski, VT, USA).

2.5. Statistical analysis

All statistical analyses were performed using GraphPad Prism 9.0 (GraphPad Software, San Diego, CA, USA). Data were extracted from the molecular dynamics simulation trajectory and further presented as mean ± standard deviation (SD). Comparisons among multiple groups were conducted using one-way analysis of variance (ANOVA), followed by post hoc multiple comparisons with letter annotations to indicate between-group differences: groups labeled with the same letter are not statistically different, while groups labeled with different letters (*e.g.*, a *vs*. b) differ significantly, with a significance threshold set at $p < 0.0001$.

## 3. Results

3.1. Allosteric inhibitors induce contraction of the Mpro catalytic pocket

To investigate the effects of allosteric inhibitors (*e.g.*, pelitinib) on the structure of Mpro, MD simulations were performed on six systems, including Mpro monomer, Mpro dimer, and ligand-Mpro complexes. The root-mean-square deviation (RMSD) values of all six systems remained stable throughout the 500 ns simulation, confirming the reliability of the results (Figure S1, *https://www.ddtjournal.com/action/getSupplementalData.php?ID=315*). Subsequent calculations of the catalytic pocket volume in each system revealed that, as shown in Figure 1A, the catalytic pocket volume of Mpro was approximately 1,200 Å³ in systems where Mpro activity was not inhibited (dimer and negative control group: PD168568-Mpro complex (*27*)). In contrast, the pocket volume was reduced to approximately 800 Å³ in systems where Mpro activity was inhibited (monomer, Pelitinib-Mpro, RS102895-Mpro, and Ifenprodil-Mpro complexes (*27*)). These results suggest that the volume of the Mpro catalytic pocket is a key indicator of its activity state. As illustrated in Figure 1B, the active state (~1,200 Å³) significantly enhances substrate binding efficiency by expanding the substrate-binding cavity, whereas the inactive state (~800 Å³) impairs substrate binding through shrinking the substrate-binding pocket, ultimately leading to the loss of enzymatic activity.

To further explore the intrinsic mechanism by which pocket volume affects enzymatic activity, ABMD simulations were employed to calculate the free energy changes during the binding of the natural substrate (nsp4/5) to Mpro in both active and inactive states. As shown in Figure 2, in the active state, the substrate could move from the external region into the catalytic site (with a distance of ~5 Å between the

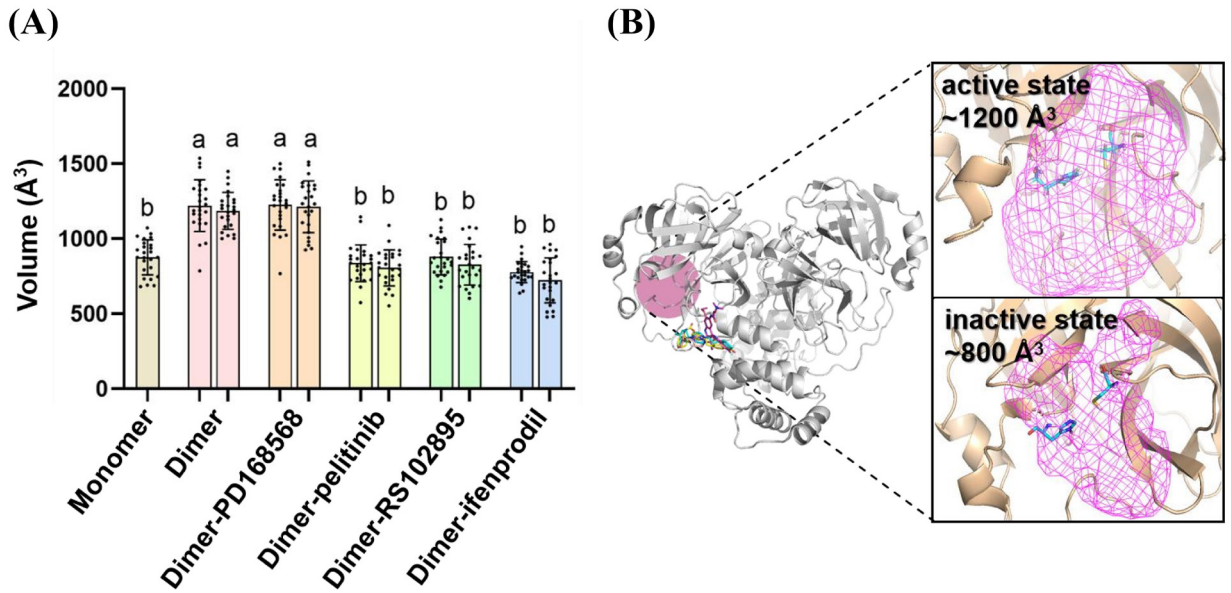


**Figure 1. (A)** Catalytic pocket volume of Mpro in the six systems through MD simulation, groups labeled with different letters differed significantly (a *vs.* b, $p < 0.0001$). **(B)** Relationship model between the Mpro catalytic pocket volume and its catalytic activity. The pocket is depicted by pink mesh.

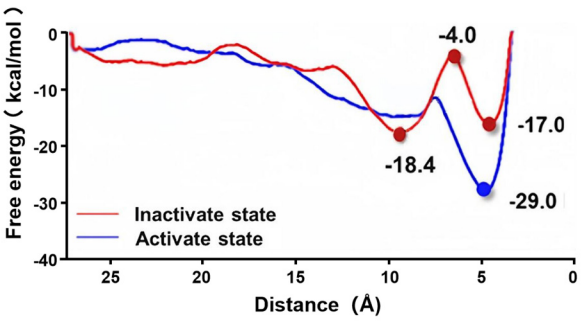


**Figure 2. The free energy profile during the binding of the native substrate to Mpro in active and inactive state.**

substrate and C145) with almost no energy barrier, and finally release 29.0 kcal/mol of energy to form a thermodynamically stable pre-reaction state, ensuring the subsequent occurrence of substrate hydrolysis. In the inactive state, although the substrate could also form a pre-reaction complex by releasing 17.0 kcal/mol of energy, the system first formed a thermodynamically more stable binding intermediate (with a distance of ~10 Å between the substrate and C145) before reaching the pre-reaction state. Thereafter, the system required overcoming an energy barrier of 14.4 kcal/mol to transition into the pre-reaction state. We speculate that due to the small volume of the catalytic pocket, when the substrate approaches the catalytic center to a distance of approximately 10 Å, it needs to induce the expansion of the pocket to achieve further binding. This conformational change results in the final pre-reaction state being thermodynamically and kinetically unstable, leading the substrate to tend to bind in a non-reactive manner (at a distance of ~10 Å from C145) and thus causing enzyme inactivation. These results indicate that an excessively small volume of the Mpro catalytic pocket hinders the effective binding between Mpro and its substrate, thereby rendering the enzyme inactive. Pelitinib appears to achieve inhibition of Mpro activity by inducing pocket contraction upon binding, as suggested by our simulations.

### 3.2. Conformational dynamics of the S3 helix modulate Mpro catalytic activity

Analysis of the MD trajectories of the Mpro structure revealed that the extended helical region spanning residues 40–60, herein defined as the "S3 helix," exhibited significantly higher flexibility in the active state, whereas its flexibility was markedly reduced in the inactive state (Figure 3A and B). This region encompasses the short P2 helix (residues 45–50) described previously (*47*), along with its extended flanking segments identified as key flexible regions in our simulations. The S3 helix is a component of the Mpro catalytic pocket, and H41 on the S3 helix forms a catalytic dyad with C145 located inside the pocket, which is the core of Mpro's hydrolytic function. Local structural analysis (Figure 3C and D) showed that in the active state, the hydrogen bond interaction between the H41-C145 dyad was disrupted, and the S3 helix was no longer constrained, thus moving away from the pocket. This may account for the high flexibility of the S3 helix and the enlarged volume of the Mpro catalytic pocket. In contrast, in the inactive state, the stable hydrogen bond interaction between H41 and C145 restricted the flexibility of the S3 helix and prevented its outward movement, ultimately leading to the shrinkage of the pocket volume. In other words, the interaction between H41 and C145 determines the flexibility of the S3 helix and ultimately affects the size of the Mpro catalytic pocket.

However, the enlarged volume of the Mpro catalytic pocket in the active state is dependent on the dissociation of the catalytic dyad (H41-C145), which contradicts the requirement for Mpro to exert subsequent hydrolytic activity (*i.e.*, a stable hydrogen bond interaction between the H41-C145 catalytic dyad). To resolve this contradiction, ABMD simulations were used to track the changes in the distance between H41 and C145, as well as the catalytic pocket volume, during the binding of the natural substrate (nsp4/5) to Mpro. As shown in Figure 4, with the entry of the substrate (evidenced by the reduced distance between the carbonyl carbon of P1-Gln and the sulfur atom of C145, labeled as d1), the distance between H41 and C145 (d2) decreased synchronously, and the catalytic pocket volume showed a significant contraction trend. When the substrate completed binding to Mpro (with d1 less than 5.0 Å), the pocket volume shrank to less than 1,000 $Å^3$, and d2 was stably maintained within 4 Å. These results indicate that the binding of the natural substrate can induce conformational rearrangement of the catalytic pocket, ultimately forming a stable H41-C145 catalytic dyad structure and a substrate-enzyme pre-reaction state, which is predicted to facilitate the subsequent hydrolysis.

### 3.3.The allosteric inhibition pathway of pelitinib in Mpro

From the protein structure displayed in Figure 5A and B, it is evident that the catalytic site and allosteric site of Mpro are spatially adjacent, and loop 141-145 directly connects these two regions. At the allosteric site, amino acids such as Y118, L141, and C300 exhibit obvious interactions with pelitinib. In this study, a series of Mpro variants were constructed by mutating these amino acids, and the changes in the catalytic pocket volume of each variant in the presence of pelitinib (Mpro-holo state) were calculated. As shown in Figure 5C, only four variants (L141A, S144A, C145A, and H41A) could reverse the pelitinib-induced contraction of the Mpro catalytic pocket volume, indicating that these

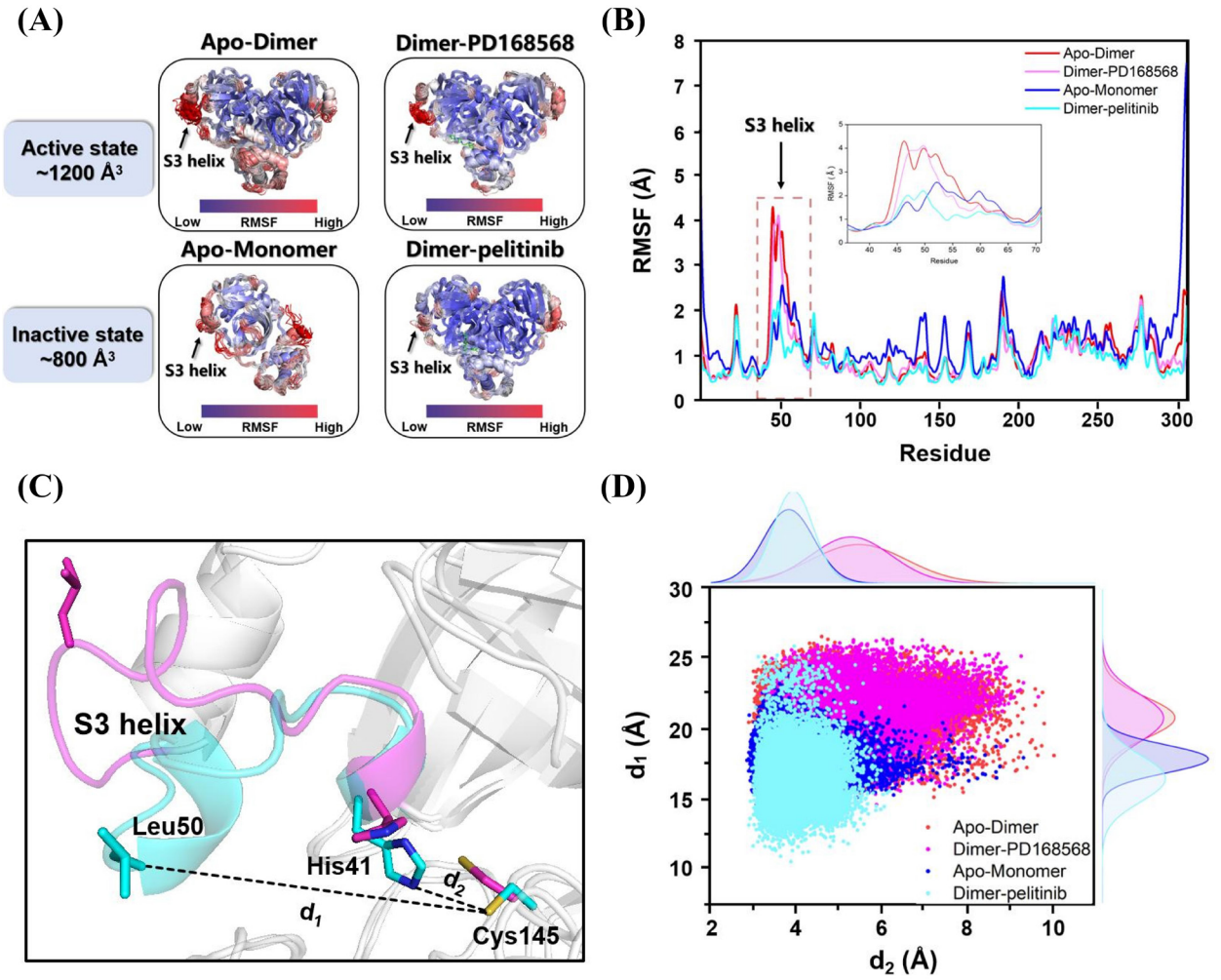


**Figure 3. Conformational dynamics of Mpro in the active and inactive states. (A)** Overall protein flexibility and **(B)** the Root Mean Square Fluctuation (RMSF) profile of Mpro. **(C)** Structural superposition of the S3 helix in the active and inactive states, and **(D)** statistical distribution of some key distances throughout the MD simulation trajectory.

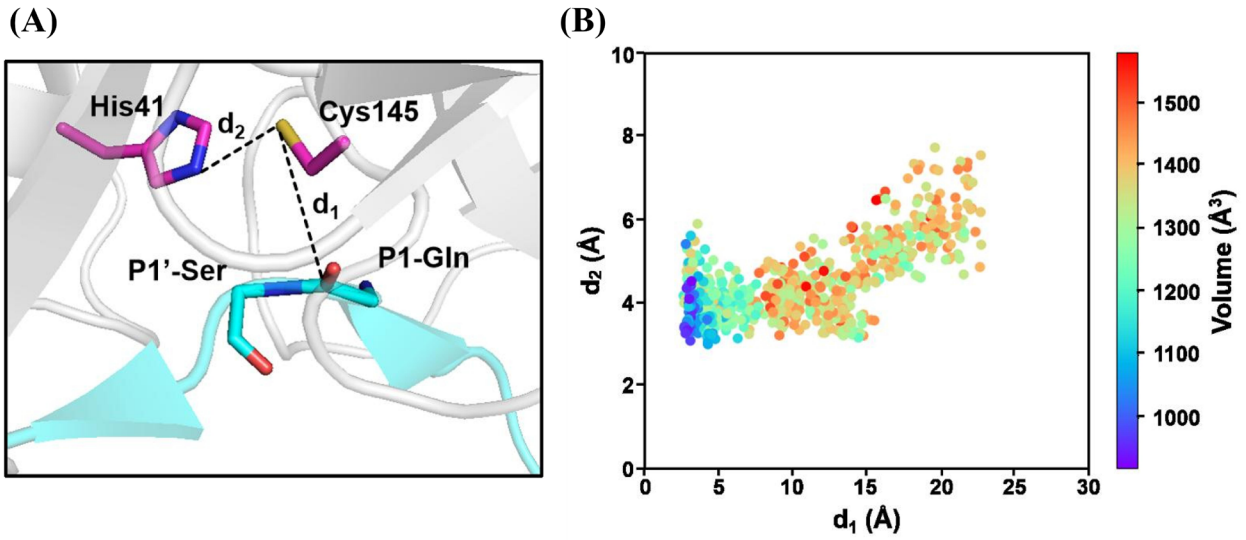


**Figure 4. (A)** Structure of the Mpro-native substrate (nsp4/5) complex. Key catalytic residues H41 and C145 (magenta), and the hydrolysis site in nsp4/5 (cyan), are shown in stick representation. Distances of C145-P1-Gln (d1) and H41-C145 (d2) are indicated by dashed lines. **(B)** Scatter plot of the distributions of d1 and d2. The color bar indicates the volume of Mpro catalytic pocket.

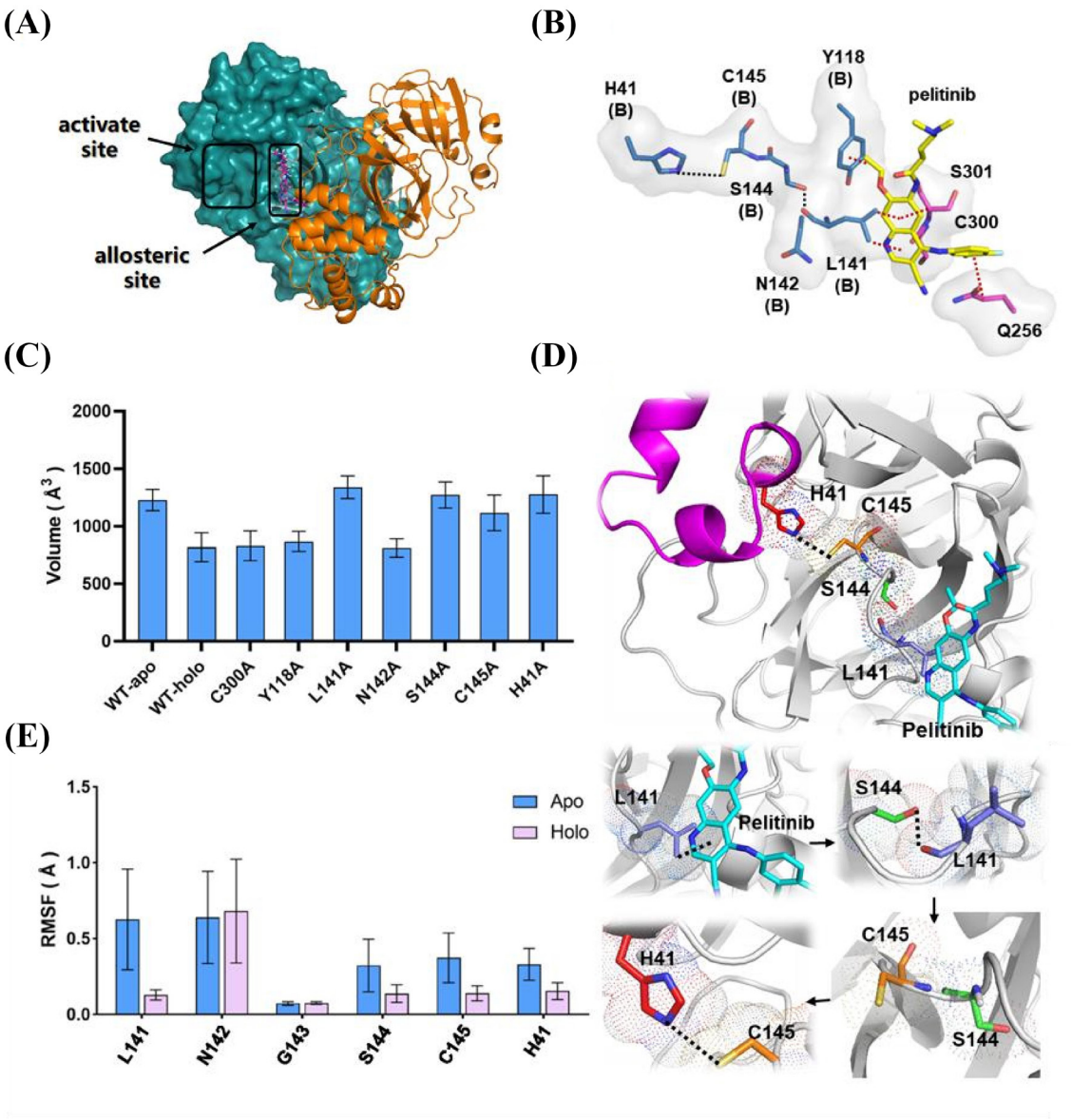


**Figure 5. (A)** Overall structure of the Mpro-Pelitinib complex. **(B)** Close-up view of the residues in active site and the allosteric site. **(C)** Catalytic pocket volumes of the Mpro wild-type and various mutants induced by pelitinib. **(D)** The allosteric regulatory pathway within the pelitinib-Mpro system. Pelitinib and key amino acid residues are shown in stick representation, and the S3 helix is depicted as a purple ribbon. **(E)** RMSF of key residues (L141, S144, C145, H41) along the allosteric pathway in both the Mpro Apo state and the Holo state (Pelitinib-Mpro system).

four amino acids play crucial roles in the allosteric inhibitory effect of Pelitinib. Additionally, the results of the C145A and H41A variants are consistent with our previous finding that the interaction between H41 and C145 affects the volume of the catalytic pocket.

Further analysis of the roles of these four key amino acids in the protein structure (Figure 5D) revealed that there was a CH-π interaction between the aromatic ring of the pelitinib backbone and the side chain of L141. Moreover, a hydrogen bond interaction existed between the main chain of L141 and the side chain of S144. Due to their adjacent positions in the amino acid sequence, the conformational changes of S144 are inevitably transmitted to C145. Based on these observations, we propose the following mechanism: Pelitinib restricts the flexibility of L141 through CH-π interaction, and this flexibility restriction effect is then transmitted to C145 *via* L141-S144. The reduced flexibility of C145 facilitates the maintenance of a stable hydrogen bond interaction between C145 and H41, which prevents the S3 helix from moving outward to expand the pocket. To verify this hypothesis, the root-mean-square fluctuation (RMSF) of loop 141-145 and H41 in both Mpro apo state and holo state (bound to pelitinib) was analyzed. As shown in Figure 5E, compared with the apo state, the flexibility of key amino acids in the pelitinib-mediated allosteric regulatory network (L141, S144, C145, and H41) was significantly reduced in the holo state. In contrast, no significant differences were observed in the flexibility of N142 and G143.

Collectively, these results are consistent with the view that pelitinib restricts the movement of the S3 helix through the L141-S144-C145-H41 interaction network, thereby maintaining the catalytic pocket in a small-volume state and ultimately blocking substrate binding to inhibit protein activity.

### 3.4. Compound screening and activity validation based on the allosteric mechanism

Given the potential off-target toxicity of pelitinib in anti-SARS-CoV-2 applications, this study further aimed to identify novel allosteric inhibitors of Mpro. The detailed screening workflow is shown in Figure S2 (*https://www.ddtjournal.com/action/getSupplementalData.php?ID=315*). By prioritizing the retention of the CH-π interaction with L141, a pharmacophore model based on the binding mode of pelitinib to the Mpro allosteric site was constructed. This model was then used for virtual screening against two subsets (Drug-like subset and Lead-like subset) of the ZINC20 database. Through a series of screening criteria, including molecular similarity evaluation and target affinity assessment, seven candidate compounds with higher affinity for Mpro than pelitinib were finally obtained (Figure S3, *https://www.ddtjournal.com/action/getSupplementalData.php?ID=315*). Subsequently, the pharmacokinetic properties and druggability (ADMET) of these seven compounds were predicted as listed in Table S2 (*https://www.ddtjournal.com/action/getSupplementalData.php?ID=315*). The results showed that Cpd-1 exhibited significant comprehensive advantages. Notably, Cpd-1 had no significant inhibitory effect on the cytochrome P450 enzyme system (CYP450), indicating a low risk of drug-drug interactions (DDI) and favorable metabolic safety profiles, which significantly enhance its potential as an Mpro inhibitor candidate.

Subsequently, a Cpd-1-Mpro complex model was successfully constructed *via* molecular docking. MD simulations combined with catalytic pocket volume analysis were performed to investigate the allosteric inhibitory activity of Cpd-1 against Mpro. The results showed that Cpd-1 could stably bind to the allosteric site of Mpro (Figure 6A and Figure S4, *https://www.ddtjournal.com/action/getSupplementalData.php?ID=315*), and importantly, it could form a stable CH-π interaction with L141, providing a structural basis for allosteric regulation. Further analysis of the

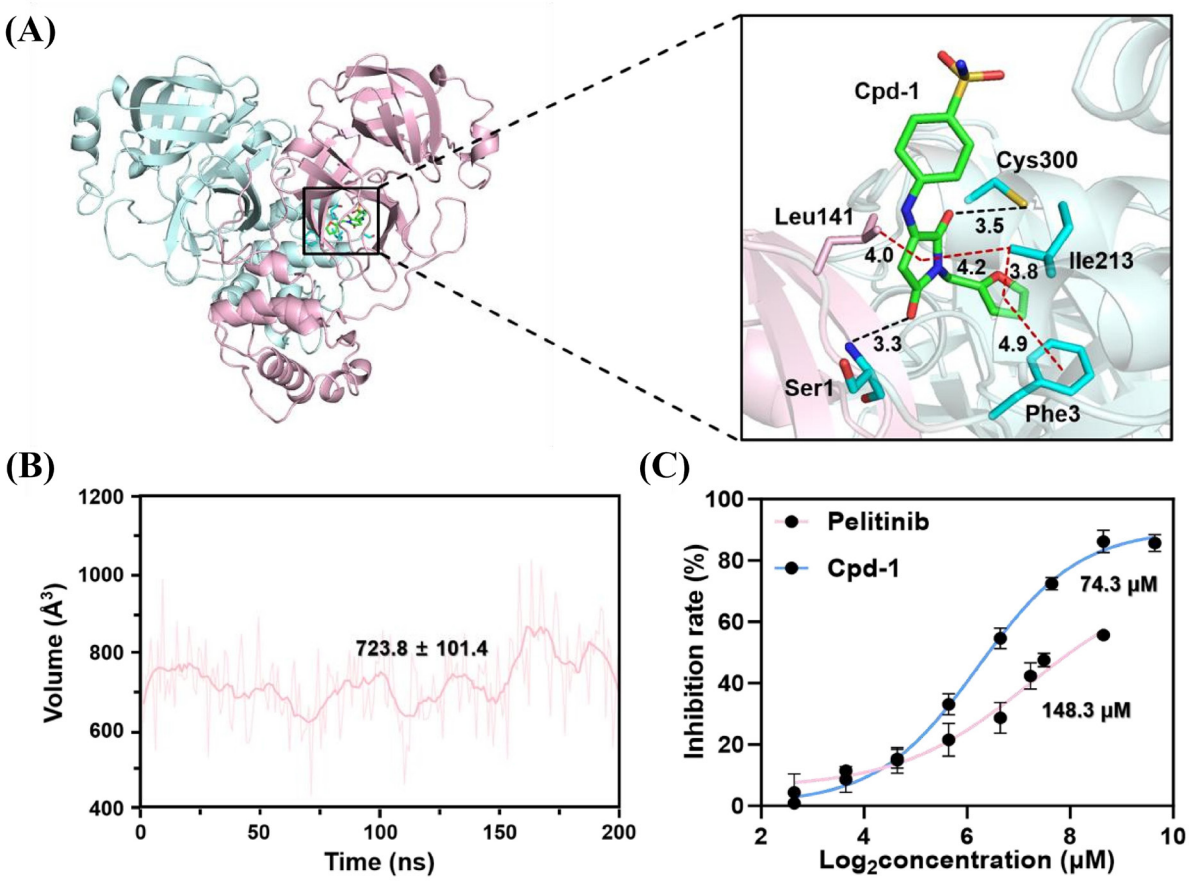


**Figure 6. (A)** The binding mode of Cpd-1 in Mpro. Cpd-1 (green), Leu141 (pink), and other key residues (cyan) are shown in stick representation. Hydrogen bond interactions (black) and CH-π interactions are indicated by dashed lines. Unit of the distance was used in Å. **(B)** Change in the catalytic pocket volume of Mpro in complex with Cpd-1 during the MD simulation. The average volume ± standard deviation is presented. **(C)** Inhibitory rate curve for Cpd-1 and pelitinib (as reference drugs) against SARS-CoV-2 Mpro by FRET assay ($n$ = 3).

catalytic pocket volume of the Cpd-1-Mpro complex revealed that Cpd-1 also induced a reduction in the volume of the Mpro catalytic pocket (723.8 ± 101.4 Å$^3$ in Figure 6B), which was consistent with the behavior of the three previously identified positive compounds (pelitinib, RS102895, and ifenprodil, in Figure 1). This indicates that the newly identified compound (Cpd-1) also has potential allosteric inhibitory activity against SARS-CoV-2 Mpro. Subsequent fluorescence resonance energy transfer (FRET) assays (*48*) (Figure 6C) showed that Cpd-1 exhibited better Mpro inhibitory activity compared with pelitinib (74.3 μM *vs.* 148.3 μM), suggesting the potential of this newly identified compound as an Mpro inhibitor. However, we observed that the direct enzymatic $IC_{50}$ of pelitinib determined in our cell-free FRET assay (148.3 μM) was substantially higher than its previously reported cellular antiviral $EC_{50}$ (1.25 μM) (*27*). We hypothesize that this discrepancy arises because pelitinib is not a selective Mpro inhibitor, but rather a well-documented dual inhibitor of EGFR and Myt1 kinases. Previous studies have demonstrated that EGFR and related host kinase pathways participate in the entry and replication processes of SARS-CoV-2 (*49*). Accordingly, the potent cellular antiviral activity of pelitinib most likely stems from the synergistic effect of allosteric Mpro inhibition combined with the suppression of host kinase pathways essential for viral propagation. In our cell-free enzymatic system, the contribution of host targets is entirely eliminated, thus, the measured $IC_{50}$ solely reflects the direct inhibitory potency of pelitinib against Mpro. Importantly, under strictly identical experimental conditions, Cpd-1 consistently exhibited stronger direct Mpro inhibitory activity than pelitinib, validating the success of our mechanism based screening strategy.

### 3.5. Target selectivity profile of Cpd-1

To investigate the target specificity of Cpd-1, the binding free energies of Cpd-1 and pelitinib to SARS-CoV-2 Mpro, Myt1 kinase, and EGFR were calculated based on MD simulations. Evaluation indicators such as RMSD, radius of gyration (Rg), solvent accessible surface area (SASA) and number of hydrogen bonds (Hbonds) showed that the MD simulations of all constructed ligand-protein systems reached a stable state (Figure S5, *https://www.ddtjournal.com/action/getSupplementalData.php?ID=315*), ensuring the reliability of the subsequent analysis results. As shown in Figure 7, the binding free energy of Cpd-1 to Mpro was -21.2 kcal/mol, which was comparable to that of pelitinib (-20.9 kcal/mol). However, the binding affinity of Cpd-1 to EGFR and Myt1 kinase was significantly weaker than that of pelitinib (-15.0 kcal/mol *vs.* -34.2

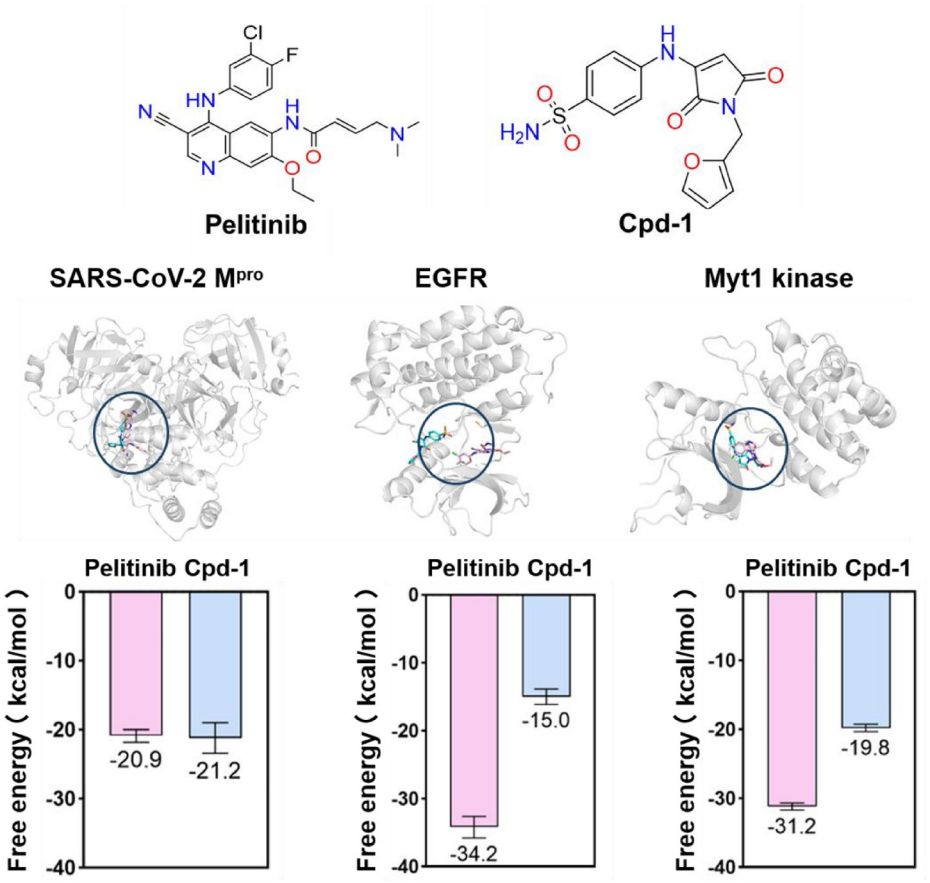


**Figure 7. Structure, binding site, and binding free energy of Cpd-1 and pelitinib toward SARS-CoV-2 M$^{pro}$, EGFR, and Myt1 kinase.**

kcal/mol for EGFR; -19.8 kcal/mol *vs.* -31.2 kcal/mol for Myt1 kinase). Additionally, Cpd-1 exhibited higher affinity for Mpro than for the other two targets. These results suggest that Cpd-1 not only retains Mpro inhibitory activity but also avoids non-specific binding to host EGFR and Myt1 kinase, thereby reducing potential side effects caused by off-target effects.

Subsequently, concentration-gradient experiments were conducted to evaluate the cytotoxicity of Cpd-1 and pelitinib. As shown in Figure 8, although both compounds exhibited concentration-dependent cytotoxic effects, their toxicity profiles differed significantly. Pelitinib induced significant cytotoxicity at a concentration of 10 μM, and almost completely inhibited cell growth at 50 μM. In contrast, Cpd-1 showed almost no cytotoxicity at 50 μM. Notably, even at a high concentration of 200 μM, the cell viability in the Cpd-1-treated group remained at approximately 60%, indicating that Cpd-1 has lower cytotoxicity and higher safety compared with pelitinib.

### 3.6. Computational predictions for selected mutant systems

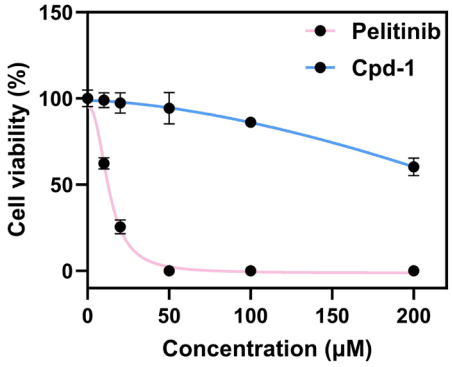


**Figure 8. Cytotoxicity evaluation of Cpd-1 and pelitinib *in vitro* (*n* = 3).**

Based on the findings that Cpd-1 exhibits higher Mpro inhibitory activity and lower cytotoxicity than pelitinib, this study further investigated the predicted inhibitory activity of Cpd-1 against drug-resistant mutants of SARS-CoV-2 Mpro through computational analysis. As shown in Figure 9, the catalytic pocket volume of a series of constructed Mpro drug-resistant mutants was approximately 1200 Å³ in the apo state, consistent with that of the wild-type Mpro. After binding to Cpd-1, the catalytic pocket volume of all mutants, including typical ensitrelvir-resistant strains (M49L and E166A) and nirmatrelvir-resistant strains (F140L, E166V and A193P), was reduced to approximately 800 Å³. These results demonstrate the potential inhibitory activity of Cpd-1 against various drug-resistant mutants of Mpro. These computational predictions suggest a potential strategy to overcome existing drug resistance barriers, warranting further experimental validation.

## 4. Discussion

In this study, we have systematically elucidated the allosteric inhibition mechanism of the SARS-CoV-2 main protease (Mpro) and successfully identified a novel inhibitor, Cpd-1, with the potential to overcome drug resistance. Unlike conventional active-site competitive inhibitors, allosteric modulation offers a distinct strategy to counter the rapid mutational evolution of Mpro. Our extensive MD simulations revealed that pelitinib binds to the allosteric site and, through the L141-S144-C145-H41 interaction network, restricts the flexibility of the S3 helix and stabilizes the H41-C145 catalytic dyad hydrogen bond. This series of conformational changes induces a marked contraction of the catalytic pocket from ~1,200 Å³ to ~800 Å³. This contraction thermodynamically and kinetically impedes the effective binding and hydrolysis of the natural substrate nsp4/5, providing, for the first time, an atomic-level depiction of how an allosteric inhibitor remotely modulates Mpro activity.

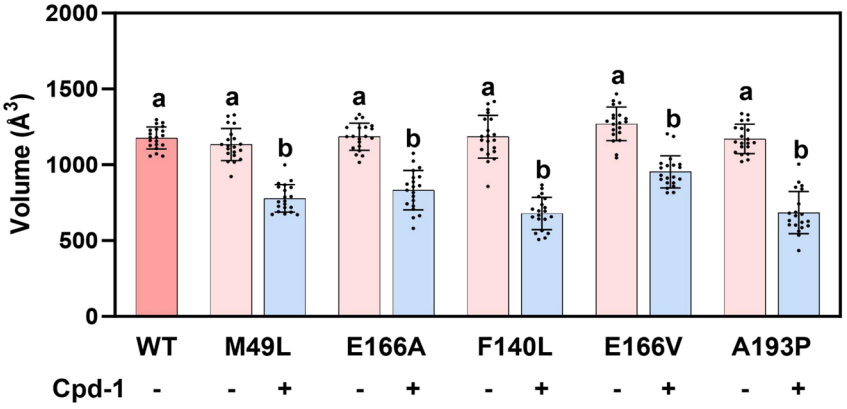


**Figure 9. Catalytic pocket volumes of the SARS-CoV-2 Mpro wild-type, drug-resistant mutants, and the Cpd-1-bound drug-resistant mutants (a *vs.* b, $p < 0.0001$).**

Guided by this mechanism, our structure-based virtual screening and subsequent biological validation led to the discovery of Cpd-1. This compound not only retains the critical CH-π interaction with L141 but also exhibits superior Mpro inhibitory activity ($IC_{50}$ = 74.3 μM) compared to pelitinib ($IC_{50}$ = 148.3 μM) in FRET-based enzymatic assays. More importantly, Cpd-1 demonstrates a significantly improved selectivity profile: computational binding free energy calculations show that its affinity for Mpro (-21.2 kcal/mol) is substantially higher than for the off-targets EGFR (-15.0 kcal/mol) and Myt1 kinase (-19.8 kcal/mol), whereas pelitinib shows strong nonspecific binding to both. These *in silico* findings are strongly corroborated by cytotoxicity assays, where Cpd-1 maintained ~ 60% cell viability even at a high concentration of 200 μM, while pelitinib nearly abolished cell growth at 50 μM. Collectively, these data robustly support a superior therapeutic window and safety profile for Cpd-1.

Notably, our computational predictions further indicate that Cpd-1 can effectively induce the same pocket contraction (from ~1,200 Å³ to ~800 Å³) in a panel of clinically relevant drug-resistant Mpro mutants, including E166V, F140L, and M49L. This suggests its potential for broad-spectrum anti-resistance activity. This characteristic is particularly significant for addressing future viral variants, as allosteric sites often exhibit higher sequence conservation than active sites, and the key residues we target, such as L141, are involved in a non-covalent conformational regulatory network that may be under lower mutational pressure.

Despite these promising findings, certain limitations should be acknowledged. The *in vitro* antiviral efficacy ($EC_{50}$) of Cpd-1, along with its *in vivo* pharmacokinetics and pharmacodynamics in animal models, remain to be validated. Furthermore, its inhibitory activity against resistant mutants is primarily based on computational models and requires confirmation through enzymatic and viral replication assays. Future efforts will focus on structure-based optimization of Cpd-1 to enhance its potency and drug-like properties, followed by comprehensive preclinical evaluation. Overall, our work not only deepens the mechanistic understanding of Mpro allosteric regulation but also provides a robust theoretical foundation and a promising candidate for the development of next-generation anti-coronavirus agents with a higher barrier to resistance.

## 5. Supporting Information

Summary of the MD simulation systems (Table S1, *https://www.ddtjournal.com/action/getSupplementalData.php?ID=315*), predicted pharmacokinetic properties and druggability (ADMET) of the screened compounds (Table S2, *https://www.ddtjournal.com/action/getSupplementalData.php?ID=315*). RMSD of Mpro monomer, Mpro dimer, and four ligand-Mpro complexes during the 500 ns MD simulation (Figure S1, *https://www.ddtjournal.com/action/getSupplementalData.php?ID=315*), screening workflow on the allosteric inhibitors of Mpro (Figure S2, *https://www.ddtjournal.com/action/getSupplementalData.php?ID=315*), structures and binding affinities of Pelitinib and the seven candidate compounds on Mpro (Figure S3, *https://www.ddtjournal.com/action/getSupplementalData.php?ID=315*), RMSD of Cpd-1-Mpro complex and distance changes of the key residues with Cpd-1 during the 200 ns MD simulation (Figure S4, *https://www.ddtjournal.com/action/getSupplementalData.php?ID=315*), evaluation indicators of MD simulation (RMSD, Rg, SASA and Hbonds) on the ligand-receptor complexes in Section 3.5 (Figure S5, *https://www.ddtjournal.com/action/getSupplementalData.php?ID=315*).

*Funding*: This work was supported by Natural Science Foundation of Shandong Province (ZR2024QH448), Key R&D Program of Shandong Province (2025CXPT137).

*Conflict of Interest*: The authors have no conflicts of interest to disclose.

*Data availability statement*: All data (input files for the MD simulations) are available on Github (*https://github.com/xwtangQDU/Allosteric-Inhibition-Mechanism-of-SARS-CoV-2-Main-Protease*).

## References

1. Piret J, Boivin G. Pandemics throughout history. Front Microbiol. 2021; 11:631736.
2. Fauci AS. Infectious diseases: considerations for the 21st century. Clin Infect Dis. 2001; 32:675-685.
3. Nicola M, Alsafi Z, Sohrabi C, Kerwan A, Al-Jabir A, Iosifidis C, Agha M, Agha R. The socio-economic implications of the coronavirus pandemic (COVID-19): a review. Int J Surg. 2020; 78:185-193.
4. Karniadakis I, Mazonakis N, Tsioutis C, Papadakis M, Markaki I, Spernovasilis N. Oral Molnupiravir and Nirmatrelvir/Ritonavir for the treatment of COVID-19: a literature review with a focus on real-world evidence. Infect Dis Rep. 2023; 15:662-678.
5. Cao B, Wang Y, Lu H, *et al.* Oral simnotrelvir for adult patients with mild-to-moderate COVID-19. N Engl J Med. 2024; 390:230-241.
6. Chen X, Huang X, Ma Q, *et al*. Preclinical evaluation of the SARS-CoV-2 Mpro inhibitor RAY1216 shows improved pharmacokinetics compared with nirmatrelvir. Nat Microbiol. 2024; 9:1075-1088.
7. Syed YY. Ensitrelvir fumaric acid: first approval. Drugs. 2024; 84:721-728.
8. Kow CS, Hasan SS. Real-world effectiveness of BNT162b2 mRNA vaccine: a meta-analysis of large observational studies. Inflammopharmacology. 2021; 29:1075-1090.
9. Khobragade A, Bhate S, Ramaiah V, *et al.* Efficacy,

safety, and immunogenicity of the DNA SARS-CoV-2 vaccine (ZyCoV-D): the interim efficacy results of a phase 3, randomised, double-blind, placebo-controlled study in India. Lancet. 2022; 399:1313-1321.
10. Hadj Hassine I. COVID-19 vaccines and variants of concern: a review. Rev Med Virol. 2022; 32:e2313.
11. Graña C, Ghosn L, Evrenoglou T, *et al.* Efficacy and safety of COVID-19 vaccines. Cochrane Database Syst Rev. 2022; 12:CD015477.
12. McLean G, Kamil J, Lee B, Moore P, Schulz TF, Muik A, Sahin U, Türeci Ö, Pather S. The impact of evolving SARS-CoV-2 mutations and variants on COVID-19 vaccines. mBio. 2022; 13:e02979-21.
13. Madhi SA, Baillie V, Cutland CL, *et al.* Efficacy of the ChAdOx1 nCoV-19 Covid-19 vaccine against the B.1.351 variant. N Engl J Med. 2021; 384:1885-1898.
14. Hu Q, Xiong Y, Zhu G, Zhang Y, Zhang Y, Huang P, Ge G. The SARS-CoV-2 main protease (Mpro): structure, function, and emerging therapies for COVID-19. MedComm. 2022; 3:e151.
15. Bhardwaj M, Anjum R, Hariprasad P, Patel AK. Allosteric mutations impact the catalytic activity and oligomeric state of the main protease of coronavirus. Int J Biol Macromol. 2025; 309:142765.
16. Gioia M, Ciaccio C, Calligari P, De Simone G, Sbardella D, Tundo G, Fasciglione GF, Di Masi A, Di Pierro D, Bocedi A, Ascenzi P, Coletta M. Role of proteolytic enzymes in the COVID-19 infection and promising therapeutic approaches. Biochem Pharmacol. 2020; 182:114225.
17. Zhang L, Lin D, Sun X, Curth U, Drosten C, Sauerhering L, Becker S, Rox K, Hilgenfeld R. Crystal structure of SARS-CoV-2 main protease provides a basis for design of improved α-ketoamide inhibitors. Science. 2020; 368:409-412.
18. Liu Y, Liang C, Xin L, Ren X, Tian L, Ju X, Li H, Wang Y, Zhao Q, Liu H, Cao W, Xie X, Zhang D, Wang Y, Jian Y. The development of coronavirus 3C-like protease (3CLpro) inhibitors from 2010 to 2020. Eur J Med Chem. 2020; 206:112711.
19. Jin Z, Du X, Xu Y, *et al.* Structure of Mpro from SARS-CoV-2 and discovery of its inhibitors. Nature. 2020; 582:289-293.
20. Cannalire R, Cerchia C, Beccari AR, Di Leva FS, Summa V. Targeting SARS-CoV-2 proteases and polymerase for COVID-19 treatment: state of the art and future opportunities. J Med Chem. 2022; 65:2716-2746.
21. Lu H, Zhang G, Mao J, *et al*. Efficacy and safety of GST-HG171 in adult patients with mild to moderate COVID-19: a randomised, double-blind, placebo-controlled phase 2/3 trial. eClinicalMedicine. 2024; 71:102582.
22. Hattori SI, Bulut H, Hayashi H, *et al*. Structural and virologic mechanism of the emergence of resistance to Mpro inhibitors in SARS-CoV-2. Proc Natl Acad Sci U S A. 2024; 121:e2404175121.
23. Moghadasi SA, Biswas RG, Harki DA, Harris RS. Rapid resistance profiling of SARS-CoV-2 protease inhibitors. NPJ Antimicrob Resist. 2023; 1:9.
24. Wenthur CJ, Gentry PR, Mathews TP, Lindsley CW. Drugs for allosteric sites on receptors. Annu Rev Pharmacol. 2014; 54:165-184.
25. Cimermancic P, Weinkam P, Rettenmaier TJ, Bichmann L, Keedy DA, Woldeyes RA, Schneidman-Duhovny D, Demerdash ON, Mitchell JC, Wells JA, Fraser JS, Sali A. CryptoSite: expanding the druggable proteome by characterization and prediction of cryptic binding sites. J Mol Biol. 2016; 428:709-719.
26. Greener JG, Sternberg MJ. Structure-based prediction of protein allostery. Curr Opin Struct Biol. 2018; 50:1-8.
27. Günther S, Reinke PYA, Fernández-García Y, *et al.* X-ray screening identifies active site and allosteric inhibitors of SARS-CoV-2 main protease. Science. 2021; 372:642-646.
28. Samrat SK, Xu J, Xie X, Gianti E, Chen H, Zou J, Pattis JG, Elokely K, Lee H, Li Z, Klein ML, Shi PY, Zhou J, Li H. Allosteric inhibitors of the main protease of SARS-CoV-2. Antiviral Res. 2022; 205:105381.
29. Zhu JY, Cuellar RA, Berndt N, Lee HE, Olesen SH, Martin MP, Jensen JT, Georg GI, Schönbrunn E. Structural basis of Wee kinases functionality and inactivation by diverse small molecule inhibitors. J Med Chem. 2017; 60:7863-7875.
30. Hegedüs C, Truta-Feles K, Antalffy G, Várady G, Német K, Ozvegy-Laczka C, Kéri G, Orfi L, Szakács G, Settleman J, Váradi A, Sarkadi B. Interaction of the EGFR inhibitors gefitinib, vandetanib, pelitinib and neratinib with the ABCG2 multidrug transporter: implications for the emergence and reversal of cancer drug resistance. Biochem Pharmacol. 2012; 84:260-267.
31. Berman HM, Westbrook J, Feng Z, Gilliland G, Bhat TN, Weissig H, Shindyalov IN, Bourne PE. The Protein Data Bank. Nucleic Acids Res. 2000; 28:235-242.
32. Hollingsworth SA, Dror RO. Molecular dynamics simulation for all. Neuron. 2018; 99:1129-1143.
33. Case DA, Aktulga HM, Belfon K, *et al.* AmberTools. J Chem Inf Model. 2023; 63:6183-6191.
34. Tian C, Kasavajhala K, Belfon KAA, Raguette L, Huang H, Migues AN, Bickel J, Wang Y, Pincay J, Wu Q, Simmerling C. ff19SB: amino-acid-specific protein backbone parameters trained against quantum mechanics energy surfaces in solution. J Chem Theory Comput. 2020; 16:528-552.
35. Jorgensen WL, Chandrasekhar J, Madura JD, Impey RW, Klein ML. Comparison of simple potential functions for simulating liquid water. J Chem Phys. 1983; 79:926-935.
36. Bayly CI, Cieplak P, Cornell W, Kollman PA. A well-behaved electrostatic potential based method using charge restraints for deriving atomic charges: the RESP model. J Phys Chem. 1993; 97:10269-10280.
37. Ryckaert JP, Ciccotti G, Berendsen HJC. Numerical integration of the Cartesian equations of motion of a system with constraints: molecular dynamics of n-alkanes. J Comput Phys. 1977; 23:327-341.
38. Babin V, Roland C, Sagui C. Adaptively biased molecular dynamics for free energy calculations. J Chem Phys. 2008; 128:134101.
39. Wagner JR, Sørensen J, Hensley N, Wong C, Zhu C, Perison T, Amaro RE. POVME 3.0: software for mapping binding pocket flexibility. J Chem Theory Comput. 2017; 13:4584-4592.
40. Kumari R, Kumar R, Lynn A. G_mmpbsa – a GROMACS tool for high-throughput MM-PBSA calculations. J Chem Inf Model. 2014; 54:1951-1962.
41. Zoete V, Daina A, Bovigny C, Michielin O. SwissSimilarity: a web tool for low to ultra high throughput ligand-based virtual screening. J Chem Inf Model. 2016; 56:1399-1404.
42. Vilar S, Cozza G, Moro S. Medicinal chemistry and the Molecular Operating Environment (MOE): application

of QSAR and molecular docking to drug discovery. Curr Top Med Chem. 2008; 8:1555-1572.
43. Trott O, Olson AJ. AutoDock Vina: improving the speed and accuracy of docking with a new scoring function, efficient optimization, and multithreading. J Comput Chem. 2010; 31:455-461.
44. Daina A, Michielin O, Zoete V. SwissADME: a free web tool to evaluate pharmacokinetics, drug-likeness and medicinal chemistry friendliness of small molecules. Sci Rep. 2017; 7:42717.
45. Fu L, Shi S, Yi J, Wang N, He Y, Wu Z, Peng J, Deng Y, Wang W, Wu C, Lyu A, Zeng X, Zhao W, Hou T, Cao D. ADMETlab 3.0: an updated comprehensive online ADMET prediction platform enhanced with broader coverage, improved performance, API functionality and decision support. Nucleic Acids Res. 2024; 52:W422-W431.
46. Banerjee P, Kemmler E, Dunkel M, Preissner R. ProTox 3.0: a webserver for the prediction of toxicity of chemicals. Nucleic Acids Res. 2024; 52:W513-W520.
47. Kneller DW, Phillips G, O'Neill HM, Jedrzejczak R, Stols L, Langan P, Joachimiak A, Coates L, Kovalevsky A. Structural plasticity of SARS-CoV-2 3CL Mpro active site cavity revealed by room temperature X-ray crystallography. Nat Commun. 2020; 11:3202.
48. Zhao J, Ma Q, Zhang B, Guo P, Wang Z, Liu Y, Meng M, Liu A, Yang Z, Du G. Exploration of SARS-CoV-2 3CLpro inhibitors by virtual screening methods, FRET detection, and CPE assay. J Chem Inf Model. 2021; 61:5763-5773.
49. Razzaq A, Disoma C, Zhou Y, *et al*. Targeting epidermal growth factor receptor signalling pathway: a promising therapeutic option for COVID-19. Rev Med Virol. 2024; 34:e2500.

Received July 28, 2026; Revised August 18, 2026; Accepted August 22, 2026.

**Address correspondence to:*
Xiaowen Tang, School of Pharmacy, and Shandong Provincial Key Laboratory of Pathogenesis and Prevention of Brain Diseases, Qingdao University, Qingdao 266071, China.
E-mail: xwtang1219@qdu.edu.cn

Released online in J-STAGE as advance publication August 26, 2026.

***Brief Report***

DOI: 10.5582/ddt.2026.01033

# Simultaneous determination of belzutifan and cabozantinib, oral agents for renal cell carcinoma, in human plasma using high-performance liquid chromatography

**Yoshito Gando, Takeo Yasu***

Department of Clinical Pharmacodynamics and Toxicology Analytics, Meiji Pharmaceutical University, Tokyo, Japan.

**SUMMARY**: Belzutifan and cabozantinib are oral drugs for advanced renal cell carcinoma, which display exposure-dependent toxicities. No validated method exists for simultaneously quantifying these drugs in human plasma. In this study, we developed and validated a high-performance liquid chromatography–ultraviolet method for simultaneously quantifying belzutifan and cabozantinib in human plasma. Plasma samples (50 μL) were processed *via* simple protein precipitation. Chromatographic separation on a C18 column was performed isocratically with 0.5% $KH_2PO_4$ (pH 4.5)/acetonitrile (47/53, v/v) at 1.0 mL/min, with UV detection at 230 nm. Performance characteristics (calibration, precision, accuracy, recovery, stability, selectivity, and interference by concomitant drugs) were systematically evaluated. Linear calibration ranges were 50–4,000 ng/mL for belzutifan and 25–4,000 ng/mL for cabozantinib with excellent linearity ($r^2 \geq 0.9998$). Intra- and interday coefficients of variation were ≤ 5.41% for belzutifan and ≤ 12.25% for cabozantinib. Both analytes were stable under bench-top, short-term, long-term, and freeze–thaw conditions. No interference from endogenous plasma components or six commonly co-administered medications was observed. The newly developed assay for the simultaneous quantification of belzutifan and cabozantinib in human plasma is rapid, requires minimal sample volumes, and demonstrates robust analytical performance.

***Keywords***: high-performance liquid chromatography–ultraviolet, human plasma concentration, belzutifan; cabozantinib

## 1. Introduction

Belzutifan and cabozantinib are orally administered anticancer agents indicated for the treatment of advanced renal cell carcinoma (RCC) (*1,2*). Belzutifan is predominantly metabolized by UDP-glucuronosyltransferase (UGT) 2B17 and cytochrome P450 (CYP) 2C19 (*3*). Poor-metabolizer (PM) phenotypes associated with UGT2B17 and CYP2C19 occur at appreciable frequencies in Asian populations, with reported prevalences of approximately 60% and 20%, respectively, among Japanese individuals (*4,5*). Although the predicted prevalence of the dual UGT2B17/CYP2C19 PM phenotype in the United States population is approximately 0.5%, it may be as high as 15% in East Asian populations (*3*). Anemia is a characteristic adverse event associated with belzutifan, with incidences of 82.8% for any grade and 32.5% for grade ≥ 3 (*1*). Exposure–response analyses have demonstrated a significant association between plasma belzutifan concentrations and the incidence of grade ≥ 3 anemia (*6*). In individuals with the dual UGT2B17/CYP2C19 PM phenotype, the area under the concentration–time curve (AUC) of belzutifan is reportedly 3.2-fold higher than those for UGT2B17 extensive metabolizers and CYP2C19 non-PMs, translating into an estimated 13.0% increase in the risk of grade ≥ 3 anemia (*3,6*). Collectively, these observations suggest that monitoring plasma belzutifan concentrations and implementing appropriate dose adjustments may mitigate the risk of severe anemia while preserving therapeutic efficacy.

For cabozantinib, plasma exposure is associated with its efficacy and toxicity, with thresholds of 536.8 and 617.7 ng/mL, respectively (*7*). Moreover, plasma cabozantinib concentrations in Japanese patients have been reported to be approximately 30% higher than those in non-Japanese patients (*8*). In light of these findings, therapeutic drug monitoring (TDM)–guided dose optimization has been recommended for cabozantinib (*9*).

Recently, the efficacy of the combination of belzutifan and cabozantinib was evaluated in a clinical trial, and this combination therapy might become one

of the treatment options for renal cell carcinoma in the future (*10*). Although several analytical methods have been described for the individual quantification of belzutifan or cabozantinib in human plasma (*11-13*), no validated method is available for simultaneous quantification of both the agents. To address this gap, we developed and validated a high-performance liquid chromatography–ultraviolet (HPLC–UV) method for simultaneous measurement of belzutifan and cabozantinib in human plasma in accordance with the U.S. Food and Drug Administration Bioanalytical Method Validation Guidance (*14*).

## 2. Materials and Methods

### 2.1. Reagents and chemicals

Belzutifan was obtained from MedChemExpress (Monmouth Junction, NJ, USA). Cabozantinib and ibrutinib (internal standard, IS) were obtained from Toronto Research Chemicals Inc. (Ontario, Canada) (Figure 1). HPLC-grade acetonitrile, methanol, distilled water (Kanto Chemical Co., Inc., Tokyo, Japan), dimethyl sulfoxide (Fujifilm Wako, Osaka, Japan), and $KH_2PO_4$ (FUJIFILM Wako Pure Chemical Co., Osaka, Japan) were used to prepare the HPLC mobile phase and stock/working solutions. Human plasma (pooled and individual) and ethylenediaminetetraacetic acid (EDTA)-2Na were purchased from Cosmo Bio Co., Ltd. (Tokyo, Japan).

### 2.2. Stock and working standard solutions

Stock solutions containing 1 mg/mL belzutifan and cabozantinib were prepared in acetonitrile. Stock solutions of IS were prepared in methanol at 1 mg/mL. Working solutions of belzutifan (250, 500, 2,500, 5,000, 10,000, and 20,000 ng/mL) and cabozantinib (125, 250, 2,500, 5,000, 10,000, and 20,000 ng/mL) were prepared by dilution with acetonitrile. The IS was further diluted with methanol to a final concentration of 2,500 ng/mL. All working solutions were stored at − 60°C.

### 2.3. Equipment and chromatographic conditions

All analyses were performed on an HPLC system (Jasco, Tokyo, Japan) equipped with PU-4180 pumps, a UV-4075 detector, and an AS-4550 autosampler. Chromatographic separation was achieved using a Capcell Pak C18 MG II reversed-phase column (250 × 4.6 mm i.d., 5 μm; Osaka Soda, Tokyo, Japan). The mobile phase consisted of 0.5% potassium dihydrogen phosphate ($KH_2PO_4$, pH 4.5) and acetonitrile (47/53, v/v), delivered at a flow rate of 1.0 mL/min, and analytes were detected at 230 nm. The column and autosampler temperatures were maintained at room temperature (22°C). The run time was 10.5 min.

### 2.4. Internal standard (IS) selection

Ibrutinib, a Bruton's tyrosine kinase inhibitor (TKI) that is primarily used for the treatment of chronic lymphocytic leukemia, was selected as the IS, as it is unlikely to be co-administered in patients with RCC (*15*). In analytical methods for cabozantinib, TKIs are frequently used as ISs (*12,13*). Accordingly, we evaluated five TKIs (brigatinib, tirabrutinib, pirtobrutinib, erlotinib, and nilotinib) as potential IS candidates. However, their retention times (2.4, 5.4, 5.8, 6.0, and 8.9 min, respectively) overlapped with those of plasma matrix components or the analytes of interest, rendering them unsuitable for use as ISs. Ibrutinib provided appropriate chromatographic separation without interference.

### 2.5. Preparation of samples

Prior to analyses, human plasma and working solutions were thawed and vortexed. Briefly, blank plasma (50 μL) was spiked with 10 μL of belzutifan and 10 μL of cabozantinib and mixed by vortexing for 5 s, followed by the addition of 10 μL of IS and 120 μL of methanol chilled to − 60°C (total volume 200 μL). The mixture was vortexed for 1 min and centrifuged at 15,000 × *g* for 10 min at 4°C. Thereafter, 30 μL of the resulting supernatant was directly injected into the HPLC system for analysis.

### 2.6. Calibration curves and quantitation

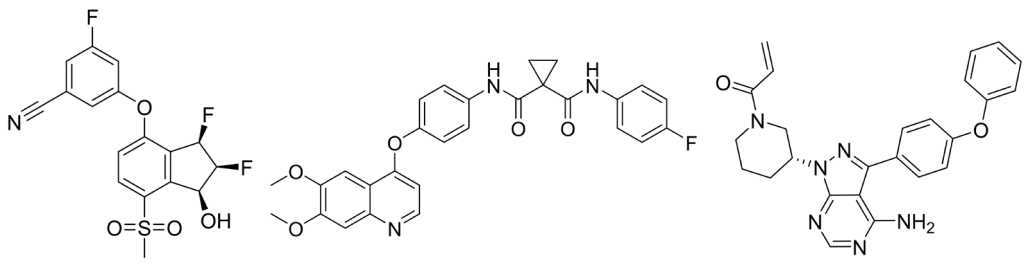


Belzutifan Cabozantinib Ibrutinib

**Figure 1. Chemical structures of belzutifan (left), cabozantinib (center), and ibrutinib (right).**

Accuracy and linearity were assessed by analyzing a series of calibration standards for belzutifan (50, 100, 500, 1,000, 2,000, and 4,000 ng/mL) and cabozantinib (25, 50, 500, 1,000, 2,000, and 4,000 ng/mL). Intra- and inter-day precision and accuracy were evaluated by replicate analyses of five sets of plasma samples spiked with six concentrations of belzutifan and cabozantinib within the same day or over five consecutive days. Analytical validation procedures were performed in accordance with the recommendations of the FDA Guidance for the Validation of Bioanalytical Methods (*14*).

2.7. Stability studies

Stability was evaluated at 50, 1,000, and 4,000 ng/mL for belzutifan and at 25, 1,000, and 4,000 ng/mL for cabozantinib. To evaluate bench-top, short-term, long-term, and freeze–thaw stability, samples were maintained at room temperature (22°C) for 6 h, stored at 4°C for 24 h, stored at −60°C for 3 months, and subjected to three cycles of freezing at −60°C or below and thawing at room temperature, respectively. Stability was evaluated by analyzing these samples against calibration curves prepared from freshly spiked analytes, and the measured concentrations were compared with the nominal values.

2.8. Recovery

The recovery of belzutifan and cabozantinib was evaluated in five replicates of plasma samples spiked with six concentrations of each analyte and 50 µL of normal saline to determine the recovery ratio (%). The average recovery of each analyte (expressed as a percentage) was calculated by dividing the recovered amount by the original amount and multiplying by 100.

2.9. Selectivity and specificity

Selectivity was evaluated using seven different commercially available lots of blank human plasma without the addition of belzutifan, cabozantinib, or IS. In a previous study, we investigated the top 10 medications most frequently co-administered with cabozantinib in clinical practice in Japan, namely levothyroxine, amlodipine, ursodeoxycholic acid, acetaminophen, magnesium oxide, vonoprazan, esomeprazole, furosemide, febuxostat, and nifedipine (*13*). Six frequently co-administered medications (Table 1) were evaluated under identical analytical conditions to assess potential interference, defined as the presence of peaks co-eluting with belzutifan, cabozantinib, or the IS at a resolution of < 1.5.

2.10. Ethical considerations

This study used commercially available pooled and individual human plasma samples (Cosmo Bio Co., Ltd., Tokyo, Japan; catalog No. 12271450 and 12271440), which was supplied without donor identifiers or individual-level clinical information and was used solely as an *in vitro* assay matrix. In accordance with the Ethical Guidelines for Medical and Biological Research Involving Human Subjects in Japan and the institutional policy of Meiji Pharmaceutical University, this study was considered outside the scope of ethics committee review because it used only a generally available commercial research reagent.

## 3. Results and Discussion

3.1. Chromatography, selectivity, and specificity

Representative chromatograms of blank human plasma samples are shown in Figure 2a. The retention times of belzutifan, cabozantinib, and the IS were 6.1, 9.5, and 8.3 min, respectively. The chromatographic resolutions of belzutifan and cabozantinib from the IS were 9.4 and 4.0, respectively. No interference from endogenous plasma components was observed at these retention times (Figures 2b and 2c).

The selectivity and specificity of the method were further evaluated using plasma matrices obtained from seven different commercially available lots. No endogenous interference with belzutifan, cabozantinib, or the IS was detected. In addition, six concomitant medications frequently co-administered in oncology practice were evaluated under the same chromatographic conditions, and none interfered with the retention times of belzutifan, cabozantinib, or the IS (Table 1). These

**Table 1. Medications included in the specificity evaluation**

| Medications | Retention time (min) | Rs *vs*. belzutifan peak | Rs *vs*. cabozantinib peak | Rs *vs*. IS peak |
|---|---|---|---|---|
| Acetaminophen | 3.6 | 8.7 | 13.7 | 12.2 |
| Amlodipine | 3.8 | 11.0 | 17.2 | 15.4 |
| Esomeprazole | 4.6 | 11.1 | 18.7 | 16.7 |
| Febuxostat | 6.4 | 2.8 | 10.5 | 8.2 |
| Furosemide | 4.1 | 11.5 | 18.1 | 16.4 |
| Levothyroxine | 3.8 | 12.2 | 18.6 | 16.7 |

Medications that are used concomitantly with belzutifan or cabozantinib in clinical practice were analyzed under the conditions used for the present method and did not interfere with belzutifan, cabozantinib, or the IS. Rs: resolution.

findings support the robustness and clinical applicability of the assay in settings where polypharmacy is common. Selection of the IS was carefully considered during method development. Several TKIs were initially evaluated; however, multiple candidates showed overlap with matrix-derived peaks or insufficient chromatographic separation from the analytes. Ibrutinib was ultimately selected as the IS because of its favorable chromatographic behavior and the low likelihood of co-administration with belzutifan and cabozantinib in patients with RCC.

3.2. Calibration curve and quantitation

Calibration curves for belzutifan and cabozantinib were constructed using the least-squares method. For belzutifan, the six-point calibration curve was expressed as $y = 0.002x - 0.0035$ ($r^2 = 0.9999$) and was linear over a concentration range of 50–4,000 ng/mL. For cabozantinib, the six-point calibration curve was expressed as $y = 0.0027x + 0.0559$ ($r^2 = 0.9998$) and was linear over a concentration range of 25–4,000 ng/mL, where y represents the peak height ratio of the analyte to the IS and x represents the analyte concentration (ng/mL). The calibration ranges established in the present study sufficiently cover clinically observed plasma concentrations. Reported steady-state plasma concentrations in clinical trials are 214–1,305 ng/mL for belzutifan and 383–1,148 ng/mL for cabozantinib (*3,16*). Therefore, the validated ranges are considered appropriate for TDM and pharmacokinetic evaluation in patients receiving these agents. Compared with previously reported HPLC–UV methods for the individual quantification of belzutifan or cabozantinib, the present assay provides comparable or broader calibration ranges while requiring only 50 µL of plasma. The use of a simple protein-precipitation procedure will also enable rapid sample preparation suitable for routine clinical analysis. The characteristics of previously reported analytical methods and the present method are summarized in Table 2. For belzutifan, the present assay provides a wider calibration range and lower plasma volume requirement than previously reported HPLC–UV methods (*11-13*), although with a modestly longer run time. For cabozantinib, the present method achieved a comparable calibration range with a substantially shorter run time than that reported by Maruyama *et al.* (*12*) and a lower limit of quantification than that reported by Yasu *et al.* (*13*). Collectively, these findings indicate that the present method maintains analytical performance comparable to or better than those of previously reported HPLC–UV assays while enabling simultaneous quantification of both analytes.

3.3. Precision, accuracy, and recovery

The intra- and inter-day coefficients of variation (CVs), accuracies, and recoveries for belzutifan and

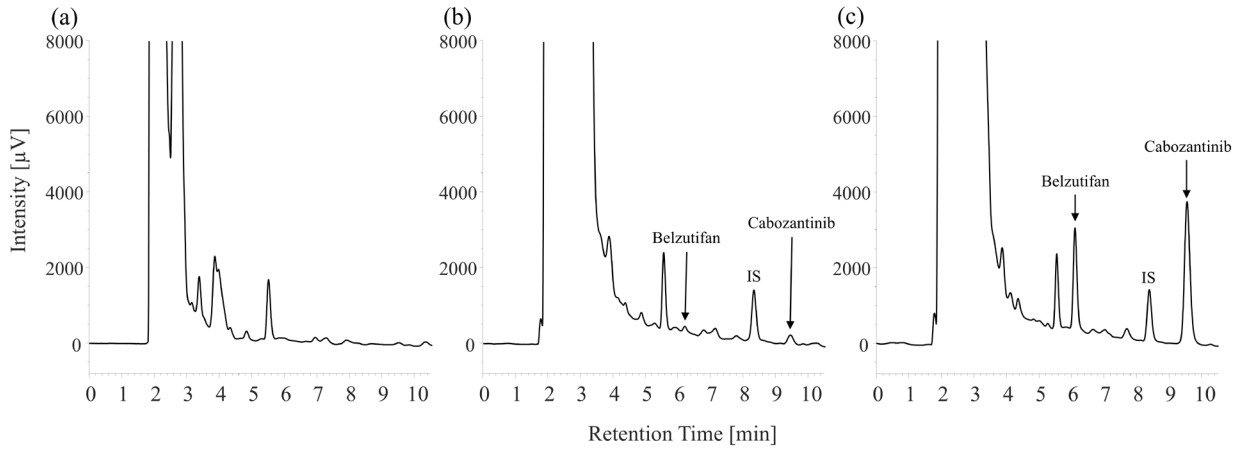


**Figure 2. Chromatograms of (a) blank plasma sample, (b) plasma sample containing belzutifan 50 ng/mL (limit of quantitation (LOQ)) and cabozantinib 25 ng/mL (LOQ), and (c) plasma sample containing belzutifan 1,000 ng/mL and cabozantinib 1,000 ng/mL.**

**Table 2. Comparison of present and previous methods of measuring plasma belzutifan and cabozantinib concentrations using HPLC-UV**

| | Present method | Kolli *et al.* (*11*) | Maruyama *et al.* (*12*) | Yasu *et al.* (*13*) |
|---|---|---|---|---|
| Analysis time (min) | 10.5 | 5 | 18 | 8 |
| Required plasma volume (µL) | 50 | 75 | 100 | 50 |
| Target agent | Belzutifan and cabozantinib | Belzutifan | Cabozantinib | Cabozantinib |
| Calibration range (ng/mL) | Belzutifan 50–4,000, Cabozantinib 25–4,000 | 75–3,000 | 25–4,000 | 50–5,000 |

cabozantinib are summarized in Table 3. For belzutifan, all intra- and inter-day CVs were below 5.41%. The intra-day accuracy ranged from −6.50% to 5.12%, whereas the inter-day accuracy ranged from −1.86% to 4.99%. For cabozantinib, all intra- and inter-day CVs were below 12.25%, with intra- and inter-day accuracies ranging from −5.47% to 0.96% and −1.55% to 4.95%, respectively.

These validation results satisfied the acceptance criteria defined in the U.S. FDA bioanalytical method validation guidelines (*14*), demonstrating adequate reproducibility and reliability for quantitative analysis. Both belzutifan and cabozantinib exhibit exposure-dependent toxicities, and clinical studies evaluating the combination of belzutifan and cabozantinib have recently been conducted. This combination therapy may become a treatment option for RCC in the future. Despite this increasing clinical relevance, no analytical method for simultaneous quantification of these agents in human plasma has previously been reported. Therefore, the validated precision and accuracy achieved in the present study support the potential utility of this assay for TDM applications in routine laboratory settings.

3.4. Stability

Stability studies were conducted under conditions relevant to the handling and storage of clinical samples. Belzutifan and cabozantinib in human plasma were stable for 6 h at room temperature (22°C), for 24 h at 4°C, for 3 months at −60°C, and after three freeze–thaw cycles. The results are summarized in Table 4. These findings indicate that the present assay is sufficiently robust for routine clinical use, including sample transport, temporary refrigerated storage, long-term frozen storage, and repeated freeze–thaw handling during reanalysis procedures.

3.5. Clinical applicability and potential utility for TDM

We established and validated the first HPLC–UV method capable of simultaneously quantifying belzutifan and cabozantinib in human plasma. Because HPLC–UV systems are widely available in hospital laboratories, the developed assay may provide a practical and accessible platform for TDM implementation in routine clinical practice. This method may be particularly useful in patients with RCC complicated by hepatic and/or renal impairment. Although belzutifan exposure is reportedly unaffected by mild hepatic dysfunction and mild-to-moderate renal dysfunction (*3*), cabozantinib exposure

**Table 3. Intra- and inter-day precision and accuracy results for belzutifan and cabozantinib in human plasma using the proposed HPLC method (*n*=5)**

| Added belzutifan concentration (ng/mL) | Intra-day (*n* = 5) | | | Inter-day (*n* = 5) | | | Recovery (%) |
|---|---|---|---|---|---|---|---|
| | Detected (ng/mL) mean ± SD | CV (%) | Accuracy (%) | Detected (ng/mL) mean ± SD | CV (%) | Accuracy (%) | |
| 50 | 52.56 ± 2.84 | 5.41 | 5.12 | 52.23 ± 1.90 | 3.64 | 4.46 | 93.08% |
| 100 | 95.70 ± 4.46 | 4.66 | −4.30 | 104.99 ± 4.57 | 4.36 | 4.99 | 90.65% |
| 500 | 467.48 ± 6.56 | 1.40 | −6.50 | 492.51 ± 11.40 | 2.31 | −1.50 | 95.54% |
| 1000 | 948.14 ± 19.40 | 2.05 | −5.19 | 997.28 ± 19.56 | 1.96 | −0.27 | 99.52% |
| 2000 | 1919.93 ± 10.72 | 0.56 | −4.00 | 1969.00 ± 48.19 | 2.45 | −1.55 | 101.17% |
| 4000 | 3792.91 ± 100.38 | 2.65 | −5.18 | 3925.42 ± 90.76 | 2.31 | −1.86 | 100.10% |
| Added cabozantinib concentration (ng/mL) | Detected (ng/mL) mean ± SD | CV (%) | Accuracy (%) | Detected (ng/mL) mean ± SD | CV (%) | Accuracy (%) | Recovery (%) |
| 25 | 24.07 ± 0.99 | 4.13 | −3.70 | 25.66 ± 3.14 | 12.25 | 2.63 | 103.41% |
| 50 | 50.48 ± 0.80 | 1.59 | 0.96 | 52.48 ± 1.73 | 3.30 | 4.95 | 106.76% |
| 500 | 472.65 ± 18.60 | 3.94 | −5.47 | 494.24 ± 1.73 | 0.35 | −1.15 | 102.67% |
| 1000 | 959.47 ± 29.57 | 3.08 | −4.05 | 997.72 ± 26.16 | 2.62 | −0.23 | 97.24% |
| 2000 | 1928.01 ± 48.21 | 2.50 | −3.60 | 1972.51 ± 69.00 | 3.50 | −1.37 | 95.20% |
| 4000 | 3846.98 ± 110.19 | 2.86 | −3.83 | 3937.80 ± 158.42 | 4.02 | −1.55 | 96.11% |

**Table 4. Stability analysis**

| Stability test conditions | Ratio of the plasma belzutifan concentration to the spiked value (%) | | | Ratio of the plasma cabozantinib concentration to the spiked value (%) | | |
|---|---|---|---|---|---|---|
| | 50 ng/mL (mean ± S.D.) | 1,000 ng/mL (mean ± S.D.) | 4,000 ng/mL (mean ± S.D.) | 25 ng/mL (mean ± S.D.) | 1,000 ng/mL (mean ± S.D.) | 4,000 ng/mL (mean ± S.D.) |
| Benchtop storage (22°C, 6 h) | 98.56 ± 5.55 | 101.33 ± 0.24 | 101.63 ± 0.85 | 87.48 ± 6.48 | 97.80 ± 0.61 | 99.40 ± 1.32 |
| Short-term storage (4°C, 24 h) | 91.71 ± 12.76 | 90.59 ± 2.10 | 95.44 ± 1.89 | 98.30 ± 7.99 | 102.25 ± 1.83 | 101.08 ± 0.69 |
| Long-term storage (−60°C, 3 months) | 94.27 ± 13.08 | 97.54 ± 1.65 | 97.49 ± 2.93 | 96.27 ± 11.53 | 98.56 ± 1.60 | 98.05 ± 3.86 |
| Freeze–thaw, three cycles (−60°C to room temperature) | 103.01 ± 4.38 | 97.59 ± 1.56 | 95.31 ± 1.80 | 88.69 ± 7.03 | 96.97 ± 0.93 | 97.79 ± 1.50 |

increases in such patients, with the AUC elevated by 6–81% (*17*). In addition, cabozantinib has a prolonged elimination half-life of approximately 99 h and requires approximately 15 days to reach steady state (*18*). Consideration of these pharmacokinetic characteristics may support individualized dosing strategies and extended dosing intervals aimed at reducing toxicity and treatment costs (*19*). Belzutifan exposure is also influenced by genetic polymorphisms. In UGT2B17/CYP2C19 dual poor metabolizers, the elimination half-life is prolonged by 14.3 h compared with that in UGT2B17 extensive metabolizers and CYP2C19 non-poor metabolizers (*3*). Therefore, TDM of belzutifan may facilitate optimization of systemic exposure and individualized dose adjustment according to genetic background.

The present method has several implementation-oriented advantages. First, the assay was established using cost-efficient and widely available HPLC–UV instrumentation while meeting FDA bioanalytical validation criteria, thereby lowering the barrier to clinical adoption. Second, the workflow relies on a simple protein-precipitation procedure using chilled methanol and requires only 50 μL of plasma, resulting in low per-sample costs and minimal hands-on time. Third, the absence of interference from commonly co-administered medications supports applicability in oncology settings where polypharmacy is common. Collectively, these features suggest that the assay has strong potential for integration into routine clinical workflows and multicenter implementation.

This study has certain limitations. First, validation was performed exclusively using spiked plasma samples, and patient-derived clinical samples were not evaluated. Additional studies using actual patient samples, including specimens with high and low drug concentrations, are warranted to further confirm clinical applicability. Second, comparison with LC–MS/MS methods, which remain the gold standard for drug quantification, was not performed. Future studies incorporating cross-platform comparisons, such as Bland–Altman analysis, may help confirm analytical agreement and facilitate broader implementation of the method.

**Acknowledgements**

Yoshito Gando received the Nagai Memorial Research Scholarship from the Pharmaceutical Society of Japan, which provided personal support to this author.

*Funding*: Yoshito Gando received the Nagai Memorial Research Scholarship from the Pharmaceutical Society of Japan, which provided personal support to this author.

*Conflict of Interest*: The authors have no conflicts of interest to disclose.

**References**

1. Choueiri TK, Powles T, Peltola K, *et al.* Belzutifan versus everolimus for advanced renal-cell carcinoma. N Engl J Med. 2024; 391:710-721.
2. Choueiri TK, Escudier B, Powles T, *et al.* Cabozantinib versus everolimus in advanced renal-cell carcinoma. N Engl J Med. 2015; 373:1814-1823.
3. Marathe DD, Jauslin PM, Kleijn HJ, de Miranda Silva C, Chain A, Bateman T, Shaw PM, Abraham AK, Kauh EA, Liu Y, Perini RF, de Alwis DP, Jain L. Population pharmacokinetic analyses for belzutifan to inform dosing considerations and labeling. CPT Pharmacometrics Syst Pharmacol. 2023; 12:1499-1510.
4. Okano M, Ueda T, Nishitani Y, Kano H, Ikekita A, Kageyama S. UDP-glucuronosyltransferase 2B17 genotyping in Japanese athletes and evaluation of the current sports drug testing for detecting testosterone misuse. Drug Test Anal. 2013; 5:166-181.
5. Kimura M, Ieiri I, Mamiya K, Urae A, Higuchi S. Genetic polymorphism of cytochrome P450s, CYP2C19, and CYP2C9 in a Japanese population. Ther Drug Monit. 1998; 20:243-247.
6. Marathe DD, Jauslin PM, Jan Kleijn H, De Miranda Silva C, Chain A, Abraham AK, Kauh EA, Liu Y, Perini RF, Alwis DP, Jain L. Exposure-response analyses for belzutifan to inform dosing considerations and labeling. J Clin Pharmacol. 2024; 64:1246-1258.
7. Cerbone L, Combarel D, Geraud A, *et al.* Association of cabozantinib pharmacokinetics, progression and toxicity in metastatic renal cell carcinoma patients: results from a pharmacokinetics/pharmacodynamics study. ESMO Open. 2021; 6:100312.
8. Nokihara H, Nishio M, Yamamoto N, Fujiwara Y, Horinouchi H, Kanda S, Horiike A, Ohyanagi F, Yanagitani N, Nguyen L, Yaron Y, Borgman A, Tamura T. Phase 1 study of cabozantinib in Japanese patients with expansion cohorts in non-small-cell lung cancer. Clin Lung Cancer. 2019; 20:e317-e328.
9. Géraud A, Combarel D, Funck-Brentano C, Beaulieu Q, Zahr N, Broutin S, Spano JP, Massard C, Besse B, Gougis P. A score to predict the clinical usefulness of therapeutic drug monitoring: Application to oral molecular targeted therapies in cancer. Clin Pharmacol Ther. 2024; 116:678-689.
10. Choueiri TK, McDermott DF, Merchan J, Bauer TM, Figlin R, Heath EI, Michaelson MD, Arrowsmith E, D'Souza A, Zhao S, Roy A, Perini R, Vickery D, Tykodi SS. Belzutifan plus cabozantinib for patients with advanced clear cell renal cell carcinoma previously treated with immunotherapy: an open-label, single-arm, phase 2 study. Lancet Oncol. 2023; 24:553-562.
11. Kolli P, Galla R. Bioanalytically validated LC-UV method for estimation of hypoxia-inducible factor-2 alpha (HIF-2α) inhibitor in spiked human plasma. Curr Trends Biotechnol Pharm. 2025; 19:126-132.
12. Maruyama S, Kato M, Hiraga T, Ishida M, Kanno H. Quantitative determination of plasma cabozantinib concentration using HPLC-UV and its application to patients with renal cell carcinoma. Biomed Chromatogr. 2023; 37:e5599.
13. Yasu T, Gando Y, Nishijima R, Ikuta R, Suzuki M, Shirota M. Plasma cabozantinib level measurement in patients with renal cell and hepatocellular carcinomas using a simple HPLC-UV method suitable for clinical application.

Curr Oncol. 2023; 30:4871-4879.
14. US DHHS, FDA, CDER, CVM. Guidance for Industry: Bioanalytical method validation. US Department of Health and Human Services, Food and Drug Administration, Center for Drug Evaluation and Research and Center for Veterinary Medicine, Rockville, MD, 2018.
15. Brown JR, Eichhorst B, Hillmen P, *et al.* Zanubrutinib or ibrutinib in relapsed or refractory chronic lymphocytic leukemia. N Engl J Med. 2023; 388:319-332.
16. Nguyen L, Chapel S, Tran BD, Lacy S. Cabozantinib exposure-response analyses of efficacy and safety in patients with advanced hepatocellular carcinoma. J Pharmacokinet Pharmacodyn. 2019; 46:577-589.
17. Nguyen L, Holland J, Ramies D, Mamelok R, Benrimoh N, Ciric S, Marbury T, Preston RA, Heuman DM, Gavis E, Lacy S. Effect of renal and hepatic impairment on the pharmacokinetics of cabozantinib. J Clin Pharmacol. 2016; 56:1130-1140.
18. Lyseng-Williamson KA. Cabozantinib as first-line treatment in advanced renal cell carcinoma: a profile of its use. Drugs Ther Perspect. 2018; 34:457-465.
19. Tan Z, Völler S, Yin A, Rieborn A, Gelderblom AJ, van der Hulle T, Knibbe CAJ, Moes DJAR. Population pharmacokinetics of cabozantinib in metastatic renal cell carcinoma patients: Towards drug expenses saving regimens. Clin Pharmacokinet. 2024; 63:857-869.

Received May 16, 2026; Revised August 17, 2026; Accepted August 18, 2026.

**Address correspondence to:*
Takeo Yasu, Department of Clinical Pharmacodynamics and Toxicology Analytics, Meiji Pharmaceutical University, 2-522-1, Noshio, Kiyose, Tokyo 204-8588, Japan.
E-mail: yasutakeo@my-pharm.ac.jp

Released online in J-STAGE as advance publication August 26, 2026.

**Brief Report**

DOI: 10.5582/ddt.2026.01034

# Nicotine administration selectively inhibits kainate-induced *Arc* and *junB* but not *c-fos* and *egr1* mRNA expression in mouse cerebral cortex

**Daisuke Ihara[§], Yuna Kato[§], Akiko Tabuchi[*]**

Laboratory of Molecular Neurobiology, Graduate School of Medicine and Pharmaceutical Sciences, University of Toyama, Toyama, Japan.

**SUMMARY**: The nicotinic acetylcholine receptor is an ion channel receptor that is highly expressed in the brain and can cooperatively propagate several signals with other ion channel receptors in neurons. However, little is known about how nicotinic acetylcholine and kainate receptors, both of which enable cation influx into neurons, cooperatively regulate immediate early genes. In this study, we administrated both ligands, nicotine and kainate, into mice and investigated alterations of the immediate early genes *activity-regulated cytoskeleton-associated protein* (*Arc*), *junB*, *c-fos*, and *egr1* in the cerebral cortex, hippocampus, olfactory bulb, and cerebellum. Kainate alone showed a tendency to induce all four immediate early genes in all four brain regions, whereas nicotine alone did not induce them strongly. However, pretreatment of nicotine before administration of kainate showed differential effects of nicotine on mRNA expression across different brain regions. Nicotine selectively inhibited kainate-induced *Arc* and *junB* mRNA expression in the cerebral cortex. These findings suggest that nicotine influences specific brain regions *via* the induction of certain immediate early genes.

***Keywords***: nicotine, kainate, *Arc*, *junB*, *egr1*, *c-fos*

## 1. Introduction

Nicotinic acetylcholine receptors (nAchRs) are enriched in the nervous system and play versatile roles in brain functions; as such, they may be promising therapeutic targets against brain disorders, including Alzheimer's disease (*1*). Two major nAchRs, composed of either α4β2 or α7 subunits, are predominantly expressed in the nervous system and act as ligand-gated ion channels with $Ca^{2+}$ permeability (*1*). Besides these major subunits, several other nAchR subunits are distributed across different brain regions, probably resulting in diverse outputs for fine-tuning brain functions (*1*). The binding of nicotine or acetylcholine to nAchRs triggers depolarization and $Ca^{2+}$ influx. This activates multiple intracellular signal transduction pathways that include phosphatidylinositol 3-kinase, protein kinase A, $Ca^{2+}$-calmodulin-dependent protein kinases, protein kinase C, or the subsequent extracellular signal-regulated mitogen-activated protein kinase (*1*), which might affect gene expression in cultured neuronal cells and animals (*2-4*). Previously, it has been reported that several immediate early genes (IEGs) are regulated by nicotine in PC12 cells (*2*) and *in vivo*, *e.g.*, in rodents (*3,4*). In particular, administration of nicotine to rats resulted in the induction of *c-fos* and *activity-regulated cytoskeleton-associated protein* (*Arc*) (*5*).

The kainate receptor is an ionotropic glutamate receptor and well-known ion channel that causes depolarization in neurons (*6*). It regulates the expression of several IEGs (*7,8*), inducing the expression of *junB, c-fos, egr1* (7), and *Arc* genes (*9*), and also evokes seizure (*10,11*) and neurotoxicity (*12,13*).

The activation of nAchRs protects against glutamate-mediated neurotoxicity (*14*), and nAchR-mediated neuroprotection has been observed in the hippocampus (*15,16*), striatum (*17,18*), and substantia nigra (*19,20*). The activation of nAchR propagates phosphatidylinositol 3-kinase-Akt signaling and suppresses amyloid-β-induced neuronal damage (*16,21*). The neuroprotective effects of nAchRs on kainate-induced excitotoxicity have also been reported by studies that administered both nicotine and kainate *in vivo* (*22-24*).

As described above, the effects of nAchRs on pathological phenomena triggered by the activation of glutamate receptors have mostly been demonstrated in relation to the suppression of excitotoxicity. However, little is known about the molecular mechanisms underlying the interactions of nAchRs with glutamate receptors. Both nAchRs and kainate receptors can regulate gene expression through downstream signaling

pathways. However, it remains unresolved how IEGs are regulated by the pretreatment of nAchRs before activation of kainate receptors. Thus, the current study investigated how representative IEGs (*i.e.*, *Arc*, *junB*, *c-fos*, and *egr1*) are differentially regulated in distinct brain regions by intraperitoneal administration of nicotine and kainate in mice.

## 2. Materials and Methods

### 2.1. Animals

C57BL/6N male 7-week-old mice were purchased from Japan SLC (Hamamatsu, Shizuoka, Japan). All animal experiments were performed in accordance with the ARRIVE guidelines and the requirements of the Animal Care and Experimentation Committee of the University of Toyama, Sugitani Campus (approval numbers A2022PHA-7 and A2025PHA-11). All efforts were made to minimize animal suffering and the number of animals used.

### 2.2. Reagents and treatments

(−)-Nicotine hydrogen tartrate (N5260) and kainic acid monohydrate (kainate) (K0250) were purchased from Sigma-Aldrich (St. Louis, MO, USA). The mice were injected intraperitoneally with either saline (vehicle), 2 mg/kg nicotine dissolved in saline, or 30 mg/kg kainate dissolved in saline 2 h after nicotine administration. Animals were killed 30 min after kainate administration, and their brains were extracted.

### 2.3. RNA isolation and quantitative PCR (qPCR)

Total RNA was extracted from mouse brain tissues by the acid guanidine phenol-chloroform method. Total RNA was isolated by adding TRIsure (BIO-38032; Bioline, London, UK) to the tube with mouse brain and homogenizing the mixture with a polytron homogenizer (PT-2100, Kinematica AG, Malters, Switzerland), according to the manufacturer's instructions with minor modifications (*25*). After homogenization, total RNA was treated with RNase-free DNase I (TaKaRa, Shiga, Japan) to prevent contamination by genomic DNA. After the removal of DNase I, RNA (250 ng) was reverse-transcribed into cDNA using SuperScript II reverse transcriptase (Invitrogen), as previously described (*25*). To detect the mRNA levels of *Arc, junB, c-fos, egr1*, and glyceraldehyde-3-phosphate dehydrogenase (*Gapdh*) genes, qPCR was performed in 20 µL of 1 × SYBR Select Master Mix (4472908, Thermo Fisher Scientific), 2 µL of cDNA solution, and 0.2 µM of each primer. The Stratagene Mx3000P or Mx3005P Real-Time PCR system was used, and the thermal profile was as follows: pre-heating at 50°C for 2 min followed by 95°C for 2 min, denaturation at 95°C for 15 s, annealing at 58°C for 15 s, and extension at 72°C for 1 min for 40 cycles. Standard curves were generated for each gene using a plasmid DNA dilution series containing the target sequences. The primer sequences are provided in the Supplementary material (Table S1, *https://www.ddtjournal.com/action/getSupplementalData.php?ID=314*). Expression levels were normalized to *Gapdh* mRNA levels.

### 2.4. Statistical analysis

Data were presented as mean ± standard deviation (n = 3–4) and compared using two-way ANOVA or one-way ANOVA followed by a Tukey-Kramer or Scheffe *F* test. Differences were considered significant at $p < 0.05$. All statistical analyses were performed with Microsoft Excel 2013 (version 15.0.5127.1000).

## 3. Results and Discussion

A previous study already demonstrated that the IEGs, *Arc* and c-*fos* were activated in the rat brains by acute nicotine administration (*5*) and the previous study also suggest that these findings might be involved in nicotine-induced activation of the brain involved in stress and anxiety-linked behavior (*5*). On the other hand, it is reported that nicotine exerts the protective effect on kainate-induced neurotoxicity (*22-24*). These studies prompted us to investigate how IEGs are regulated by combinated treatment of nicotine and kainate to extend the previous study. To activate nAchRs prior to activation of kainate receptors in mice *in vivo*, we intraperitoneally administered their agonists: nicotine first and then kainate. Initially, we measured four IEGs (*Arc*, *junB*, *c-fos*, and *egr1*) by using RNAs isolated from cerebral cortices and qPCR. Nicotine alone did not significantly alter IEG expression; however, *Arc* and *junB* were slightly increased compared with the findings with the vehicle. Kainate alone significantly increased *Arc* and *junB* mRNA expression (Figures 1A and 1B). The expression of *c-fos and egr1* showed a slight increasing trend in the cerebral cortex stimulated with kainate (Figures 1C and 1D). Nicotine significantly inhibited the expression of *Arc* and *junB* but not *c-fos* and *egr1*, induced by kainate (Figures 1A–D).

Next, we assessed the expression of the four IEGs in the hippocampus (Figure 2). The expression of *c-fos* and *egr*1 was significantly induced by kainate alone (Figures 2C and 2D), and this increase was not decreased by the combined administration of nicotine and kainate (Figures 2C and 2D). Nicotine alone showed a tendency to decrease the expression of the four IEGs (Figures 2C and 2D). The expression of *Arc* and *junB* showed a slight increasing trend after kainate alone treatment; however, this increase was not significant and was not suppressed by nicotine (Figures 2A and 2B). Nicotine alone slightly decreased *junB* mRNA levels (Figure 2B).

In the olfactory bulb, kainate alone significantly

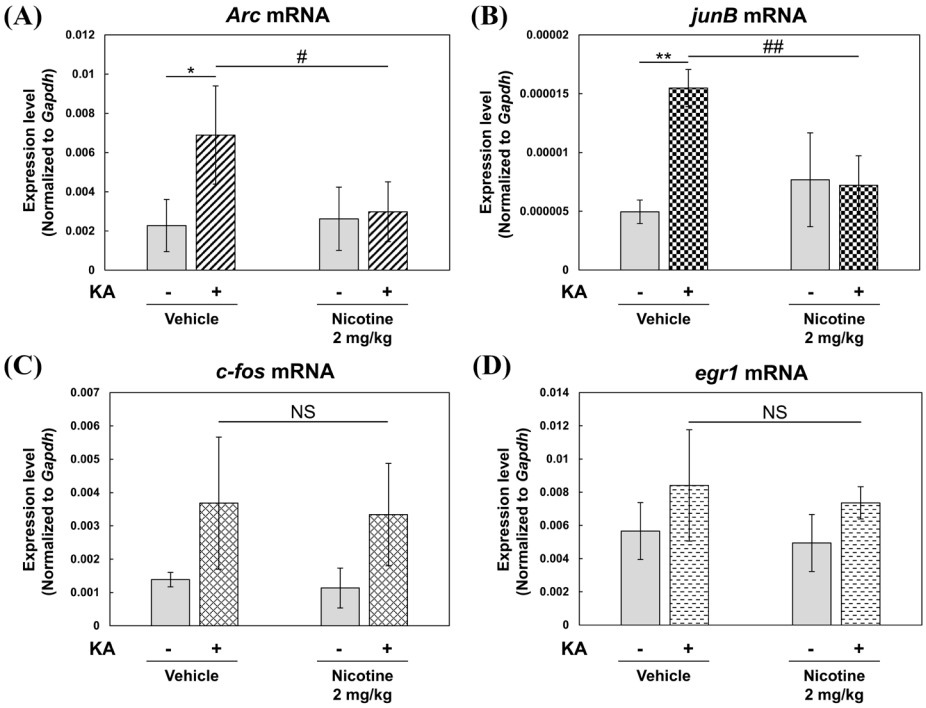


**Figure 1. Kainate-induced *Arc* and *junB* mRNA levels are suppressed by nicotine administration in the cerebral cortex.** Nicotine (2 mg/kg) and/or kainate (KA; 30 mg/kg) were administered into mice, and after 30 min, cerebral cortices were isolated, and total RNA was extracted and subjected to qPCR. (A–D) The mRNA expression levels of *Arc* (A), *junB* (B), *c-fos* (C), and *egr1* (D). Bars represent means ± SD ($n$ = 3–4). Interactions between nicotine and kainate were analyzed using two-way ANOVA. *$p$ = 0.0356 (A), **$p$ = 0.00190 (B), $p$ = 0.9420 (C) or $p$ = 0.8766 (D). Differences were analyzed using one-way ANOVA with a post hoc Tukey-Kramer (A and B) or Scheffe $F$ test (C). $^{*}p < 0.05$, $^{**}p < 0.01$ *vs.* control; $^{\#}p < 0.05$, $^{\#\#}p < 0.01$ *vs.* KA alone; NS, not significant *vs.* KA alone.

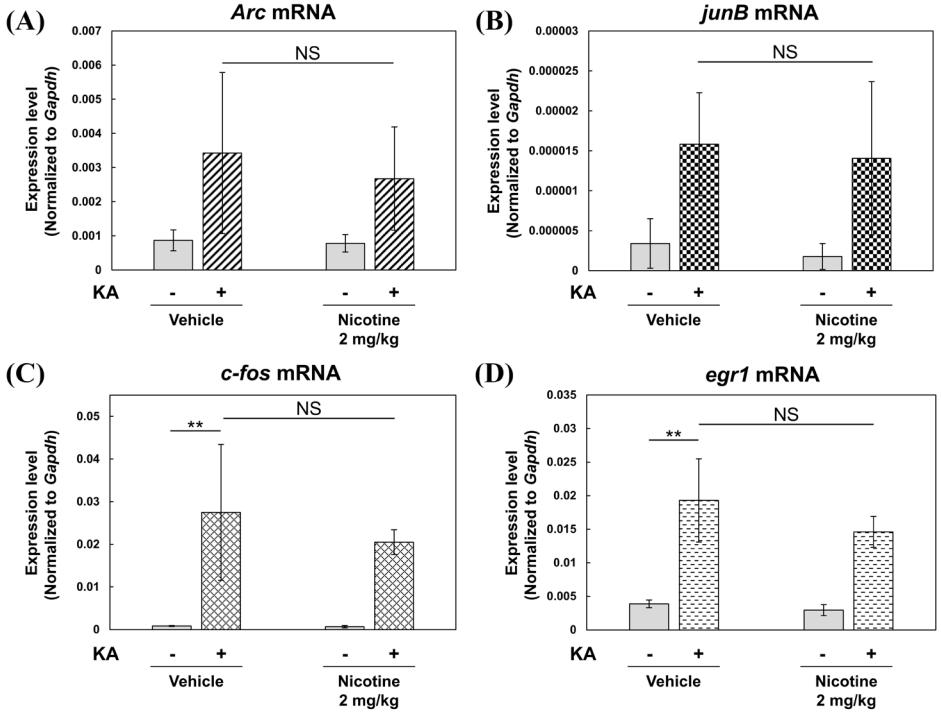


**Figure 2. Kainate-induced *Arc*, *junB*, *c-fos*, and *egr1* mRNA levels are not suppressed by nicotine administration in the hippocampus.** Nicotine (2 mg/kg) and/or kainate (KA; 30 mg/kg) were administered into mice, and after 30 min, hippocampi were isolated, and total RNA was extracted and subjected to qPCR. (A–D) The mRNA expression levels of *Arc* (A), *junB* (B), *c-fos* (C), and *egr1* (D). The bars represent means ± SD ($n$ = 4). Interactions between nicotine and kainate were analyzed using two-way ANOVA. $p$ = 0.6486 (A), $p$ = 0.9834 (B), $p$ = 0.4158 (C) or $p$ = 0.2836 (D). Differences were analyzed using one-way ANOVA with a post hoc Tukey-Kramer (B) or Scheffe $F$ test (C and D). $^{**}p < 0.01$ *vs*. control; NS, not significant *vs*. KA alone.

increased *junB* mRNA expression (Figure 3B) and showed a tendency to increase *Arc*, *c-fos*, and *egr*1 (Figures 3A, 3C, and 3D). Nicotine alone showed a tendency to decrease *junB* mRNA expression (Figure 3B).

In the cerebellum, kainate alone significantly increased *Arc*, *c-fos*, and *egr1* expression and showed a tendency to increase *junB* expression (Figures 4A–4D). Although the interaction between nicotine and kainate was observed in terms of *Arc* expression (Figure 4A, figure legend), post hoc test in kainate alone versus kainate plus nicotine did not show significant difference. Nicotine suppressed the kainate-induced increases in *c-fos* expression (Figure 4C).

In summary, nicotine differentially affected *Arc*, *junB*, *c-fos*, and *egr1* expression levels, also across different brain regions. In the case of combined administration of nicotine prior to kainate treatment, nicotine exerted an inhibitory effect on kainate-induced IEG mRNA expression. Excitatory neuronal activation is also induced by kainate, associated with seizure (*10,11*). Previously, the inhibitory effect of nicotine on kainate-induced wet dog shakes followed by motoric seizure has been reported (*23*). Taken together, therefore, the suppressive effect of nicotine on some of IEG expression may be due to the reduction of seizure. Notably, this suppressive effect of nicotine was not observed for all IEGs and in all brain regions. This indicates selective suppression, depending on the IEG and/or brain region. Especially in the cerebral cortex, nicotine selectively and strongly blocked kainate-induced *Arc* and *junB* mRNA expression.

The subunits of nAchRs have been reported to be spatiotemporally expressed in the central nervous system (*1,26*). The cerebral cortex expresses the subunits α2, α4, α5, and α7, and the hippocampus expresses these same subunits in addition to α3 (*1*). The cerebellum expresses the subunits α3, α4, and α7 (*1*). Thus, differential expression patterns of nAchR subunits across different brain regions might result in distinct nAchR channel properties in each brain region, further leading to different activation of downstream signaling and gene expression. In this study, we used 7-week-old mice to evaluate the effects of nicotine and kainate on IEG expression. Notably, nAchR subunit and thus channel variability during brain development may also play critical roles in physiological and pathological processes in the brain (*26*). Therefore, further studies are needed to investigate whether our findings can also be applied to neonatal or aged brain and whether alterations in IEG expression based on interactions between nAchRs and kainate receptors contribute to brain development and higher brain functions, such as learning and memory.

The molecular mechanisms by which nicotine inhibits kainate-induced IEG expression remain unknown. The neuroprotective role of nicotine against glutamate toxicity and the underlying mechanisms, which include

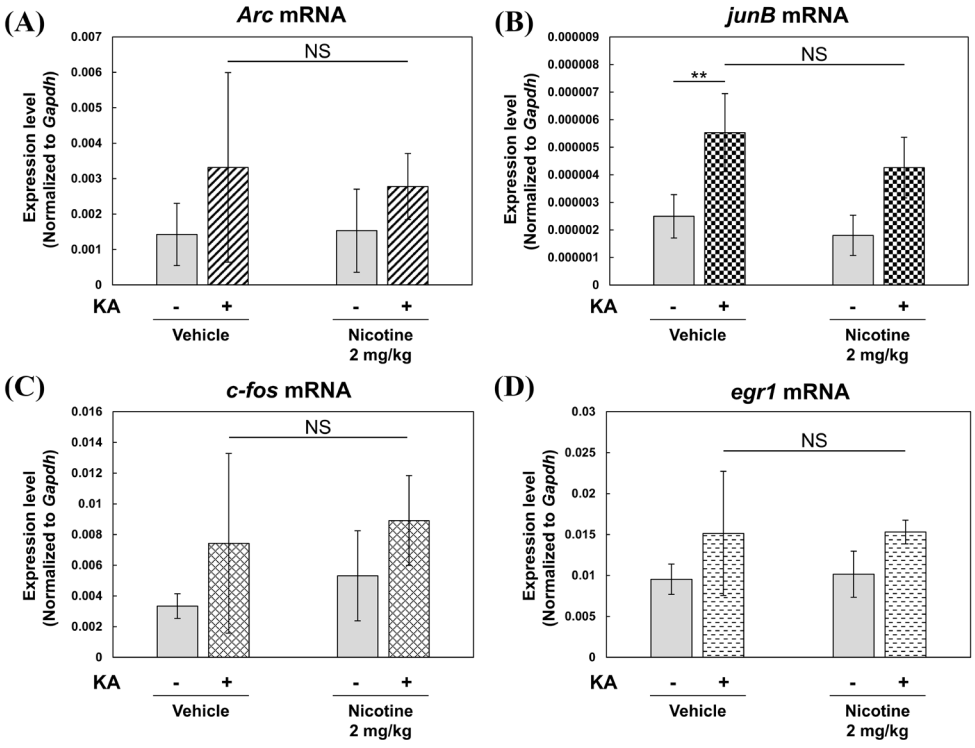


**Figure 3. Kainate-induced *junB* mRNA levels are not significantly suppressed by nicotine administration, and nicotine alone tends to decrease *junB* mRNA levels in the olfactory bulb.** Nicotine (2 mg/kg) and/or kainate (KA; 30 mg/kg) were administered into mice, and after 30 min, olfactory bulbs were isolated, and total RNA was extracted and subjected to qPCR. (A–D) The mRNA expression levels of *Arc* (A), *junB* (B), *c-fos* (C), and *egr1* (D). The bars represent means ± SD ($n$ = 3–4). Interactions between nicotine and kainate were analyzed using two-way ANOVA. $p = 0.6926$ (A), $p = 0.6164$ (B), $p = 0.8943$ (C) or $p = 0.9188$ (D). Differences were analyzed using one-way ANOVA with a post hoc Tukey-Kramer (B). $^{**}p < 0.01$ *vs.* control; NS, not significant *vs.* KA alone.

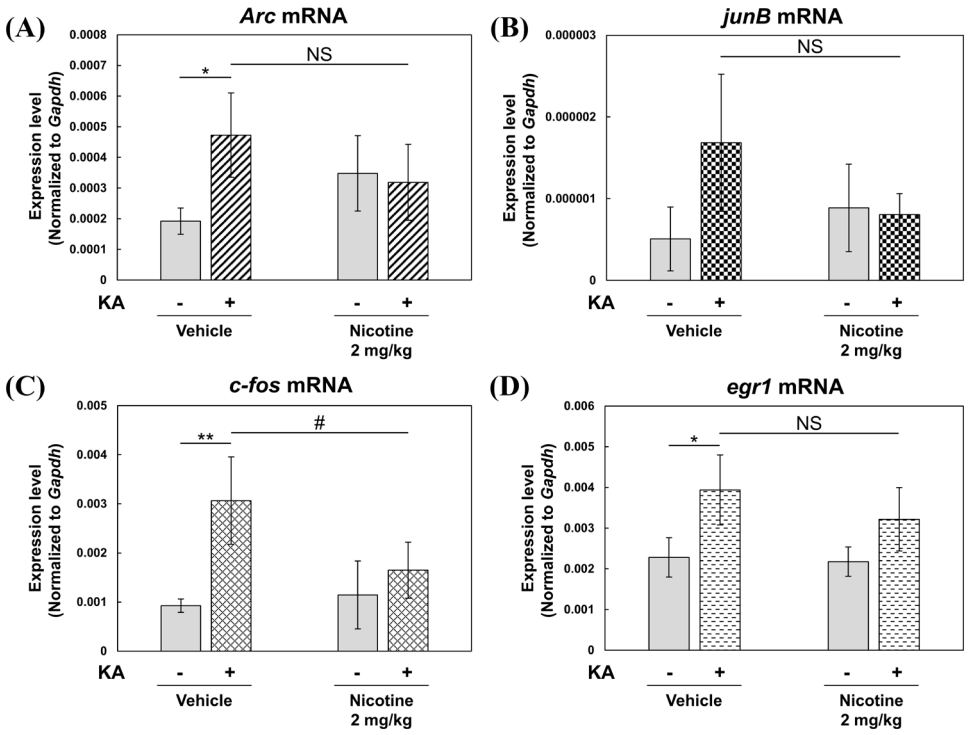


**Figure 4. Kainate induces *Arc*, *c-fos*, and *egr1* mRNA expression, and kainate-induced *c-fos* mRNA expression is suppressed by nicotine in the cerebellum.** Nicotine (2 mg/kg) and/or kainate (KA; 30 mg/kg) were administered into mice, and after 30 min, cerebelli were isolated, and total RNA was extracted and subjected to qPCR. (A–D) The mRNA expression levels of *Arc* (A), *junB* (B), *c-fos* (C), and *egr1* (D). The bars represent means ± SD (n = 3–4). Interactions between nicotine and kainate were analyzed using two-way ANOVA. $^{*}p = 0.0180$ (A), $p = 0.0542$ (B), $^{*}p = 0.0245$ (C) or $p = 0.3633$ (D). Differences were analyzed using one-way ANOVA with a post hoc Tukey-Kramer test. $^{*}p < 0.05$, $^{**}p < 0.01$ *vs.* control; $^{\#}p < 0.05$ *vs*. KA alone; NS, not significant *vs*. KA alone.

the phosphatidylinositol 3-kinase-Akt pathway (*21*) and non-neuronal cells such as microglia (*27,28*), might provide critical insights into the underlying mechanisms of the findings of this study. Among the affected IEGs, *Arc* and *junB* were particularly more sensitive to nicotine treatment in the cerebral cortex (Figure 1). This finding suggests that nicotine may block specific transcription factors or posttranscriptional events, which commonly and selectively drive *Arc* and *junB* gene expression. Serum response factor is one of the common transcription factors that regulate both *Arc* and *junB* genes (*29,30*), implying that, together with its regulatory complexes, it might be affected by nicotine and kainate in the cerebral cortex. In the present study, however, we did not take pharmacological or genetic approaches to elucidate the mechanisms as proposed above. Therefore, this study has limitations to fully explain the involvement of differential nAchRs subunits at differential brain regions and SRF transcriptional factor complex. To further address this molecular mechanism, investigations into the subcellular localization and posttranslational modification of specific transcription factor proteins *in vivo* are warranted.

A growing body of evidence is accumulating that shows that nAchRs and their ligands may be involved in brain health and diseases and represent therapeutic targets for neurodegenerative diseases (*1,26*). Studies on the effects of nicotine on gene expression should lead to a deeper understanding of the roles of nicotine and ultimately contribute to the development of novel therapeutic strategies for brain diseases.

**Acknowledgements**

This study was supported by the Smoking Research Foundation (to A.T.). The funder did not have any role in the study design, data collection or analysis, manuscript preparation, or the decision to submit the manuscript for publication. We thank Dr. Eva Lasic, PhD, from Edanz (*https://jp.edanz.com/ac*), for editing a draft of this manuscript.

*Funding*: None.

*Conflict of Interest*: The authors have no conflicts of interest to disclose.

**References**

1. Akaike A., Izumi Y. Nicotinic Acetylcholine Receptor Signaling in Neuroprotection (Akaike A, Shimohama S, Misu Y, eds.). Springer, Singapore, 2018; pp. 1-15.
2. Bartel DP, Sheng M, Lau LF, Greenberg ME. Growth factors and membrane depolarization activate distinct programs of early response gene expression: dissociation of fos and jun induction. Genes Dev. 1989; 3:304-313.
3. Koistinaho J, Pelto-Huikko M, Sagar SM, Dagerlind A, Roivainen R, Hokfelt T. Differential expression of

immediate early genes in the superior cervical ganglion after nicotine treatment. Neuroscience. 1993; 56:729-739.
4. O'Hara BF, Macdonald E, Clegg D, Wiler SW, Andretic R, Cao VH, Miller JD, Heller HC, Kilduff TS. Developmental changes in nicotinic receptor mRNAs and responses to nicotine in the suprachiasmatic nucleus and other brain regions. Brain Res Mol Brain Res. 1999; 66:71-82.
5. Schmitt HF, Huang LZ, Son JH, Pinzon-Guzman C, Slaton GS, Winzer-Serhan UH. Acute nicotine activates c-fos and activity-regulated cytoskeletal associated protein mRNA expression in limbic brain areas involved in the central stress-response in rat pups during a period of hypo-responsiveness to stress. Neuroscience. 2008; 157:349-59.
6. Contractor A, Mulle C, Swanson GT. Kainate receptors coming of age: milestones of two decades of research. Trends Neurosci. 2011; 34:154-163.
7. Zagulska-Szymczak S, Filipkowski RK, Kaczmarek L. Kainate-induced genes in the hippocampus: lessons from expression patterns. Neurochem Int. 2001; 38:485-501.
8. Collaco-Moraes Y, De Belleroche J. Differential temporal patterns of expression of immediate early genes in cerebral cortex induced by intracerebral excitotoxin injection: sensitivity to dexamethasone and MK-801. Neuropharmacology. 1995; 34:521-531.
9. Li L, Carter J, Gao X, Whitehead J, Tourtellotte WG. The neuroplasticity-associated arc gene is a direct transcriptional target of early growth response (Egr) transcription factors. Mol Cell Biol. 2005; 25:10286-10300.
10. Ben-Ari Y. Limbic seizure and brain damage produced by kainic acid: mechanisms and relevance to human temporal lobe epilepsy. Neuroscience. 1985; 14:375-403.
11. Lévesque M, Wang S, Macey-Dare ADB, Salami P, Avoli M. Evolution of interictal activity in models of mesial temporal lobe epilepsy. Neurobiol Dis. 2023; 180:106065.
12. Nadler JV, Perry BW, Cotman CW. Intraventricular kainic acid preferentially destroys hippocampal pyramidal cells. Nature. 1978; 271:676-677.
13. Jakaria M, Park SY, Haque ME, Karthivashan G, Kim IS, Ganesan P, Choi DK. Neurotoxic Agent-Induced Injury in Neurodegenerative Disease Model: Focus on Involvement of Glutamate Receptors. Front Mol Neurosci. 2018; 11:307.
14. Kaneko S, Maeda T, Kume T, Kochiyama H, Akaike A, Shimohama S, Kimura J. Nicotine protects cultured cortical neurons against glutamate-induced cytotoxicity *via* alpha7-neuronal receptors and neuronal CNS receptors. Brain Res. 1997; 765:135-140.
15. Dajas-Bailador FA, Lima PA, Wonnacott S. The alpha7 nicotinic acetylcholine receptor subtype mediates nicotine protection against NMDA excitotoxicity in primary hippocampal cultures through a $Ca^{2+}$ dependent mechanism. Neuropharmacology. 2000; 39:2799-2807.
16. Alkadhi KA. Neuroprotective Effects of Nicotine on Hippocampal Long-Term Potentiation in Brain Disorders. J Pharmacol Exp Ther. 2018; 366:498-508.
17. Ohnishi M, Katsuki H, Takagi M, Kume T, Akaike A. Long-term treatment with nicotine suppresses neurotoxicity of, and microglial activation by, thrombin in cortico-striatal slice cultures. Eur J Pharmacol. 2009; 602:288-293.
18. Mouhape C, Costa G, Ferreira M, Abin-Carriquiry JA, Dajas F, Prunell G. Nicotine-Induced Neuroprotection in Rotenone *In Vivo* and *In Vitro* Models of Parkinson's Disease: Evidences for the Involvement of the Labile Iron Pool Level as the Underlying Mechanism. Neurotox Res. 2019; 35:71-82.
19. Takeuchi H, Yanagida T, Inden M, *et al.* Nicotinic receptor stimulation protects nigral dopaminergic neurons in rotenone-induced Parkinson's disease models. J Neurosci Res. 2009; 87:576-585.
20. Zhgenti N, Bakuradze E, Bibilashvili O, Koshoridze N. The role of BDNF/PI3K/AKT/Nrf2 signaling in nicotine's protective effects against MPTP-induced Parkinson's disease. Neurosci Lett. 2025; 868:138412.
21. Kihara T, Shimohama S, Sawada H, Honda K, Nakamizo T, Shibasaki H, Kume T, Akaike A. alpha 7 nicotinic receptor transduces signals to phosphatidylinositol 3-kinase to block A beta-amyloid-induced neurotoxicity. J Biol Chem. 2001; 276:13541-13546.
22. Borlongan CV, Shytle RD, Ross SD, Shimizu T, Freeman TB, Cahill DW, Sanberg PR. (−)-nicotine protects against systemic kainic acid-induced excitotoxic effects. Exp Neurol. 1995; 136:261-265.
23. Shytle RD, Borlongan CV, Sanberg PR. Nicotine blocks kainic acid-induced wet dog shakes in rats. Neuropsychopharmacology. 1995; 13:261-264.
24. Kaur J, Rauti R, Nistri A. Nicotine-mediated neuroprotection of rat spinal networks against excitotoxicity. Eur J Neurosci. 2018; 47:1353-1374.
25. Fukuchi M, Izumi H, Mori H, Kiyama M, Otsuka S, Maki S, Maehata Y, Tabuchi A, Tsuda M. Visualizing changes in brain-derived neurotrophic factor (BDNF) expression using bioluminescence imaging in living mice. Sci Rep. 2017; 7:4949.
26. Dwyer JB, McQuown SC, Leslie FM. The dynamic effects of nicotine on the developing brain. Pharmacol Ther. 2009; 122:125-139.
27. Egea J, Buendia I, Parada E, Navarro E, Leon R, Lopez MG. Anti-inflammatory role of microglial alpha7 nAChRs and its role in neuroprotection. Biochem Pharmacol. 2015; 97:463-472.
28. Qin Y, Yan X, Luo Y, Wang H, Tian Y, Wu X, Chen H, Hou H, Hu Q. Nicotine Regulates LPS-Induced Inflammatory Responses in HMC3 Microglia and Exerts Neuronal Protection. Mediators Inflamm. 2026; 2026:4652344.
29. Kawashima T, Okuno H, Nonaka M, Adachi-Morishima A, Kyo N, Okamura M, Takemoto-Kimura S, Worley PF, Bito H. Synaptic activity-responsive element in the Arc/Arg3.1 promoter essential for synapse-to-nucleus signaling in activated neurons. Proc Natl Acad Sci U S A. 2009; 106:316-321.
30. Perez-Albuerne ED, Schatteman G, Sanders LK, Nathans D. Transcriptional regulatory elements downstream of the JunB gene. Proc Natl Acad Sci U S A. 1993; 90:11960-11964.

Received May 19, 2026; Revised July 28, 2026; Accepted August 12, 2026.

[§]These authors contributed equally to this work.

**Address correspondence to:*
Akiko Tabuchi, Laboratory of Molecular Neurobiology, Graduate School of Medicine and Pharmaceutical Sciences, University of Toyama, 2630 Sugitani, Toyama 930-0194, Japan.
E-mail: atabuchi@pha.u-toyama.ac.jp

Released online in J-STAGE as advance publication August 21, 2026.

***Brief Report***

DOI: 10.5582/ddt.2026.01036

# Sensory testing assessment of dosage forms designed to resist overdose

**Kazuki Nagashima*, Rin Tanaka, Fumiya Owase, Yuko Sekine**

Laboratory of Practical Pharmacy, Graduate School and Faculty of Pharmaceutical Sciences, Chiba University, Chiba, Japan.

**SUMMARY**: Overdose incidence has increased among young individuals, particularly involving psychotropic and over-the-counter (OTC) drugs. However, there is limited information regarding how the physical form of medications—such as tablet size or thickness—affects the ability to take large doses. This study aims to determine which tablet characteristics (size, thickness, and volume) can discourage overdose by using sensory testing methods. The diameters and thicknesses of tablets commonly used in overdosing were measured. Additionally, dummy tablets were three-dimensionally (3D) printed, after which sensory tests were conducted to evaluate how many tablets could be comfortably consumed in large quantities, as well as the ease of consumption, rated on a 5-point scale. The respondents were students (average age: 21.3 ± 2.1 years, $n$ = 253). Results indicate that OTC drugs typically have larger and thicker tablets compared with prescription drugs. Sensory tests of 3D-printed dummy tablets found that smaller tablets are easier to ingest in large numbers, whereas larger and thicker tablets are harder to consume in bulk. For tablets with the same diameter, a 5-mm thickness tends to make overdose more difficult compared with a 2-mm thickness. Importantly, tablets with a combined diameter and thickness of 13 mm or more and a volume of at least 190 $mm^3$ are less likely to be overdosed. These findings can assist pharmacists in selecting appropriate dosage forms for patients at risk of overdose and provide pharmaceutical companies with guidance during product development.

***Keywords***: Overdose, sensory test, tablets, 3D printer, pharmacist

## 1. Introduction

The incidence of overdose among young individuals has increased, particularly involving psychotropic and over-the-counter (OTC) medications (*1–3*). Patients who have experienced an overdose often repeat the behavior for self-harm or suicide attempts (*4*). Notably, even when the initial intent is self-harm, the hazard ratio for subsequent suicidal behavior compared with controls is approximately 42 (*5*). Tablets are commonly used in self-harm overdoses and are frequently administered orally (*6*). Careful selection of dosage forms is critical, particularly for patients prone to recurrent overdoses (*4*). Consideration should be given to tablet sizes that are less likely to cause overdose.

Pharmacists and registered drug sellers are responsible for preventing overdoses by acting as gatekeepers (*7*). These professionals must also recognize signs of suicidal ideation, actively listen, and monitor individuals (*8,9*) while using their expertise to select and modify dosage forms (diameter and thickness) based on available medications.

Research on tablet formulations has primarily focused on improving patient adherence by assessing preferred formulations. For example, studies indicate that participants favor model formulations in which the sum of the major/minor axes and thickness does not exceed 22 mm, with thickness ranging from 2 to 6 mm (*10,11*). Additional investigations into swallowing difficulties have examined the effects of head position relative to tablet size (*12*) and the impact of coatings (*13*). However, in scenarios where individuals intentionally ingest large quantities of tablets, perceptions of tablet size and dimensions may differ from those observed in everyday contexts; data addressing this aspect are currently insufficient. The ideal tablet size should balance deterring overdose and ensuring ease of swallowing for typical patients.

Psychotropic drugs are most frequently implicated in overdoses (*1*). Similarly, for OTC drugs such as caffeine, diphenhydramine, and cold medicines, information regarding ingredient characteristics and types is readily available (*14-16*). Furthermore, oral tablets constitute the predominant dosage form associated with overdoses. However, empirical evidence regarding dosage forms, specifically tablet size or thickness that are less

conducive to large-dose ingestion, is limited.

To address this gap, the present study utilizes sensory testing to identify appropriate tablet dosage forms (including diameter, thickness, and volume) that may reduce the likelihood of consuming large amounts of medication.

## 2. Materials and Methods

### 2.1. Measurement of OTC and prescription drug tablet diameter and thickness

This study examined 19 types of OTC drugs commonly implicated in overdoses, as identified by the FY2022 Ministry of Health, Labor, and Welfare Administrative Promotion Research Project Subsidy (Pharmaceutical and Medical Device Regulatory Science Policy Research Project) Participating Research Report in Japan (*17*). Tablet diameter and thickness for OTC drugs were measured using a digital caliper (Model: BDC100, measurement precision: ± 0.03 mm, AS ONE, Osaka, Japan), with mean values calculated from four replicates ($n$ = 4). For prescription drugs, analysis focused on Classes 1, 2, and 3 psychotropic drugs designated under the Narcotics and Psychotropic Substances Control Law in Japan. The dimensions of 232 original and generic circular tablet formulations were assessed using Pharmaceutical Interview Forms, which are standardized documents provided by pharmaceutical companies in Japan.

### 2.2. Fabrication of dummy tablets *via* three-dimensional (3D) printing

Dummy tablets were modeled using 3D Builder software (Microsoft Corporation, Redmond, WA, USA). Cylindrical models were constructed, setting diameter (major and minor axes on the X- and Y-axes, respectively) and thickness (Z-axis). Tablet edges were chamfered to conform to standard tablet geometry (Figure 1), and all dummy tablets were produced in white. In total, 10 types of dummy tablets were created,


**Figure 1. Diagram of dummy tablets produced using a 3D printer.** (A) Top view of dummy tablets. (B) Side view of dummy tablets; d: diameter (mm), t: thickness (mm). (C) Tablets and packs were used in the test. A sensory test was conducted in which the tablets were available for visual and tactile examination.

comprising five diameters (3, 5, 8, 11, and 15 mm) and two thicknesses (2 and 5 mm) per diameter. The designs were realized using a stereolithography 3D printer (Elegoo Mars 2, Elegoo LCD., Shenzhen, China) following the manufacturer's instructions, with Water Washable resin SK02W (Felidentia Capital Ltd., Tokyo, Japan).

### 2.3. Participants and sensory testing with dummy tablets

The recruitment period spanned from June 28th, 2024, to February 6th, 2025. A total of 253 university and graduate students participated in the survey, primarily individuals in their twenties—an age demographic that aligns with most drug overdose patients. Participants were recruited after the study was explained and informed consent was obtained.

Ten dummy tablets, fabricated *via* 3D printing, were individually placed in transparent bags labeled A–J for the sensory test, during which participants were permitted to observe and handle the tablets (Figure 1C, Table 1). The diameter and thickness of the dummy tablets were randomly assigned, and testing was conducted under the surveyor's supervision. Survey responses were collected electronically *via* a web-based questionnaire accessed *via* a QR code (Table 1). Participants received only alphabetic and visual information about the dummy tablets; numerical dimensions, including tablet diameter and thickness, were withheld (Figure 1C).

The sensory test included two main questions. Question 1 (Q1) asked participants: "If you are taking a large number of tablets, please choose the number of tablets that you can take.," with options ranging from 0 to 19, 20 to 39, 40 to 69, 70 to 99, and over 100 tablets (Table 1). Question 2 (Q2) assessed perceived ease of ingestion, stating: "If you are taking a large number of tablets, please rate the ease of swallowing on a 5-point scale (1-5: Difficult - Easy)" (Table 1).

### 2.4. Statistical analysis

All statistical analyses were performed using JMP Student Edition 19 (SAS Institute Inc., Cary, NC, USA), with a significance threshold set at $p < 0.05$. Cutoff values were determined employing the Youden Index method. According to Japan's Ministry of Internal Affairs and Communications, as of April 2025, approximately 23.37 million individuals were in their teens and twenties. Based on this population size, the required sample size for the survey was calculated to be 245 participants, assuming a 5% margin of error, an 80% collection rate, and a 95% confidence interval (CI). This sample-size calculation was described as a descriptive precision estimate rather than as an a priori sample-size determination.

### 2.5. Ethics approval

**Table 1. Sensory test results about Overdose**

| dummy tablets (d, t) | I (3, 2) | F (3, 5) | C (5, 2) | B (5, 5) | A (8, 2) | D (8, 5) | E (11, 2) | H (11, 5) | G (15, 2) | J (15, 5) |
|---|---|---|---|---|---|---|---|---|---|---|
| Q1 *n* (%) | | | | | | | | | | |
| 0–19 Tablets | 8 (3.2) | 10 (4.0) | 8 (3.2) | 33 (13.0) | 86 (34.0) | 126 (49.8) | 131 (51.8) | 182 (71.9) | 190 (75.1) | 223 (88.1) |
| 20–39 Tablets | 12 (4.7) | 28 (11.1) | 45 (17.8) | 79 (31.2) | 101 (40.0) | 79 (31.2) | 85 (33.6) | 49 (19.4) | 42 (16.6) | 19 (7.5) |
| 40–69 Tablets | 31 (12.3) | 59 (23.3) | 67 (26.5) | 84 (33.2) | 35 (13.8) | 30 (11.9) | 22 (8.7) | 14 (5.5) | 11 (4.3) | 5 (2.0) |
| 70–99 Tablets | 33 (13.0) | 54 (21.3) | 57 (22.5) | 32 (12.6) | 11 (4.3) | 12 (4.7) | 9 (3.6) | 4 (1.6) | 3 (1.2) | 2 (0.8) |
| more than 100 tablets | 169 (66.8) | 102 (40.3) | 76 (30.0) | 25 (9.9) | 20 (7.9) | 6 (2.4) | 6 (2.4) | 4 (1.6) | 7 (2.8) | 4 (1.6) |
| Q2 *n* (%) | | | | | | | | | | |
| 1 (difficult to take) | 3 (1.2) | 4 (1.6) | 0 (0) | 5 (2.0) | 8 (3.2) | 40 (15.8) | 66 (26.1) | 141 (55.7) | 168 (66.4) | 233 (92.1) |
| 2 | 4 (1.6) | 6 (2.4) | 5 (2.0) | 13 (5.1) | 49 (19.4) | 111 (43.9) | 122 (48.2) | 88 (34.8) | 61 (24.1) | 11 (4.3) |
| 3 | 12 (4.7) | 13 (5.1) | 15 (5.9) | 42 (16.6) | 70 (27.7) | 76 (30.0) | 46 (18.2) | 17 (6.7) | 17 (6.7) | 3 (1.2) |
| 4 | 14 (5.5) | 48 (19.0) | 50 (19.8) | 114 (45.1) | 91 (36.0) | 21 (8.3) | 14 (5.5) | 4 (1.6) | 3 (1.2) | 2 (0.8) |
| 5 (easy to take) | 220 (87.0) | 182 (71.9) | 183 (72.3) | 79 (31.2) | 35 (13.8) | 5 (2.0) | 5 (2.0) | 3 (1.2) | 4 (1.6) | 4 (1.6) |

Sensory test: About the dummy tablets (you can look and touch). Question 1 (Q1): If you are taking a large number of tablets, please choose the number of tablets that you can take. Question 2 (Q2): If you are taking a large number of tablets, please rate the ease of swallowing on a 5-point scale (1-5: Difficult - Easy). $n$ = 253. The alphabetical order is the order of the exams. Smallest to largest order of dummy tablets. d: diameter (mm), t: thickness (mm).

This study was approved by the Ethics Committee of the Graduate School of Pharmaceutical Sciences, Chiba University (R049-1). Participants received both verbal and written explanations before scanning the QR code. Participation was voluntary and did not affect grades. Consent was obtained as participants indicated their agreement by selecting the consent box on the web-based questionnaire and submitting their responses. All participants were adults in Japan. All methods were carried out in accordance with the Declaration of Helsinki.

## 3. Results and Discussion

### 3.1. Investigation of the diameter and thickness of prescription and OTC drugs

To examine the diameter (d) and thickness (t) of round prescription drug tablets, data were obtained from the Pharmaceutical Interview Form, and correlations were analyzed (Figure 2A). The correlation between prescription drug diameter and thickness was weak ($\rho = 0.26$, 95% CI: 0.20-0.43, $p < 0.05$). The diameter distribution for these tablets predominantly fell within $6 < d \leq 8$ mm, with no examples observed below 4 mm or above 12 mm (Figure 2C). The thickness of round prescription tablets was primarily distributed between 2 and 3 mm, with no measurements below 1 mm or exceeding 5 mm (Figure 2E).

For OTC drugs used for overdoses, the diameter and thickness of round tablets were measured using a digital caliper, and averages were calculated ($n = 4$; Figure 2). Analysis demonstrated a strong correlation between diameter and thickness in round OTC tablets ($\rho = 0.61$, 95% CI: 0.45-0.90, $p < 0.05$; Figure 2B). Most OTC tablet diameters were within the 8–10 mm range, with none smaller than 4 mm or larger than 12 mm (Figure 2D). The most frequent thickness category was > 5 mm

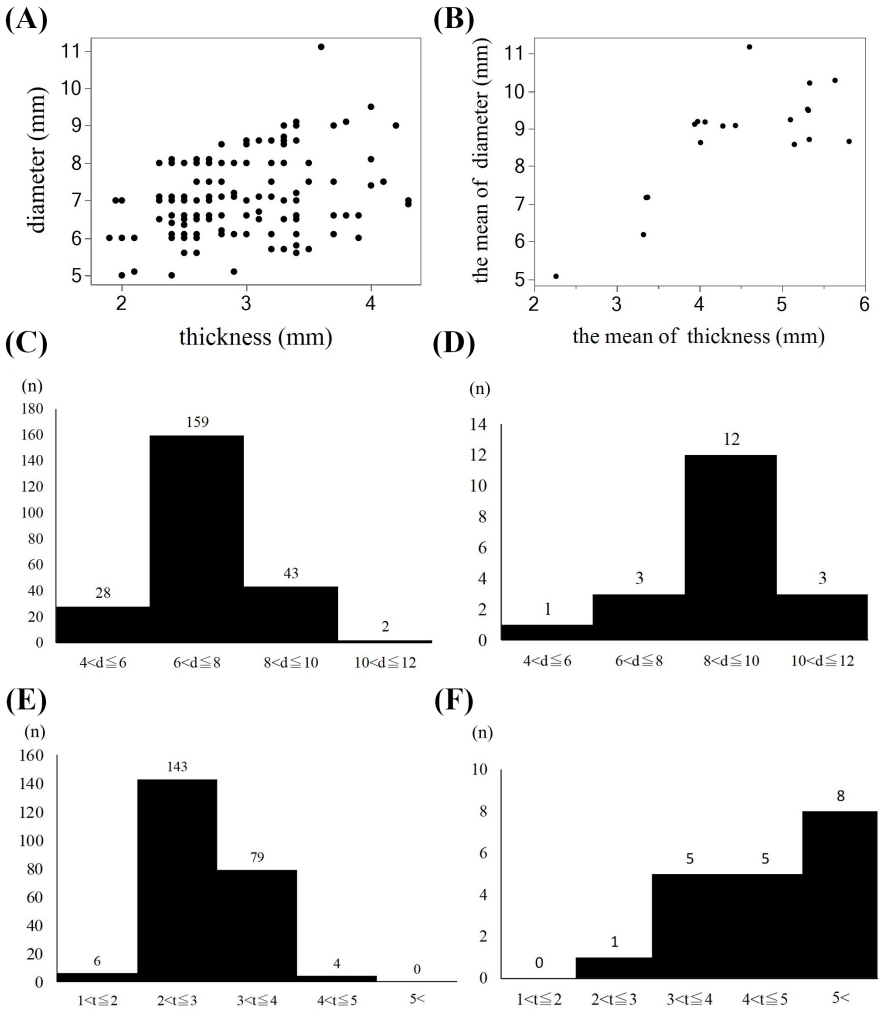


**Figure 2. Diameter and thickness characteristics of prescription and over-the-counter (OTC) tablets.** (A) Correlation between diameter and thickness of pharmaceutical products, $n = 232$, $\rho = 0.26$, 95% CI: 0.20–0.43, $p < 0.05$. (B) Correlation between mean diameter and mean thickness of OTC drugs, $n = 19$, $\rho = 0.61$, 95% CI: 0.45–0.90, $p < 0.05$. (C) Diameter distribution of prescription drugs. (D) Mean diameter distribution of OTC drugs. (E) Distribution of the thickness of prescription drugs. (F) Distribution of average thickness of OTC drugs; d: diameter (mm), t: thickness (mm). The vertical axis of C–F indicates *n*. Spearman's rank correlation coefficient was calculated.

(8/19); none had a thickness less than 2 mm (Figure 2F).

Regarding product trends, OTC drug tablets typically displayed a greater diameter and thickness than prescription drug tablets. Previous studies have reported a mean diameter of 7.6 ± 1.4 mm for 3,271 round prescription drug tablets (*18*). Similarly, the results of the current study indicated that most round OTC drug tablets had diameters within $8 < d \leq 10$ mm, with no tablets under 4 mm or over 12 mm. This trend underscores the observation that OTC drugs are generally larger in size and thickness than their prescription counterparts. Based on these findings, dummy tablets were produced for this study.

### 3.2. Response rate and participant characteristics

The required sample size for this survey was calculated to be 245, and 253 individuals responded, thereby fulfilling the adequacy criteria. With an estimated 300 surveys distributed, the response rate was 84.3% (253/300). The mean age of participants was 21.3 ± 2.1 years; male respondents ($n$ = 111) had a mean age of 21.5 ± 2.6 years, while female respondents ($n$ = 142) had a mean age of 21.1 ± 1.5 years.

### 3.3. Sensory test using dummy tablets

Dummy tablets were manufactured *via* 3D printing to facilitate sensory tests and to investigate appropriate dosage forms—such as diameter and thickness—to mitigate the risk of overdose (Figure 1C). Five different diameters were produced based on actual tablet sizes from prior investigations; extreme reference sizes of 3 mm and 15 mm, not present in surveyed products, were included. Tablets were prepared at thicknesses of 2 mm and 5 mm, resulting in ten variations subjected to sensory testing (Table 1).

Initially, participants were presented with Q1 (Table 1) to consider the maximum number of tablets they could consume when taking a large dose. For the small, 3 mm-diameter dummy tablets—which do not reflect any current medication—the highest proportion of respondents reported being able to take "more than 100 tablets," with 169 respondents (66.8%) for the 2 mm-thick tablets and 102 (40.3%) for the 5 mm-thick tablets. Conversely, among the 15 mm diameter dummy tablets, representing the largest size not found in actual medications, the percentage of respondents reporting the perceived ability to ingest more than 100 tablets was lowest: 7 respondents (2.8%) for the 2 mm thick tablets and 4 respondents (1.6%) for the 5 mm thick tablets. Among the tablets with a 5 mm diameter—the smallest available size—76 respondents (30.0%) were able to ingest more than 100 tablets at a thickness of 2 mm, while 25 respondents (9.9%) could do so at a thickness of 5 mm. For tablets with an 11 mm diameter—the largest available size—6 respondents (2.4%) were able to ingest more than 100 tablets at a thickness of 2 mm, while 4 respondents (1.6%) could do so at a thickness of 5 mm. These findings suggest that increasing tablet thickness (from 2 mm to 5 mm) reduces the ease of consuming large quantities, even when the diameter remains constant.

Subsequently, Q2 was asked to assess the perceived ease of bulk ingestion (Table 1). For the 3 mm-diameter dummy tablets, which are not representative of existing medications, the proportion of respondents who answered "easy to take" was highest: 220 (87.0%) for the 2 mm-thick tablet and 182 (71.9%) for the 5 mm-thick tablet. In contrast, for the larger dummy tablets (15 mm diameter), which were not present in the actual drug sample, only 4 respondents (1.6%) across both thicknesses answered: "easy to take." Regarding the 5 mm diameter tablets—the smallest available as medicine—183 respondents (72.3%) for 2 mm thickness and 79 (31.2%) for 5 mm thickness were rated as "easy to take." For tablets with an 11 mm diameter—the largest available as medicine—only 5 respondents (2.0%) for 2 mm thickness and 3 (1.2%) for 5 mm thickness reported they were "easy to take."

### 3.4. Tablet form (diameter and thickness) associated with reduced overdose risk

Based on the data obtained from the sensory tests, an evaluation was conducted to determine which tablet diameter and thickness were most likely to impede overdose (Table 1). The dummy tablets for which the highest proportion of respondents selected the lowest response category ("0–19 tablets") for "Q1. If you are taking a large number of tablets, please choose the number of tablets that you can take." had a diameter of 8 mm and a thickness of 5 mm (Tablet D; 126 respondents, 49.8%). Similarly, Tablets E, H, G, and J, which possess larger diameters and thicknesses than Tablet D, also received "0–19 tablets" as the most frequent answer to this question. Notably, for Tablet H (diameter: 11 mm; thickness: 5 mm), 71.9% of respondents selected the minimum category (0–19 tablets) when asked Q1. Additionally, tablets with a 15-mm diameter may further complicate the administration of large doses (Table 1).

### 3.5. Threshold for "diameter + thickness" and "volume" of tablets that are difficult to overdose

First, a generalized linear mixed model was constructed to control for within-participant correlation due to repeated measures. Receiver operating characteristic (ROC) analysis was employed to identify cutoff values for both "diameter + thickness" and "volume" to determine tablet formulations that are difficult to overdose (Table 1, Figure 3). Specifically, the threshold for "diameter + thickness" was verified using the ease-of-taking scores obtained from the sensory test, with a threshold set at ≤ 2 on a 5-point scale. The ROC analysis

revealed a cutoff value of 13, with an area under the curve (AUC) of 0.93, a 95% CI of 0.91–0.93, sensitivity of 0.91, and specificity of 0.84 ($p<0.05$).

Similarly, the cutoff value for tablet "volume" was determined using the same sensory test metric (≤ 2 on a 5-point scale). ROC analysis revealed a cutoff of 190 $mm^3$, with an AUC of 0.92 (95% CI: 0.91–0.93), sensitivity of 0.91, and specificity of 0.84 ($p<0.05$). The volume was calculated by treating each tablet as a cylinder.

Overdose of dextromethorphan (*19*) or diphenhydramine (*16*) can have profound effects. In Japan, MEDICON® (dextromethorphan) and RESTAMIN® (diphenhydramine) tablets are comparatively small, measuring 5–6 mm in diameter and 2–3 mm in thickness, and are available both by prescription and OTC. Dextromethorphan exhibits varying pharmacological effects based on the overdose amount; at high doses, it acts as an NMDA (N-methyl-D-aspartate) receptor antagonist, inducing hallucinations and dissociative symptoms *(20,21)*. Co-administration with CYP2D6 inhibitors, such as quinidine, sertraline, and diphenhydramine, can increase circulating dextromethorphan concentrations. There are also documented fatalities resulting from high-dose dextromethorphan ingestion alone (*19*). Diphenhydramine overdose can also produce severe cardiac effects, including cardiac arrest (*22*), for which no effective antidote exists. In the current study, these medications corresponded to Tablet C in the dummy tablet set. Notably, 76 participants (30.0%) selected "more than 100 tablets" as potentially ingestible at one time, while 183 (72.3%) rated the ease of taking large quantities at the maximum score of 5.

Regarding product size for future safety considerations, Tablet D (diameter: 8 mm; thickness: 5 mm) demonstrated the highest proportion of respondents (126, 49.8%) selecting the lowest value of "0–19 tablets" as the answer of Q1. This finding aligns with the ROC curve cutoff value for "diameter + thickness" of 13. Thus, Tablets D, E, H, G, and J—with larger dimensions—appear to impede excessive ingestion.

Accordingly, it is essential to optimize tablet size and thickness for medications with high overdose risk, balancing these modifications against normal patient use requirements. For safe drug formulations, prioritizing ease of administration may warrant maintaining a smaller tablet size, whereas larger tablets may be preferable for compounds with high toxicity in overdose situations. Furthermore, the results demonstrate that increasing thickness (5 mm *vs.* 2 mm) further reduces the likelihood of ingesting large doses, even when the diameter remains constant—a factor warranting consideration in pharmaceutical design.

This study has certain limitations. The findings rely on sensory testing with dummy tablets, as testing large quantities of actual tablets was not feasible. Consequently, verification was only conducted through sensory testing. Additionally, the participant group comprised solely young individuals due to the high rate of overdose reports in this demographic; thus, the findings may not apply to older adults. Moreover, although different tablet shapes can influence the results, this study considered only one shape. Hence, future investigations should examine the impact of various tablet shapes on overdose, including studies that compare pharmacokinetics across different tablet shapes. Larger tablets may increase swallowing difficulty, esophageal

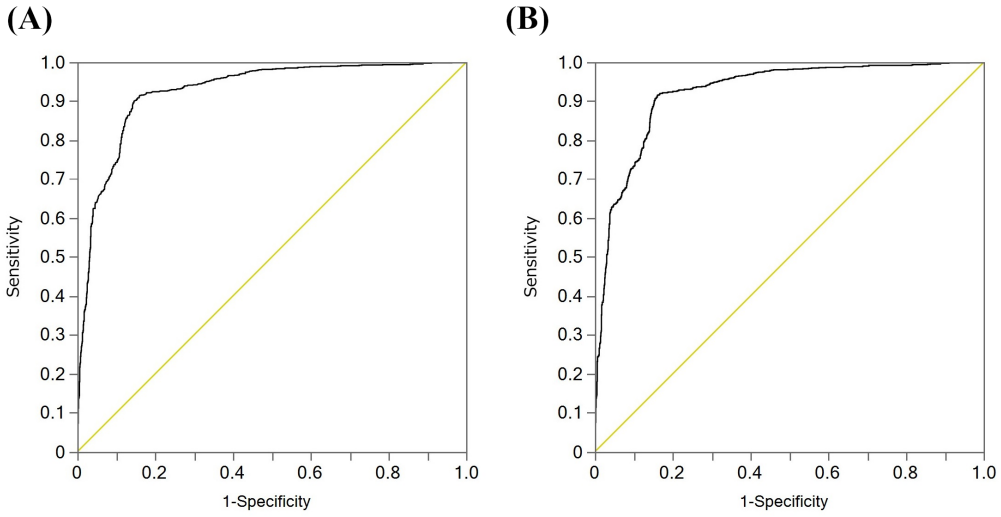


**Figure 3. ROC curves for determining cutoff values of "diameter + thickness" and "volume" parameters for tablets that are difficult to ingest in large quantities.** First, a generalized linear mixed model was constructed to control for within-participant correlation due to repeated measures. (A) ROC curve identifying the cutoff value of "diameter + thickness" for tablets with ingestion difficulty in large quantities. ROC analysis revealed a cutoff of 13 (AUC: 0.93, 95% CI: 0.91–0.93, sensitivity: 0.91, specificity: 0.84, $p < 0.05$). (B) ROC curve for determining the "volume" cutoff value in assessing tablet ingestion difficulty in large quantities. ROC analysis revealed a cutoff of 190 (AUC: 0.92, 95% CI: 0.91–0.93, sensitivity: 0.91, specificity: 0.84, $p < 0.05$).

sticking, choking, and poor medication adherence during normal use. It should also address adherence during daily treatment, risks to older adults, children, and patients with dysphagia, and the possibility that an individual may still complete an overdose by swallowing the tablets one at a time. Other overdose-prevention measures, including limiting package quantities, dispensing smaller supplies at shorter intervals, supervised medication administration, and restrictions on sales, should be discussed and compared with the tablet-size strategy. The size of the tablet should only be considered as one possible solution. This study included only a convenience sample of undergraduate and graduate students, without reporting their mental health status, history of self-harm or drug overdose, swallowing difficulties, or routine medication experience. Visual and tactile judgments made by healthy students cannot be considered a substitute for the actual behavior of patients at high risk of overdose. These precautions are necessary when generalizing research findings.

The findings of this study suggest that pharmacists can select and dispense formulations containing the same active ingredient, but designed to reduce the risk of overdose, for patients identified as a risk for overdosing, considering their dosage size. Furthermore, pharmaceutical manufacturers can now consider tablet sizes that minimize the potential for overdose on drugs commonly involved in such incidents or possessing high overdose risks, while maintaining ease of swallowing for most patients. These observations may inform the development of effective strategies for overdose prevention.

**Acknowledgements**

We would like to thank Editage for English language editing.

*Funding*: This work was supported by JSPS KAKENHI Grant Number 25K20535 (for KN) and Grant of OTC self-medication promotion foundation Number 41-2-13 (for KN).

*Conflict of Interest*: The authors have no conflicts of interest to disclose.

**References**

1. Pfeifer P, Greusing S, Kupferschmidt H, Bartsch C, Reisch T. A comprehensive analysis of attempted and fatal suicide cases involving frequently used psychotropic medications. Gen Hosp Psychiatry. 2020; 63:16-20.
2. Shoib S, Patel V, Khan S, Armiya'u AY, Saeed F, Swed S, Das S, Chandradasa M. Over-the-counter drug use in suicidal/self-harm behavior: Scoping review. Health Sci Rep. 2022; 5:e662.
3. Wright J, Bond C, Robertson HD, Matheson C. Changes in over-the-counter drug misuse over 20 years: perceptions from Scottish pharmacists. J Public Health (Oxf). 2016; 38:793-799.
4. Finkelstein Y, Macdonald EM, Hollands S, Sivilotti ML, Hutson JR, Mamdani MM, Koren G, Juurlink DN, Canadian Drug Safety and Effectiveness Research Network (CDSERN). Repetition of intentional drug overdose: a population-based study. Clin Toxicol (Phila). 2016; 54:585–589.
5. Finkelstein Y, Macdonald EM, Hollands S, Sivilotti ML, Hutson JR, Mamdani MM, Koren G, Juurlink DN, Canadian Drug Safety and Effectiveness Research Network (CDSERN). Risk of suicide following deliberate self-poisoning. JAMA Psychiatry. 2015; 72:570-575.
6. Zhang Y, Yu B, Wang N, Li T. Acute poisoning in Shenyang, China: a retrospective and descriptive study from 2012 to 2016. BMJ Open. 2018; 8:e021881.
7. Nagashima K, Hiruma K, Nakamura E, Watanabe M, Sekine Y. Identification of factors necessary for gatekeeper of overdose. Biol Pharm Bull. 2024; 47:112-119.
8. Murphy AL, Ataya R, Himmelman D, O'Reilly C, Rosen A, Salvador-Carulla L, Martin-Misener R, Burge F, Kutcher S, Gardner DM. Community pharmacists' Experiences and people at risk of suicide in Canada and Australia: A thematic analysis. Soc Psychiatry Psychiatr Epidemiol. 2018; 53:1173-1184.
9. Hawgood J, Koo YW, Sveticic J, De Leo D, Kolves K. Wesley lifeforce suicide prevention gatekeeper training in Australia: 6 month follow-up evaluation of full and half day community programs. Front Psychiatry. 2020; 11:614191.
10. Kabeya K, Satoh H, Hori S, Sawada Y. Experimental study on patient preferences regarding the shape and size of medical tablets and capsules using three-dimensionally printed plastic model formulations. Patient Prefer Adherence. 2021; 15:863-870.
11. Asano M, Imai S, Shimizu Y, Kizaki H, Ito Y, Tsuchiya M, Kuriyama R, Yoshida N, Shimada M, Sando T, Ishijima T, Hori S. Factor Analysis of Patients Who Find Tablets or Capsules Difficult to Swallow Due to Their Large Size: Using the Personal Health Record Infrastructure of Electronic Medication Notebooks. J Med Internet Res. 2024: 26:e54645.
12. Sugiyama S, Iida T, Morimoto Y, Yamazaki Y, Mikuzuki L, Hayashi M. Effects of Tablet Size and Head Posture on Drug Swallowing: A Preliminary Examination Using Endoscopy in Healthy Subjects. Acta Med Okayama. 2021; 75:495-503.
13. Yamamoto S, Taniguchi H, Hayashi H, Hori K, Tsujimura T, Nakamura Y, Sato H, Inoue M. How do tablet properties influence swallowing behaviours? J Pharm Pharmacol. 2014; 66:32-39.
14. Kamijo Y, Takai M, Fujita Y, Usui K. A Retrospective Study on the Epidemiological and Clinical Features of Emergency Patients with Large or Massive Consumption of Caffeinated Supplements or Energy Drinks in Japan. Intern Med. 2018; 57:2141-2146.
15. Kerrigan S, Lindsey T. Fatal caffeine overdose: two case reports. Forensic Sci Int. 2005; 153:67-69.
16. Nemanich A, Liebelt E, Sabbatini AK. Increased rates of diphenhydramine overdose, abuse, and misuse in the United States, 2005–2016. Clin Toxicol (Phila). 2021; 59:1002-1008.
17. Kamijo Y, Kyan R, Kohara S, Takai M, Hanazawa T, Yoshizawa T, Miyamoto M. Survey on drug-related poisoning cases in emergency medical care: Focus on

over-the-counter drugs. the FY2022 Ministry of Health, Labor, and Welfare Administrative Promotion Research Project Subsidy (Pharmaceutical and Medical Device Regulatory Science Policy Research Project) Participating Research Report (2022) *https://mhlw-grants.niph.go.jp/system/files/report_pdf/202225030A-buntan3.pdf* (accessed 26 February 2026).
18. Oshima T, Hori S, Maida C, Miyamoto E. Survey on the Size and Shape of Tablets and Capsules. Pharm Tech Japan. 2006; 22.2:253-257.
19. Hasuwa K, Inoue N, Tamura S, Terazawa I, Yuui K, Kudo R, Kasuda S. An autopsy case of a young man with a single overdose of dextromethorphan. Leg Med (Tokyo). 2024; 70:102470.
20. Logan BK, Goldfogel G, Hamilton R and Kuhlman J. Five deaths resulting from abuse of dextromethorphan sold over the internet. J Anal Toxicol. 2009; 33:99-103.
21. Brown GR, McLaughlin K, Vaughn K. Identifying and treating patients with synthetic psychoactive drug intoxication. JAAPA. 2018; 31:1-5.
22. Nishino T, Wakai S, Aoki H, Inokuchi S. Cardiac arrest caused by diphenhydramine overdose. Acute Med Surg. 2018; 5:380-383.

Received May 27, 2026; Revised July 31, 2026; Accepted August 13, 2026.

**Address correspondence to:*
Kazuki Nagashima, Laboratory of Practical Pharmacy, Graduate School and Faculty of Pharmaceutical Sciences, Chiba University; 1-8-1 Inohana, Chuo-ku, Chiba-shi, Chiba 260-8675, Japan.
E-mail: knagashima@chiba-u.jp

Released online in J-STAGE as advance publication August 18, 2026.

***Brief Report***

DOI: 10.5582/ddt.2026.01040

# Disproportionality analysis of opioid-related urinary retention using the JADER database: Focus on the lack of signal for transdermal fentanyl

**Yusuke Tanaka[1,2], Masahiko Kimura[1,2], Naohito Ide[2], Ken-ichi Sako[2], Tomoji Maeda[2,*]**

[1] Department of Pharmacy, Jichi Medical University Saitama Medical Center, Saitama, Japan;
[2] Department of Clinical Pharmacy, Nihon Pharmaceutical University, Saitama, Japan.

**SUMMARY**: Urinary retention is a known adverse effect of opioids, but limited information is available on how this adverse event varies among individual opioids. This study evaluated disproportionality signals between major opioids and urinary retention using the Japanese Adverse Drug Event Report database (JADER). We performed a disproportionality analysis of reports submitted between April 2004 and October 2025. Signals were assessed using reporting odds ratios (RORs), 95% confidence intervals (CIs), and the Information Component (IC). Adverse events were identified using the Medical Dictionary for Regulatory Activities/Japanese version (MedDRA/J) term "urinary retention." A sensitivity analysis was conducted using a broader definition of urinary dysfunction that also included "Dysuria." Time to onset was calculated from the start of opioid administration to event onset, and daily doses were converted to oral morphine equivalents. Significant signals were detected for morphine, oxycodone, tramadol, and codeine. Transdermal fentanyl was the only opioid without a detectable signal, even under the broader definition of urinary dysfunction. Among opioids with detected signals and available dose information, urinary retention was reported even at relatively low morphine-equivalent doses, suggesting the need for careful monitoring at the start of opioid therapy. The absence of a signal for transdermal fentanyl may reflect a lower reporting frequency in JADER, but not a lower clinical risk, of urinary retention. Given the limitations of spontaneous reporting systems, these findings are hypothesis-generating and are insufficient to guide opioid selection or switching.

***Keywords***: Adverse drug reaction, reporting odds ratio, signal detection, spontaneous reporting system

## 1. Introduction

Urinary retention is a recognized adverse drug event (ADE) associated with opioid use, but drug-specific information remains limited. Despite its clinical importance, reports on this condition remain limited, and current guidelines provide only general management strategies, offering little guidance on opioid selection from the perspective of urinary adverse events (*1*). We encountered a patient who developed urinary retention after initiating oral morphine therapy and subsequently showed improvement following a switch to a fentanyl patch (*2*). Although this single case cannot establish differences in clinical risk among opioids, it raised a clinical question as to whether urinary retention is reported differently among individual opioids in a spontaneous reporting database. However, although urinary retention has been included among opioid-related adverse events in previous JADER studies, detailed assessments of urinary retention reporting patterns across individual opioids remain limited. In addition, the rarity of this ADE makes conventional epidemiological studies difficult.

The Japanese Adverse Drug Event Reporting Database (JADER), maintained by the Pharmaceuticals and Medical Devices Agency (PMDA), is a large-scale spontaneous reporting system that collects adverse event reports from clinical practice in Japan. It has been widely used to evaluate drug safety signals, particularly for rare ADEs, using measures such as the reporting odds ratio (ROR) (*3-5*).

This study aimed to evaluate disproportionality signals for urinary retention associated with major opioids in JADER. These findings are intended to provide hypothesis-generating information for further evaluation and clinical monitoring, rather than to guide opioid selection.

## 2. Materials and Methods

### 2.1. Data source

This study included cases registered in the JADER between April 2004 and October 2025. The database was obtained from the Pharmaceuticals and Medical Devices Agency (PMDA) website. (*https://www.pmda.go.jp/safety/info-services/drugs/adr-info/suspected-adr/0003.html*).

JADER consists of four data tables: DEMO, DRUG, REAC, and HIST. Duplicate entries were identified and removed using the case identification numbers in the DEMO table. The DEMO, DRUG, and REAC tables were then linked using these identification numbers, and the analysis was conducted on the merged dataset. For each case, the contribution of administered drugs to adverse drug events (ADEs) was classified into three categories: "suspected drug," "concomitant medication," and "interaction." Only drugs classified as "suspected drug" were included in the analysis.

The DEMO table includes patient characteristics such as sex and age. In sex-specific analyses, cases with missing or unknown sex were excluded. Age was categorized into younger (< 60 years) and older (≥ 60 years) groups; records with ambiguous age categories were excluded.

### 2.2. Drugs included in the analysis

The drugs included in this analysis were morphine, fentanyl, oxycodone, hydromorphone, tramadol, and codeine phosphate hydrate. To minimize the influence of postoperative urinary retention, administration routes with a higher associated risk were excluded. Accordingly, fentanyl was limited to transdermal patch formulations, whereas the other opioids were restricted to oral formulations.

### 2.3. Extraction of adverse events

Adverse events were identified using the MedDRA/J (Medical Dictionary for Regulatory Activities, Japanese version; version 28.1) preferred term "urinary retention" (PT: 10046555). In addition, a sensitivity analysis was conducted to allow a broader assessment of urinary dysfunction by including the preferred term "Dysuria" (PT: 10013990).

### 2.4. Time to onset

For the time-to-onset analysis, cases with unknown start dates of drug administration or unknown dates of adverse event onset were excluded. Cases in which only the year was recorded, or in which the day was missing despite the availability of the month and year, were also excluded. Time to onset was defined as the interval from the start of drug administration to the onset of the adverse event, with 1 day added to the calculated duration.

### 2.5. Daily dose

For the daily dose analysis, cases with unknown dose information were excluded. The doses of opioids were converted to oral morphine equivalents. Specifically, 20 mg/day of oral oxycodone, 0.3 mg/day of transdermal fentanyl, 150 mg/day of oral tramadol, and 200 mg/day of oral codeine were considered equivalent to 30 mg/day of oral morphine (*6,7*).

### 2.6. Statistical analysis

The reporting odds ratio (ROR) and corresponding 95% confidence interval (CI) were calculated as measures of association. A signal was considered present when the lower limit of the 95% CI exceeded 1.

The ROR was calculated based on a two-by-two contingency table, defined as follows: a, cases with the target ADE associated with the suspected drug; b, non-cases associated with the suspected drug; c, cases with the target ADE associated with other drugs; and d, non-cases associated with other drugs. The ROR was calculated as (a×d) / (b×c). The RORs and corresponding 95% CIs were calculated using unrounded values.

Because no zero cells were present in the contingency table, no continuity correction was applied, and the ROR was calculated without adjustment. Drug definitions, including routes of administration, were kept consistent between the ROR and IC analyses.

In the primary analysis, the information component (IC), a Bayesian disproportionality measure, was calculated to assess the robustness of the signals. A signal was considered present when the lower limit of the 95% credibility interval of the IC ($IC_{025}$) exceeded 0. The IC was calculated using the Bayesian confidence propagation neural network method, and $IC_{025}$ was defined as the lower limit of the 95% credibility interval of the IC.

For the analysis of time to ADE onset, the number of reports was limited; therefore, Weibull distribution analysis was not performed, and the median time to onset was calculated instead. All statistical analyses were performed using JMP® Student Edition 19.0.5.

### 2.7. Ethical considerations

Ethical approval was not required for this study because it was based on a secondary analysis of anonymized data from a publicly available database. The JADER database contains no personally identifiable patient information; therefore, informed consent was not applicable. In addition, the Ethics Committee of Nihon Pharmaceutical University determined that ethical review was not required for this study.

## 3. Results and Discussion

### 3.1. Patient characteristics

A comparison between all urinary retention reports (*n*

= 5,011) and reports in which opioids were reported as suspected drugs ($n$ = 150) is shown in Table 1. Female patients accounted for 31.6% of all urinary retention reports and 45.3% of opioid-related urinary retention reports. Because tramadol accounted for a large proportion of the opioid-related reports, an additional descriptive analysis was conducted in a subgroup of strong opioids, excluding tramadol and codeine. In this subgroup, female patients accounted for 46.3% (19/41), showing a similar pattern.

Older adults aged ≥ 60 years accounted for 63.5% of all urinary retention reports and 71.3% of opioid-related urinary retention reports. These findings suggest that older adults represented a large proportion of urinary retention reports regardless of opioid involvement. However, because potential confounding factors could not be fully evaluated in JADER, these descriptive findings should be interpreted with caution.

### 3.2. Disproportionality analysis by drug

Based on these patient characteristics, disproportionality analyses were performed for each opioid. In the primary analysis, ROR-based signals for urinary retention were detected for morphine, oxycodone, tramadol, and codeine, whereas no ROR-based signal was detected for transdermal fentanyl or hydromorphone (Table 2). The IC analysis showed consistent results, with $IC_{025}$ values exceeding 0 for morphine (0.10), oxycodone (0.01), tramadol (2.42), and codeine (1.10), but not for transdermal fentanyl (−1.14) or hydromorphone (−0.85).

The sensitivity analysis using a broader definition that included urinary retention and dysuria is presented in Table 3. ROR-based signals were detected for all target opioids except transdermal fentanyl. Thus, no disproportionality signal for transdermal fentanyl was detected in either the primary or sensitivity analysis. These findings should be considered hypothesis-generating and require further validation in clinical studies with detailed patient-level information.

### 3.3. Interpretation of the findings for transdermal fentanyl

Among the opioids examined, no disproportionality signal was detected for transdermal fentanyl. This finding should be interpreted cautiously and should not be taken as evidence of no association or a lower clinical risk of urinary retention. Several pharmacological and clinical observations may be relevant to urinary dysfunction. Opioid-induced urinary retention has been attributed to μ-receptor-mediated inhibition of bladder sensory input and the micturition reflex, as well as increased bladder outlet resistance (*8*). In previous non-JADER studies, intrathecal fentanyl produced milder and shorter bladder relaxation than intrathecal morphine in dogs, and urinary retention was reported less frequently with fentanyl

**Table 1. Characteristics of all urinary retention reports and opioid-related urinary retention reports in the JADER database**

| Factor<br>*n* | Total UR Reports<br>(*n* = 5,011) | Opioid-related UR<br>(*n* = 150) | Morphine<br>(*n* = 11) | Fentanyl<br>(*n* = 16) | Oxycodone<br>(*n* = 12) | Hydromorphone<br>(*n* = 2) | Tramadol<br>(*n* = 98) | Codeine<br>(*n* = 11) |
|---|---|---|---|---|---|---|---|---|
| Sex, *n* (%) | | | | | | | | |
| Male | 3,171 (63.3) | 80 (53.3) | 6 (54.5) | 11 (68.8) | 4 (33.3) | 1 (50) | 52 (53.1) | 6 (54.5) |
| Female | 1,581 (31.6) | 68 (45.3) | 5 (45.5) | 5 (31.3) | 8 (66.7) | 1 (50) | 46 (46.9) | 3 (27.3) |
| Unknown | 259 (5.2) | 2 (1.3) | 0 (0) | 0 (0) | 0 (0) | 0 (0) | 0 (0) | 2 (18.2) |
| Age group, *n* (%) | | | | | | | | |
| Older adults (≥ 60 years) | 3,181 (63.5) | 107 (71.3) | 5 (45.5) | 11 (68.8) | 11 (91.7) | 0 (0) | 76 (77.6) | 4 (36.4) |
| Non-elderly (< 60 years) | 732 (14.6) | 26 (17.3) | 2 (18.2) | 3 (18.8) | 1 (8.3) | 1 (50) | 14 (14.3) | 5 (45.5) |
| Unknown | 1,098 (21.9) | 17 (11.3) | 4 (36.4) | 2 (12.5) | 0 (0) | 1 (50) | 9 (9.2) | 2 (18.2) |

Abbreviations: JADER, Japanese Adverse Drug Event Report database; UR, urinary retention. Note: Data are presented as *n* (%). Opioid-related UR was defined as UR reports in which a target opioid was reported as a suspected drug. Fentanyl refers to transdermal fentanyl.

**Table 2. Disproportionality analysis of urinary retention signals associated with individual opioids in the JADER database**

| Drug | Suspected drug | | Other drugs | | ROR | 95% CI | IC | $IC_{025}$ |
|---|---|---|---|---|---|---|---|---|
| | a (cases) | b (non-cases) | c (cases) | d (non-cases) | | | | |
| Morphine | 11 | 1077 | 5000 | 986660 | 2.02 | 1.11–3.65 | 0.94 | 0.10 |
| Fentanyl | 16 | 4324 | 4995 | 983413 | 0.73 | 0.45–1.19 | -0.44 | -1.14 |
| Oxycodone | 12 | 1300 | 4999 | 986437 | 1.82 | 1.03–3.22 | 0.81 | 0.01 |
| Hydromorphone | 2 | 154 | 5009 | 987583 | 2.56 | 0.63–10.33 | 0.96 | -0.85 |
| Tramadol | 98 | 2786 | 4913 | 984951 | 7.05 | 5.75–8.64 | 2.71 | 2.42 |
| Codeine | 11 | 480 | 5000 | 987257 | 4.53 | 2.49–8.25 | 1.95 | 1.10 |

Abbreviations: CI, confidence interval; IC, information component; $IC_{025}$, lower limit of the 95% credibility interval; ROR, reporting odds ratio. Note: Data are presented as a two-by-two contingency table (a, b, c, and d), ROR with 95% CI, and IC values. The definitions of a, b, c, and d are as follows: a, cases with the target adverse event associated with the suspected drug; b, non-cases associated with the suspected drug; c, cases with the target adverse event associated with other drugs; d, non-cases associated with other drugs. A signal based on the ROR was considered present when the lower limit of the 95% CI exceeded 1. A signal based on the IC was considered present when $IC_{025}$ exceeded 0. Fentanyl refers to transdermal fentanyl.

than with morphine in patients receiving intravenous patient-controlled analgesia (IV-PCA) after gastrectomy (*9,10*). However, differences in route of administration, study population, and outcome definitions limit direct comparison with the present analysis.

### 3.4. Interpretation of signals for other opioids

Another notable finding was the relatively high number of reports associated with tramadol. One possible explanation is its mechanism of action. In addition to its effects on opioid receptors, tramadol inhibits the reuptake of norepinephrine and serotonin (*11*), which may influence urinary function. Similar effects have been reported for antidepressants with comparable mechanisms (*5*). Increased norepinephrine activity may promote urethral sphincter contraction, thereby increasing the risk of urinary retention.

In addition, tramadol is not classified as a narcotic in Japan and is more widely prescribed than other opioids. It is commonly used for conditions prevalent in older adults, such as osteoarthritis and chronic non-cancer pain. These patients are more likely to have comorbidities such as benign prostatic hyperplasia, as well as age-related decline in renal function. These factors may have contributed to the higher number of reported cases.

For oxycodone, a significant signal was detected. A randomized controlled trial comparing intravenous morphine and oxycodone for postoperative pain management reported similar rates of opioid-related adverse events, including urinary retention (*12*), which is consistent with the present findings. However, the confidence interval in this study was close to 1, indicating marginal significance.

Codeine showed a significant signal in the primary analysis, whereas hydromorphone showed a signal only in the sensitivity analysis. Because the number of reports for these drugs was small, the precision of these estimates may be limited, and these findings should be interpreted with caution.

### 3.5. Time to onset and daily dose

To further characterize opioid-related urinary retention reports, we evaluated the time to onset and daily dose at the time of event onset. Morphine, oxycodone, and tramadol were included because ROR-based signals were detected and at least 10 events were reported, whereas transdermal fentanyl was included for descriptive purposes despite the absence of a disproportionality signal (Table 4). Fentanyl dose data were not interpreted as evidence of a dose-related association with urinary retention.

Among opioids with detected signals and available dose information, the mean morphine-equivalent daily doses at onset were 35.0 mg/day for morphine, 33.2 mg/day for oxycodone, and 16.2 mg/day for tramadol. These

**Table 3. Sensitivity analysis of urinary retention and dysuria signals for individual opioids in the JADER database**

| Drug | Suspected drug | | Other drugs | | ROR | 95% CI |
|---|---|---|---|---|---|---|
| | a (cases) | b (non-cases) | c (cases) | d (non-cases) | | |
| Morphine | 12 | 1076 | 5691 | 985969 | 1.93 | 1.09–3.42 |
| Fentanyl | 18 | 4322 | 5685 | 982723 | 0.72 | 0.45–1.14 |
| Oxycodone | 16 | 1296 | 5687 | 985749 | 2.14 | 1.31–3.51 |
| Hydromorphone | 5 | 151 | 5698 | 986894 | 5.74 | 2.35–13.98 |
| Tramadol | 111 | 2773 | 5592 | 984272 | 7.05 | 5.82–8.53 |
| Codeine | 11 | 480 | 5692 | 986565 | 3.97 | 2.18–7.22 |

Note: Cases were reports with urinary retention or dysuria. The definitions of a, b, c, and d are the same as described in Table 2. Fentanyl refers to transdermal fentanyl.

**Table 4. Time to onset and daily dose at the onset of urinary retention associated with individual opioids**

| Opioid | n for onset | Time to Onset, days, median[mean] | n for dose | Dose at onset, mean OME mg/day |
|---|---|---|---|---|
| Morphine | 8 | 1.5 [3.5] | 7 | 35.0 |
| Oxycodone | 9 | 37.0 [34.6] | 5 | 33.2 |
| Fentanyl | 10 | 4.0 [48.6] | 7 | 81.6 |
| Tramadol | 43 | 7.0 [48.8] | 56 | 16.2 |

Note: Time to onset was calculated from the start of opioid administration to the onset of urinary retention. OME, oral morphine equivalents. Cases with missing or incomplete date or dose information were excluded. Fentanyl refers to transdermal fentanyl.

descriptive findings suggest that urinary retention may be reported even at relatively low morphine-equivalent doses. However, because the number of available cases was limited and dose information was incomplete, these results should be interpreted with caution.

### 3.6. Limitations

This study has several limitations inherent to analyses based on spontaneous reporting systems. First, because JADER relies on spontaneous reports, it is subject to various reporting biases, including underreporting, overreporting, missing data, channeling bias, and event-competition or masking bias. Transdermal fentanyl may have been preferentially used in patients with specific clinical backgrounds, and its large number of total reports may have diluted the ROR for urinary retention because the ROR denominator includes non-target adverse events. Therefore, the lack of a signal for transdermal fentanyl should not be interpreted as evidence of a lower clinical risk. In addition, because the total number of patients exposed to each drug is unknown, the true incidence of adverse events cannot be determined.

Second, there are limitations related to data quality. In JADER, detailed information on patients' medical history and concomitant medications is often incomplete. Urinary retention, in particular, can be influenced by factors other than the drug itself, such as cancer stage, underlying conditions including benign prostatic hyperplasia, and concomitant use of medications with anticholinergic effects. These potential confounding factors could not be fully controlled for in the present analysis. Furthermore, comparisons among individual opioids should be interpreted cautiously because differences in drug characteristics, routes of administration, indications, and patient backgrounds may have influenced the observed reporting patterns. Therefore, the observed disproportionality signals do not necessarily represent differences in the intrinsic risk of urinary retention between opioids.

Third, caution is required in interpreting the statistical measures. The ROR is an indicator of disproportionality and does not directly reflect causal relationships or absolute risk. Therefore, the findings of this study should be interpreted as hypothesis-generating rather than confirmatory. Further validation through prospective studies with more detailed clinical information is warranted.

### 3.7. Conclusion

This hypothesis-generating study evaluated disproportionality signals for urinary retention among individual opioids using the JADER database. Transdermal fentanyl was the only opioid for which no signal was detected, even when a broader definition including dysuria was applied. In contrast, disproportionality signals were detected for morphine, oxycodone, tramadol, and codeine. Urinary retention was reported early after treatment initiation for some opioids and at relatively low morphine-equivalent doses in cases with available dose information, highlighting the need for careful monitoring during opioid therapy.

The absence of a disproportionality signal for transdermal fentanyl may reflect a lower reporting frequency in JADER, but it does not indicate a lower clinical risk of urinary retention. Given the limitations of spontaneous reporting systems and the potential

for channeling bias and event-competition bias, these findings should be regarded as hypothesis-generating and should not be used alone to guide opioid selection or switching. Prospective comparative studies with denominator data on drug exposure are required before any clinical recommendation can be made.

**Acknowledgements**

The authors thank all individuals who contributed to the data collection and management of the JADER database. The authors used an AI-based language editing tool to improve the English writing of this manuscript and take full responsibility for its content.

*Funding*: None.

*Conflict of Interest*: The authors have no conflicts of interest to disclose.

**References**

1. National Comprehensive Cancer Network. NCCN Clinical Practice Guidelines in Oncology (NCCN Guidelines®): Adult Cancer Pain. Version 1.2024. Available from: *https://www.nccn.org/guidelines/category_1* (accessed March 23, 2026)
2. Tanaka Y. A case of urinary retention following oral morphine administration successfully treated by switching to a fentanyl patch. J Jpn Soc Pharm Oncol. 2025; 42:1-11. (in Japanese)
3. Sugawara H, Uchida M, Suzuki S, Suga Y, Uesawa Y, Nakagawa T, Takase H. Analyses of respiratory depression associated with opioids in cancer patients based on the Japanese Adverse Drug Event Report database. Biol Pharm Bull. 2019; 42:1185-1191.
4. Omoto T, Asaka J, Sakai T, Sato F, Goto N, Kudo K. Disproportionality analysis of safety signals for a wide variety of opioid-related adverse events in elderly patients using the Japanese Adverse Drug Event Report (JADER) database. Biol Pharm Bull. 2021; 44:627-634.
5. Uekusa S, Mogi K, Ota Y, Hanai Y, Kitagawa K, Yoshio T, Matsuo K. A pharmacovigilance study on psychotropic agent-induced urinary retention using the Japanese Adverse Drug Event Report database. Drugs Real World Outcomes. 2024; 11:691-700.
6. Caraceni A, Hanks G, Kaasa S, *et al*. Use of opioid analgesics in the treatment of cancer pain: evidence-based recommendations from the EAPC. Lancet Oncol. 2012; 13:e58-e68.
7. Japanese Society for Palliative Medicine. Clinical guidelines for pharmacological management of cancer pain, 2020 edition. Tokyo: Kanehara & Co., Ltd.; 2020. p.59.
8. Dobrek L. Lower urinary tract disorders as adverse drug reactions: A literature review. Pharmaceuticals (Basel). 2023; 16:1031.
9. El-Bindary EM, Bakry HH. Urodynamic changes following intrathecal administration of morphine and fentanyl in dogs. East Mediterr Health J. 2001; 7:189-196.
10. Bang EG, Kim SO, Hong JG. Comparison of intravenous patient-controlled analgesia with morphine and fentanyl in gastrectomy patients. Anesth Pain Med. 2008; 3:94-98.
11. Grond S, Sablotzki A. Clinical pharmacology of tramadol. Clin Pharmacokinet. 2004; 43:879-923.
12. Cuvillon P, Alonso S, L'Hermite J, Reubrecht V, Zoric L, Vialles N, Luc Faillie J, Kouyoumdjian P, Boisson C, Raux M, Langeron O. Post-operative opioid-related adverse events with intravenous oxycodone compared to morphine: a randomized controlled trial. Acta Anaesthesiol Scand. 2021; 65:40-46.

Received June 11, 2026; Revised July 27, 2026; Accepted August 15, 2026.

**Address correspondence to:*
Tomoji Maeda, Department of Clinical Pharmacy, Nihon Pharmaceutical University, 10281 Komuro, Ina-machi, Saitama 362-0807, Japan.
E-mail: t-maeda@nichiyaku.ac.jp

Released online in J-STAGE as advance publication August 21, 2026.

**Correspondence**

DOI: 10.5582/ddt.2026.01054

# Acitretin-inspired medicinal chemistry for Alzheimer's disease: A biomarker-gated central nervous system (CNS) discovery framework

**Tian-Ge Qin[1], Yue Han[2,*]**

[1] Department of Medical Technology, Clinical College of Anhui Medical University, Hefei, Anhui, China;
[2] Department of Dermatology, The Union Hospital, Fujian Medical University, Fuzhou, Fujian, China.

**SUMMARY**: Alzheimer's disease (AD) still lacks scalable oral strategies for early intervention. This article examines acitretin, a systemic retinoid used for severe psoriasis, as a clinically characterized scaffold for central nervous system (CNS) medicinal chemistry—not as a parent drug for direct repurposing or as a predefined candidate. Retinoic acid receptor/retinoid X receptor signaling can induce a disintegrin and metalloprotease 10 (ADAM10), the principal neuronal α-secretase of amyloid precursor protein, thereby encouraging non-amyloidogenic cleavage and soluble amyloid precursor protein-α (sAPPα) production. Supporting evidence includes mechanistic studies, murine blood-brain barrier penetration, functional observations in an amyloid mouse model, and a small randomized human study showing a short-term increase in cerebrospinal fluid sAPPα. These findings provide a human biomarker anchor but do not establish adequate unbound brain exposure, durable target engagement, clinical efficacy, or a safe chronic therapeutic window. The resulting concept is an evidence-gated scaffold-redesign strategy: future work may test whether retinoid-ADAM10-APP signaling can be retained while systemic retinoid burden and metabolite persistence are reduced. Further progression would require convergence of unbound CNS exposure, bounded sAPPα modulation, and acceptable safety within the same concentration range.

***Keywords***: Alzheimer's disease, acitretin, ADAM10, α-secretase, soluble APP-α, retinoid signaling

## 1. Introduction

Alzheimer's disease (AD) remains a major unmet need in drug discovery. Clinically familiar interventions outside neurology can generate useful neuroprotective hypotheses, as illustrated by the recent discussion of herpes zoster vaccination and dementia, but such observations require rigorous mechanistic and translational validation (*1*). The World Health Organization estimated that 57 million people were living with dementia in 2021, with almost 10 million new cases each year (*2*). Disease-modifying antibodies have advanced the treatment of early AD, and yet infusion requirements, amyloid-related imaging abnormalities, and eligibility restrictions preserve a need for lower-burden oral strategies that engage disease biology upstream of plaque removal (*3-5*).

This article examines one such strategy: using acitretin as a starting scaffold for central nervous system (CNS) medicinal chemistry. The proposal is not to administer psoriasis-dose acitretin to older adults with AD, to label an unsynthesized analog as a drug candidate, or to describe conventional drug repurposing. The central question is whether the scaffold's experimentally supported connection to retinoid signaling and ADAM10-dependent amyloid precursor protein (APP) processing can be retained while systemic retinoid liabilities are reduced.

The distinctive contribution is an evidence-gated scaffold discovery framework: acitretin-inspired analogs advance only when adequate unbound CNS exposure, bounded APP-processing target engagement, and acceptable safety converge within the same concentration range. By converting a compound-specific human CSF biomarker signal into explicit progression and stop criteria, the framework links published evidence to design questions and translational gaps (Figure 1; Table 1).

## 2. Why the acitretin scaffold?

Acitretin is licensed for severe psoriasis and is accompanied by a mature clinical safety vocabulary that includes pregnancy prevention, liver-enzyme

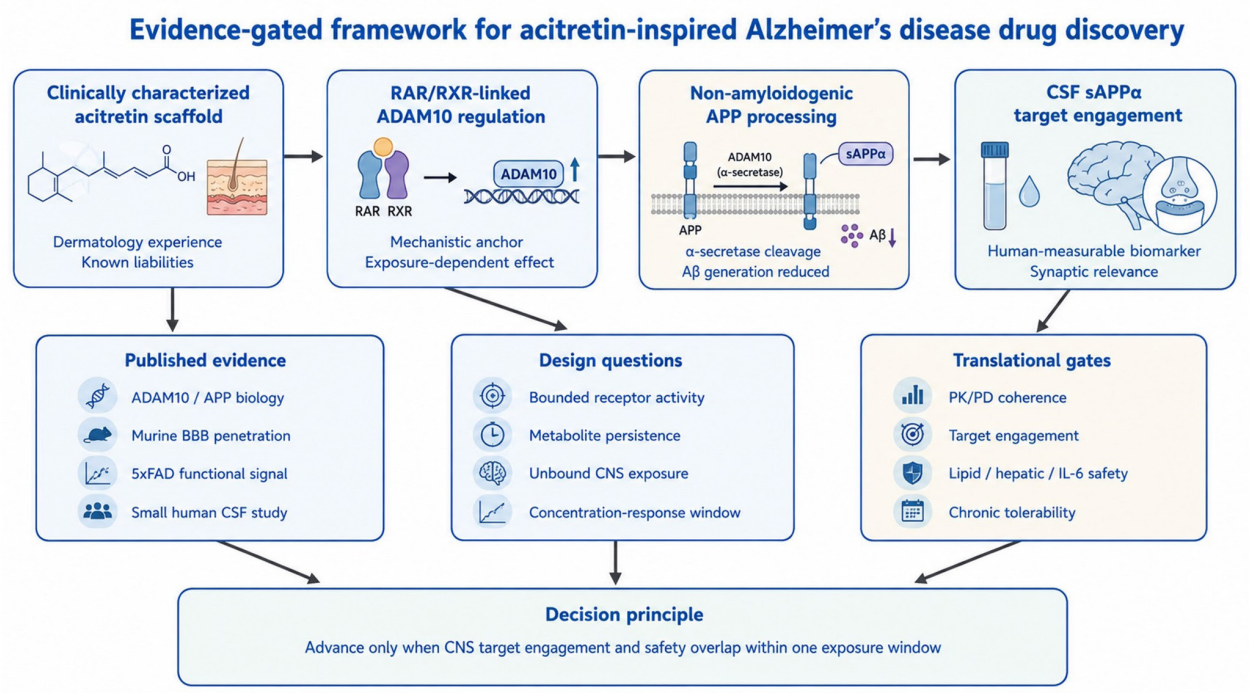


**Figure 1. Evidence-gated framework for an acitretin-inspired Alzheimer's disease drug-discovery strategy.** The upper pathway connects a clinically characterized dermatologic scaffold to RAR/RXR-linked ADAM10 regulation, non-amyloidogenic APP processing, and CSF sAPPα as a measurable target-engagement signal. The lower row separates published evidence from the questions that medicinal chemistry and translational pharmacology must resolve. Existing support includes ADAM10/APP biology, murine blood-brain barrier penetration, functional observations in a 5xFAD mouse model, and a small human CSF biomarker study. These findings do not define a drug candidate. Future analogs would need bounded receptor activity, a known metabolite profile, adequate unbound CNS exposure, and a concentration range in which sAPPα modulation occurs without unacceptable lipid, hepatic, mucocutaneous, inflammatory, skeletal, neuropsychiatric, or reproductive liabilities. Further progression would depend on the convergence of pharmacokinetic, biomarker, and safety evidence within the same exposure window. *Abbreviations*: ADAM10, a disintegrin and metalloprotease 10; APP, amyloid precursor protein; Aβ, amyloid-β; BBB, blood-brain barrier; CNS, central nervous system; CSF, cerebrospinal fluid; IL-6, interleukin-6; PK/PD, pharmacokinetics/pharmacodynamics; RAR/RXR, retinoic acid receptor/retinoid X receptor; sAPPα, soluble APP-α.

monitoring, fasting lipids, and mucocutaneous toxicity (*6*). This history does not make the parent drug suitable for chronic use in older adults with AD. It does, however, make the scaffold unusually informative: major liabilities are visible before neurological development begins, allowing them to function as design constraints rather than late clinical surprises.

The scaffold is not selected because acitretin is presumed to be the most potent or selective retinoid. Its value lies in the convergence of features reviewed below: a defined receptor-to-ADAM10 mechanism, evidence of murine brain access, a human CSF target-engagement signal, extensive dermatologic exposure, and clear opportunities for structural optimization. Few proposed CNS scaffolds enter discovery with both a measurable human pharmacodynamic observation and such a well-described liability profile.

Within the evidence reviewed here, acitretin is prioritized over other RAR/RXR-related retinoids because its compound-specific evidence aligns unusually well with the proposed gates: murine brain penetration, a human CSF sAPPα signal, extensive clinical exposure, and a well-defined liability profile (*6,15,16*). Bexarotene remains an informative class comparator, but its different receptor pharmacology, negative proof-of-concept clinical result, and triglyceride liability do not provide the same ADAM10-centered biomarker bridge (*14*). Other retinoids should therefore be treated as comparators or alternative scaffolds rather than assumed substitutes.

This combination changes the development question. The relevant comparison is not whether acitretin can outperform current AD therapies, but whether medicinal chemistry can separate the desired CNS pharmacology from the parent drug's systemic retinoid burden. A negative answer would be scientifically useful because it would finally refute a clearly defined scaffold hypothesis rather than prolong an open-ended repurposing narrative.

## 3. Biological rationale: The RAR/RXR-ADAM10-APP axis

### 3.1. ADAM10 and non-amyloidogenic APP processing

ADAM10 is the principal constitutive neuronal α-secretase of APP; cleavage within the amyloid-β (Aβ) sequence shifts processing away from β- and γ-secretase-dependent Aβ generation (*7,8*). Neuronal ADAM10 overexpression increased sAPPα, reduced amyloid deposition, and rescued hippocampal abnormalities in APP-transgenic mice (*9*), supporting APP shunting as a

**Table 1. Evidence, limitations, and decision gates for acitretin-inspired CNS medicinal chemistry**

| Dimension | Current evidence | Evidence level | Decision gate or limitation |
|---|---|---|---|
| Clinical scaffold | Acitretin is used for severe psoriasis, with established monitoring for pregnancy, liver enzymes, lipids, and mucocutaneous toxicity (*6*). | Established clinical use | Known liabilities inform design but do not eliminate the risk of prolonged treatment of the CNS in older adults. |
| Mechanistic axis | ADAM10 is the principal neuronal α-secretase of APP; RAR/RXR signaling and acitretin can increase ADAM10 and α-secretase activity (*7-11*). | Mechanistic and preclinical | The relevant question is whether target engagement can be bounded given ADAM10's multiple neuronal substrates. |
| CNS exposure | Acitretin crossed the murine blood-brain barrier and was not apparently eliminated by P-glycoprotein (*15*). | Murine preclinical | Human unbound brain exposure and the distribution of redesigned analogs remain unknown. |
| Human biomarker | Four weeks of acitretin increased CSF sAPPα in a small randomized study of 21 patients with AD (*16*). | Small human pilot | The finding supports target-engagement testing, not disease-modification or cognitive-efficacy claims. |
| Functional and safety signals | Acitretin increased IL-6 in AD-model mice and human CSF and improved early network and behavioral abnormalities in 5xFAD mice (*17,18*). | Translational and mouse-model evidence | Whether a concentration window can separate APP-processing effects from inflammatory and systemic retinoid liabilities remains to be determined. |
| Scaffold redesign | No CNS-oriented acitretin analog has been structurally defined or validated in the evidence summarized here. | Hypothesis requiring validation | A basis for progression would require convergence of unbound CNS exposure, sAPPα modulation, and safety within the same exposure range. |

*Abbreviations*: AD, Alzheimer's disease; ADAM10, a disintegrin and metalloprotease 10; APP, amyloid precursor protein; CNS, central nervous system; CSF, cerebrospinal fluid; IL-6, interleukin-6; RAR/RXR, retinoic acid receptor/retinoid X receptor; sAPPα, soluble APP-α.

mechanistic rationale rather than evidence of therapeutic efficacy.

The target is nevertheless pleiotropic. ADAM10 processes multiple neuronal and developmental substrates, making indiscriminate maximization biologically implausible and potentially unsafe (*10*). The desired pharmacology is therefore bounded target engagement: sufficient change in APP cleavage to produce a reproducible sAPPα signal without evidence that broader ADAM10 activity is causing unacceptable effects.

### 3.2. Retinoid regulation and the role of sAPPα

Retinoic acid receptor/retinoid X receptor (RAR/RXR) signaling provides the regulatory bridge between the acitretin scaffold and ADAM10: retinoic acid receptors can increase ADAM10 expression, and acitretin increased ADAM10 promoter activity and α-secretase activity in experimental systems (*11*). For development, the key question is not whether the pathway can be activated, but whether it can be engaged reproducibly at exposures compatible with prolonged treatment of the CNS.

sAPPα provides a practical pharmacodynamic readout and is reported to have neurotrophic and synaptic actions (*12*). However, its increase should be interpreted as target engagement, not proof of neuroprotection or disease modification; the transfer of this mechanism to a redesigned analog must be demonstrated in human-relevant neuronal systems.

### 3.3. A class-level caution from bexarotene

The retinoid class also provides a cautionary comparator. Bexarotene produced striking amyloid and behavioral findings in mouse models (*13*), but a subsequent proof-of-concept study in moderate AD did not meet its primary clinical objective and raised clinically relevant triglyceride concerns (*14*). This experience argues against treating receptor activity or favorable animal data as sufficient evidence. Human exposure, target engagement, and safety would need to be evaluated together.

## 4. Translational evidence for the acitretin scaffold

### 4.1. Brain access: Suggestive but unresolved

Acitretin crossed the murine blood-brain barrier and was not apparently eliminated by P-glycoprotein (*15*). This result supports biological plausibility, but it does not establish adequate unbound human brain exposure, and it cannot predict the distribution of a redesigned analog. Total plasma or tissue concentration would also be insufficient if protein binding, active transport, or metabolite formation prevents pharmacologically relevant free-drug exposure in the CNS.

### 4.2. The human CSF biomarker signal

The strongest translational anchor is a four-week randomized pilot study of 21 patients with mild-to-moderate AD, in which acitretin at 30 mg/day increased CSF sAPPα relative to a placebo (*16*). Although too small and brief to assess durable target engagement, cognition, or disease modification, the study provides compound-specific human evidence that systemic acitretin can alter an AD-relevant APP-processing biomarker.

This finding supports exposure-response testing of redesigned analogs at lower systemic retinoid burden, not chronic acitretin treatment. Paired plasma/CSF pharmacokinetics and a related APP-cleavage biomarker panel would be required to determine whether target engagement occurs within a viable therapeutic window.

4.3. Functional signals and inflammatory caution

The broader record is mixed in a way that is informative for development. Acitretin increased interleukin-6 (IL-6) in AD-model mice and in human CSF, indicating that retinoid immunopharmacology may not be uniformly beneficial (*17*). In 5xFAD mice, acitretin rebalanced early cortical network abnormalities and improved behavioral deficits (*18*). The functional observation supports plausibility, but a familial amyloid model cannot establish efficacy in sporadic human AD.

Taken together, the evidence spans molecular studies, a mouse brain-distribution experiment, a functional mouse model, and a small human biomarker trial. The signal is therefore broader than a single *in vitro* mechanism, yet it remains insufficient for a clinical-efficacy claim. Its value is to motivate the next falsifiable experiments.

## 5. Central innovation: Evidence-gated scaffold redesign

Here, acitretin functions as a clinically characterized scaffold and human biomarker anchor, not as the therapy to be repurposed. Advancement is therefore compound-agnostic: any analog must earn progression through predefined exposure, pharmacodynamic, and safety evidence rather than through resemblance to a prespecified molecular candidate.

The framework contains three linked gates. The exposure gate asks whether a compound achieves predictable unbound CNS concentrations without excessive peripheral exposure or persistent metabolites. The pharmacodynamic gate asks whether those concentrations produce a bounded increase in non-amyloidogenic APP processing, ideally supported by coherent changes in sAPPα and related APP-cleavage markers. The safety gate asks whether the same exposure range avoids unacceptable lipid, hepatic, mucocutaneous, skeletal, neuropsychiatric, reproductive, and inflammatory effects.

The three evidence domains are informative only if they overlap. Brain exposure without target engagement, or sAPPα modulation only at systemically toxic concentrations, would argue against further development. This decision architecture addresses a recurring difficulty in ADAM10 modulation: its mechanistic plausibility is high, but its target pleiotropy and translational uncertainty are substantial (*19*).

## 6. Remaining challenges and testable next steps

6.1. Medicinal chemistry and pharmacokinetics

Near-term medicinal chemistry should first define the chemical and pharmacological design space rather than optimize against a fixed potency target. Core measurements include RAR/RXR activity and selectivity, transporter interactions, plasma and brain protein binding, microsomal and hepatocyte stability, metabolite identity, and unbound brain exposure. Optimization should prioritize concentration-response relationships and the widest overlap between CNS target engagement and tolerability, while explicitly testing whether etretinate-like metabolite persistence and systemic retinoid pharmacology can be reduced.

6.2. Human-relevant translational models

Candidate analogs should be compared across human-relevant neuronal, hepatic, and inflammatory systems at matched concentrations, integrating ADAM10 induction, APP-cleavage products, IL-6 signaling, lipid-related effects, and cytotoxicity. This design would test pathway-liability separation before animal efficacy is used to justify progression. The framework should be considered falsified if APP-processing activity is lost after liability-reducing structural changes, requires broad retinoid saturation, or occurs only at concentrations that also produce clinically unacceptable hepatic, lipid, inflammatory, or other signals.

6.3. Potential human biomarker bridge

Only after a credible preclinical exposure window is established would a human biomarker study be informative. Its purpose should be to test whether plasma and CSF exposure co-varies with sAPPα and related APP-processing markers within prespecified tolerability and stopping boundaries, not to seek preliminary cognitive efficacy. Population, dose, and design should therefore remain contingent on a structurally defined analog and reproducible preclinical target engagement; clinical-efficacy testing lies beyond the present evidence.

## 7. Conclusion

Available evidence does not justify recommending acitretin for AD or naming a specific acitretin-derived

drug candidate. It supports a narrower and more testable conclusion: the acitretin scaffold merits evaluation as a human-biomarker-anchored starting point for CNS medicinal chemistry centered on ADAM10 and non-amyloidogenic APP processing.

The framework's value lies in its falsifiability. Further progression would depend on the convergence of unbound CNS exposure, bounded sAPPα target engagement, and an acceptable safety profile within the same concentration window. Failure to achieve this overlap would weaken or close the scaffold hypothesis; evidence of overlap would justify more extensive translational evaluation. Thus, acitretin-inspired chemistry is best viewed as a testable drug-discovery framework rather than a claim for a specific candidate. More broadly, the same evidence-gated logic may be transferable to other clinically characterized drug scaffolds for which a human pharmacodynamic anchor and a well-defined liability profile can be converted into explicit medicinal-chemistry decision gates.

*Funding*: None.

*Conflict of Interest*: The authors have no conflicts of interest to disclose.

**References**

1. Ma YN, Karako K, Song P, Xia Y. Can the herpes zoster vaccination be a strategy against dementia? Drug Discov Ther. 2025; 19:124-128.
2. World Health Organization. Dementia. *https://www.who.int/news-room/fact-sheets/detail/dementia* (accessed June 18, 2026).
3. Cummings J, Zhou Y, Lee G, Zhong K, Fonseca J, Cheng F. Alzheimer's disease drug development pipeline: 2024. Alzheimers Dement (N Y). 2024; 10:e12465.
4. van Dyck CH, Swanson CJ, Aisen P, *et al*. Lecanemab in early Alzheimer's disease. N Engl J Med. 2023; 388:9-21.
5. Sims JR, Zimmer JA, Evans CD, *et al*. Donanemab in early symptomatic Alzheimer disease: The TRAILBLAZER-ALZ 2 randomized clinical trial. JAMA. 2023; 330:512-527.
6. DailyMed. Acitretin capsule. *https://dailymed.nlm.nih.gov/dailymed/* (accessed June 18, 2026).
7. Lammich S, Kojro E, Postina R, Gilbert S, Pfeiffer R, Jasionowski M, Haass C, Fahrenholz F. Constitutive and regulated alpha-secretase cleavage of Alzheimer's amyloid precursor protein by a disintegrin metalloprotease. Proc Natl Acad Sci U S A. 1999; 96:3922-3927.
8. Kuhn PH, Wang H, Dislich B, Colombo A, Zeitschel U, Ellwart JW, Kremmer E, Rossner S, Lichtenthaler SF. ADAM10 is the physiologically relevant, constitutive alpha-secretase of the amyloid precursor protein in primary neurons. EMBO J. 2010; 29:3020-3032.
9. Postina R, Schroeder A, Dewachter I, Bohl J, Schmitt U, Kojro E, Prinzen C, Endres K, Hiemke C, Blessing M, Flamez P, Dequenne A, Godaux E, van Leuven F, Fahrenholz F. A disintegrin-metalloproteinase prevents amyloid plaque formation and hippocampal defects in an Alzheimer disease mouse model. J Clin Invest. 2004; 113:1456-1464.
10. Saftig P, Lichtenthaler SF. The alpha secretase ADAM10: A metalloprotease with multiple functions in the brain. Prog Neurobiol. 2015; 135:1-20.
11. Tippmann F, Hundt J, Schneider A, Endres K, Fahrenholz F. Up-regulation of the alpha-secretase ADAM10 by retinoic acid receptors and acitretin. FASEB J. 2009; 23:1643-1654.
12. Muller UC, Deller T, Korte M. Not just amyloid: Physiological functions of the amyloid precursor protein family. Nat Rev Neurosci. 2017; 18:281-298.
13. Cramer PE, Cirrito JR, Wesson DW, Lee CYD, Karlo JC, Zinn AE, Casali BT, Restivo JL, Goebel WD, James MJ, Brunden KR, Wilson DA, Landreth GE. ApoE-directed therapeutics rapidly clear beta-amyloid and reverse deficits in AD mouse models. Science. 2012; 335:1503-1506.
14. Cummings JL, Zhong K, Kinney JW, Heaney C, Moll-Tudla J, Joshi A, Pontecorvo M, Devous M, Tang A, Bena J. Double-blind, placebo-controlled, proof-of-concept trial of bexarotene in moderate Alzheimer's disease. Alzheimers Res Ther. 2016; 8:4.
15. Holthoewer D, Endres K, Schuck F, Hiemke C, Schmitt U, Fahrenholz F. Acitretin, an enhancer of alpha-secretase expression, crosses the blood-brain barrier and is not eliminated by P-glycoprotein. Neurodegener Dis. 2012; 10:224-228.
16. Endres K, Fahrenholz F, Lotz J, Hiemke C, Teipel S, Lieb K, Tuscher O, Fellgiebel A. Increased CSF APPs-alpha levels in patients with Alzheimer disease treated with acitretin. Neurology. 2014; 83:1930-1935.
17. dos Santos Guilherme M, Stoye NM, Rose-John S, Garbers C, Fellgiebel A, Endres K. The synthetic retinoid acitretin increases IL-6 in the central nervous system of Alzheimer disease model mice and human patients. Front Aging Neurosci. 2019; 11:182.
18. Rosales Jubal E, Schwalm M, Dos Santos Guilherme M, Schuck F, Reinhardt S, Tose A, Barger Z, Roesler MK, Ruffini N, Wierczeiko A, Schmeisser MJ, Schmitt U, Endres K, Stroh A. Acitretin reverses early functional network degradation in a mouse model of familial Alzheimer's disease. Sci Rep. 2021; 11:6649.
19. Khezri MR, Mohebalizadeh M, Ghasemnejad-Berenji M. Therapeutic potential of ADAM10 modulation in Alzheimer's disease: A review of the current evidence. Cell Commun Signal. 2023; 21:60.

Received June 19, 2026; Revised August 6, 2026; Accepted August 10, 2026.

**Address correspondence to:*
Yue Han, Department of Dermatology, The Union Hospital, Fujian Medical University, 29 Xinquan Road, Fuzhou, China 350001.
E-mail: dr_hanyue@126.com

Released online in J-STAGE as advance publication August 18, 2026.

**Correspondence**

DOI: 10.5582/ddt.2026.01051

# Enlicitide: The first oral PCSK9 inhibitor approved for treatment of hypercholesterolemia

**Yueyi Sun, Jianjun Gao***

Department of Pharmacology, School of Pharmacy, Qingdao University, Qingdao, Shandong, China.

**SUMMARY**: Hypercholesterolemia, and particularly elevated low-density lipoprotein cholesterol (LDL-C), is a major causal factor in atherosclerotic cardiovascular disease (ASCVD) and contributes substantially to coronary heart disease, ischemic stroke, and peripheral artery disease. Statins remain the cornerstone of lipid-lowering therapy, while ezetimibe and injectable proprotein convertase subtilisin/kexin 9 (PCSK9) targeted agents are added when further LDL-C reduction is required. However, concerns about injections, cost, accessibility, and treatment inertia have limited the use of existing PCSK9 therapies, creating a need for potent oral alternatives. Enlicitide, approved by the US Food and Drug Administration in July 2026, is the first approved oral PCSK9 inhibitor. This macrocyclic peptide blocks the interaction between circulating PCSK9 and hepatic LDL receptors, thereby increasing receptor recycling and LDL-C clearance. In the phase III CORALreef Lipids and CORALreef HeFH trials, once-daily enlicitide reduced LDL-C by approximately 60%, and the effect was maintained for up to 52 weeks. Adverse event rates were generally similar to those observed with a placebo. Nevertheless, those trials primarily evaluated LDL-C reduction rather than cardiovascular outcomes, and their duration was insufficient to establish long-term safety. The ongoing CORALreef Outcomes trial will determine whether enlicitide-mediated LDL-C reduction translates into fewer major cardiovascular events and will help define its long-term clinical role.

***Keywords***: PCSK9, LDL-C, LDLR, ASCVD, enlicitide

Hypercholesterolemia is a lipid metabolism disorder characterized primarily by elevated plasma total cholesterol, and low-density lipoprotein cholesterol (LDL-C) in particular. Cumulative exposure to LDL-C over time promotes lipid retention within the arterial intima, triggering inflammation and atherosclerotic plaque formation and ultimately increasing the risks of coronary heart disease, ischemic stroke, and peripheral artery disease (*1*). Genetic and epidemiological studies have established LDL as an important causal factor in atherosclerotic cardiovascular disease (ASCVD) (*2*). A study covering 200 countries showed that the global burden of cholesterol-related diseases is gradually shifting from high-income Western countries to East and Southeast Asia (*3*). In 2017, elevated non-high-density lipoprotein cholesterol (non-HDL-C) was responsible for approximately 3.9 million deaths, half of which occurred in East, Southeast, and South Asian countries (*3*).

Treatments for elevated LDL-C in patients with hypercholesterolemia should be individualized according to the overall risk of cardiovascular events (*4*). Dietary modifications, regular physical activity, weight management, and smoking cessation are the foundations of long-term management; however, most high-risk patients still require pharmacological treatment. Statins have robust evidence supporting their cardiovascular benefits and remain the cornerstone of lipid-lowering therapy (*5*). For patients who fail to achieve target LDL-C levels despite receiving a maximally tolerated statin dose, additional agents such as ezetimibe are generally recommended. For patients with very-high-risk ASCVD, heterozygous familial hypercholesterolemia (HeFH), or a need for substantial LDL-C reduction, early combination therapy incorporating a proprotein convertase subtilisin/kexin 9 (PCSK9) targeted agent should be considered (*6*).

Before the approval of enlicitide, all marketed therapies targeting PCSK9 were administered by injection. Alirocumab and evolocumab act by binding to circulating PCSK9, they reduce LDL-C levels by approximately 60%, and they have been found to decrease the incidence of cardiovascular events (*7,8*). Inclisiran, a small interfering RNA therapeutic, lowers LDL-C by suppressing PCSK9 synthesis in hepatocytes. It is administered once every six months and reduces LDL-C levels by approximately 50% (*9*). Despite

their potent lipid-lowering effects, these agents may be used to a limited extent clinically due to concerns about injections, cost, accessibility, and therapeutic inertia. Conversely, conventional oral non-statin agents generally do not provide a sufficient LDL-C reduction to meet the treatment needs of some high-risk patients. Therefore, an agent combining the convenience of oral administration with potent LDL-C-lowering efficacy has long represented an unmet clinical need.

On July 15, 2026, the US Food and Drug Administration approved enlicitide (trade name: LIPFENDRA) 20-mg tablets as an adjunct to diet and exercise to reduce LDL-C levels in adults with hypercholesterolemia, including those with HeFH. Enlicitide is the first oral PCSK9 inhibitor approved worldwide (*10,11*). It is a macrocyclic peptide that binds to circulating PCSK9 and blocks its interaction with the low-density lipoprotein receptor (LDLR) on the hepatocyte surface. This reduces LDLR degradation, allowing more receptors to be recycled to the hepatocyte surface and remove LDL-C from the circulation (*11,12*). Enlicitide tablets contain sodium caprate as an absorption enhancer, although their oral bioavailability remains only approximately 1%. The tablet must be swallowed whole in the morning on an empty stomach, and patients should wait at least 30 min after administration before eating. Its principal advantage is that it reduces LDL-C to a similar extent as PCSK9 monoclonal antibodies, albeit through oral administration, and it thereby represents a new option for patients who are unwilling or unable to receive long-term injectable therapy.

The approval of enlicitide was based primarily on two phase III randomized controlled trials. The CORALreef Lipids trial (NCT05952856) enrolled adults who had experienced an ASCVD event or were at risk of a first ASCVD event and who required further LDL-C reduction despite receiving stable lipid-lowering therapy (*13*). A total of 2,904 patients were included in the efficacy and safety analyses and were assigned in a ratio of 2:1 to receive enlicitide 20 mg or a placebo once daily for 52 weeks (*13*). At week 24, LDL-C levels had changed from the baseline by −57.1% in the enlicitide group and 3.0% in the placebo group, with an adjusted between-group difference of −55.8 percentage points. At week 52, the between-group difference remained −47.6 percentage points. The incidence of adverse events was comparable between the two groups (*13*). The CORALreef HeFH trial (NCT05952869) enrolled 303 adults with HeFH who were receiving stable moderate- or high-intensity statin therapy and randomly assigned them in a ratio of 2:1 to receive enlicitide or a placebo (*14*). At week 24, LDL-C levels had changed from the baseline by −58.2% and 2.6%, respectively, with a between-group difference of −59.4 percentage points (*14*). At week 52, the between-group difference was −61.5 percentage points, indicating that the lowering of LDL-C was sustained for one year. The incidence of adverse events was similar between the two groups (*14*).

The two studies consistently demonstrated the potent LDL-C-lowering efficacy of enlicitide; however, several limitations should be considered when interpreting their findings. First, the principal efficacy endpoint was the change in LDL-C rather than clinical outcomes such as myocardial infarction, stroke, or cardiovascular death. Second, a 52-week follow-up period is insufficient to evaluate efficacy over several years or to detect rare adverse events. The HeFH trial also had a relatively small sample size, and the high levels of adherence to the dosing and fasting requirements achieved in clinical trials may not be reproducible in routine clinical practice. Therefore, the available evidence supports the marked LDL-C-lowering efficacy of enlicitide but does not yet directly demonstrate that it reduces cardiovascular events.

The CORALreef Outcomes trial (NCT06008756) is currently underway. This phase III randomized, placebo-controlled trial involves approximately 14,550 adults at high cardiovascular risk and is designed primarily to determine whether enlicitide reduces the risk of a composite endpoint including coronary heart disease death, myocardial infarction, ischemic stroke, and major adverse limb events (*11,15*). The trial will determine whether the substantial LDL-C reduction achieved with enlicitide translates into fewer cardiovascular events in the future.

*Funding*: None.

*Conflict of Interest*: The authors have no conflicts of interest to disclose.

**References**

1. Stein JH, Tattersall MC. Familial Hypercholesterolemia. JAMA. 2026. doi: 10.1001/jama.2026.8822.
2. Ference BA, Ginsberg HN, Graham I, *et al*. Low-density lipoproteins cause atherosclerotic cardiovascular disease. 1. Evidence from genetic, epidemiologic, and clinical studies. A consensus statement from the European Atherosclerosis Society Consensus Panel. Eur Heart J. 2017; 38:2459-2472.
3. Collaboration NCDRF. Repositioning of the global epicentre of non-optimal cholesterol. Nature. 2020; 582:73-77.
4. Palloni MC, Farella T, Faggiano A, Vatri M, Fattirolli F, Angelino E, Ambrosetti M, Ruscica M, Corsini A, Carugo S, Poli A, Faggiano P. LDL-cholesterol distance to target: A practical tool for guiding lipid-lowering treatment decisions. Atheroscler Plus. 2026; 65:100574.
5. Zachariah D, Kakooza D, Pothas S, Thomas A, Kruger L. Statin therapy and cardiovascular prevention: Contemporary evidence, challenges, and future directions-A narrative review. Int J Environ Res Public Health. 2026; 23:921.
6. Blumenthal RS, Morris PB, Gaudino M, *et al.* 2026 ACC/AHA/AACVPR/ABC/ACPM/ADA/AGS/APhA/ASPC/NLA/PCNA Guideline on the Management of

Dyslipidemia: A Report of the American College of Cardiology/American Heart Association Joint Committee on Clinical Practice Guidelines. J Am Coll Cardiol. 2026; 87:2624-2757.
7. Sabatine MS, Giugliano RP, Keech AC, Honarpour N, Wiviott SD, Murphy SA, Kuder JF, Wang H, Liu T, Wasserman SM, Sever PS, Pedersen TR, FOURIER Steering Committee and Investigators. Evolocumab and clinical outcomes in patients with cardiovascular disease. N Engl J Med. 2017; 376:1713-1722.
8. Schwartz GG, Steg PG, Szarek M, *et al*. Alirocumab and cardiovascular outcomes after acute coronary syndrome. N Engl J Med. 2018; 379:2097-2107.
9. Ray KK, Wright RS, Kallend D, Koenig W, Leiter LA, Raal FJ, Bisch JA, Richardson T, Jaros M, Wijngaard PLJ, Kastelein JJP, ORION-10 and ORION-11 Investigators. Two Phase 3 trials of inclisiran in patients with elevated LDL cholesterol. N Engl J Med. 2020; 382:1507-1519.
10. US Food and Drug Administration. FDA approves first oral therapy that inhibits proprotein convertase subtilisin/kexin type 9 (PCSK9) to lower bad cholesterol in adults with high cholesterol. *https://www.fda.gov/news-events/press-announcements/fda-approves-first-oral-pcsk9-inhibitor-lower-ldl-cholesterol-adults-high-cholesterol* (accessed July 25, 2026).
11. MERCK. Merck's LIPFENDRA® (enlicitide) is the First and Only Once-Daily Oral PCSK9 Inhibitor Approved by the U.S. FDA to Reduce LDL-C in Adults with Hypercholesterolemia. *https://www.merck.com/news/mercks-lipfendra-enlicitide-is-the-first-and-only-once-daily-oral-pcsk9-inhibitor-approved-by-the-u-s-fda-to-reduce-ldl-c-in-adults-with-hypercholesterolemia/* (accessed July 27, 2026).
12. Johns DG, Campeau LC, Banka P, *et al*. Orally bioavailable macrocyclic peptide that inhibits binding of PCSK9 to the low density lipoprotein receptor. Circulation. 2023; 148:144-158.
13. Navar AM, Mikhailova E, Catapano AL, *et al*. A placebo-controlled trial of the oral PCSK9 inhibitor enlicitide. N Engl J Med. 2026; 394:529-539.
14. Ballantyne CM, Gellis L, Tardif JC, Banka P, Navar AM, Asprusten EA, Scott R, Stroes ESG, Froman S, Mendizabal G, Wang F, Catapano AL. Efficacy and safety of oral PCSK9 inhibitor enlicitide in adults with heterozygous familial hypercholesterolemia: A randomized clinical trial. JAMA. 2026; 335:129-139.
15. ClinicalTrials.gov. Enlicitide Decanoate (MK-0616 Oral PCSK9 Inhibitor) Cardiovascular Outcomes Study (MK-0616-015) CORALreef Outcomes. *https://clinicaltrials.gov/study/NCT06008756* (accessed July 28, 2026).

Received August 1, 2026; Accepted August 5, 2026.

**Address correspondence to:*
Jianjun Gao, Department of Pharmacology, School of Pharmacy, Qingdao University, Qingdao, Shandong, China.
E-mail: gaojj@qdu.edu.cn

Released online in J-STAGE as advance publication August 14, 2026.

**Correspondence**

DOI: 10.5582/ddt.2026.01056

# Oveporexton: The first-in-class orexin receptor 2 (OX2R) agonist approved for treatment of narcolepsy type 1 (NT1)

**Yueyi Sun, Jianjun Gao***

Department of Pharmacology, School of Pharmacy, Qingdao University, Qingdao, Shandong, China.

**SUMMARY**: Narcolepsy type 1 (NT1) is a chronic neurological disorder caused by selective loss of orexin-producing neurons, resulting in unstable sleep-wake regulation and characteristic symptoms including excessive daytime sleepiness (EDS), cataplexy, sleep paralysis, hypnagogic or hypnopompic hallucinations, and disrupted nocturnal sleep. Current treatments mainly provide partial symptomatic relief and do not correct the underlying orexin deficiency, highlighting the need for mechanism-based therapies. Oveporexton (TAK-861), an orally administered selective orexin receptor 2 (OX2R) agonist developed by Takeda Pharmaceuticals, represents the first approved therapy targeting the orexin pathway in NT1. By activating preserved OX2R signaling, oveporexton restores wakefulness regulation and alleviates multiple core symptoms of NT1. Its approval was aided by two global phase 3 trials which demonstrated significant improvements in wakefulness and cataplexy compared with placebo. Although its long-term safety, accessibility, and real-world efficacy need to be evaluated further, oveporexton represents a major advance toward disease mechanism-based treatment for NT1.

***Keywords***: narcolepsy, NT1, orexin, OX2R, EDS, cataplexy

## 1. Narcolepsy and disease burden

Narcolepsy is a chronic neurological disorder characterized by impaired stability of the sleep–wake state and dysregulation of rapid eye movement (REM) sleep (*1*). According to the International Classification of Sleep Disorders (ICSD), narcolepsy is mainly classified into narcolepsy type 1 (NT1) and narcolepsy type 2 (NT2). NT1 accounts for approximately 70% of all narcolepsy cases, and its core pathological feature is the selective loss of orexin (also known as hypocretin)-producing neurons in the lateral hypothalamus, resulting in markedly reduced orexin levels in cerebrospinal fluid (*2-4*).

Patients with NT1 typically present with excessive daytime sleepiness (EDS), cataplexy, sleep paralysis, hypnagogic or hypnopompic hallucinations, and disrupted nocturnal sleep (*1*). Among these symptoms, cataplexy is the key clinical feature distinguishing NT1 from NT2 and is considered to result from the abnormal intrusion of REM sleep-associated muscle atonia mechanisms into wakefulness (*1,5*). In contrast, NT2 is primarily characterized by EDS without typical cataplexy, and orexin levels in cerebrospinal fluid are generally normal. The underlying pathophysiological mechanisms of NT2 still have yet to be fully understood (*1,5*).

Although NT1 has a relatively low prevalence, it imposes a substantial disease burden. Epidemiological studies in the United States have reported a prevalence of approximately 0.025–0.05%, although estimates vary among different studies (*6*). In China, the true prevalence of narcolepsy remains unclear due to the lack of large-scale population-based studies; however, available surveillance data indicate that narcolepsy cases continue to be identified, with NT1 representing a substantial proportion of cases (*7*). Persistent daytime sleepiness and cataplexy significantly impair patients' academic performance, occupational ability, and social functioning. In addition, they increase the risk of traffic accidents and occupational injuries and are associated with depression, anxiety, obesity, and cardiometabolic abnormalities (*1,5*).

## 2. Current treatment landscape and the unmet clinical need for treatment of NT1

Current management of NT1 mainly includes behavioral interventions and pharmacological therapies. The major therapeutic goals are to alleviate EDS, reduce cataplexy episodes, optimize nocturnal sleep, and help patients regain normal social functioning (*8,9*). Pharmacological treatment remains a cornerstone of disease management.

Commonly used medications for EDS include modafinil, armodafinil, sodium oxybate, pitolisant, and solriamfetol. Modafinil has long been considered a first-line wake-promoting medication for many patients due to its established efficacy and favorable safety profile. Sodium oxybate can alleviate both EDS and cataplexy and it remains an important therapeutic option for NT1. Pitolisant and solriamfetol are newer medications developed primarily for the management of EDS (*8,9*). For cataplexy, sodium oxybate and certain antidepressants, including tricyclic antidepressants and serotonin reuptake inhibitors, can effectively reduce the frequency of attacks (*8,9*).

However, current treatments mainly act by enhancing wake-promoting pathways or modulating monoaminergic neurotransmission and cannot correct the fundamental pathological defect of orexin deficiency in NT1. Therefore, existing therapies only provide partial symptomatic relief, and many patients continue to experience residual sleepiness, cataplexy episodes, and impaired nocturnal sleep quality. Moreover, some medications are associated with limitations, including the potential risk of dependence, cardiovascular adverse effects, or insufficient evidence regarding long-term safety. Therefore, the development of mechanism-based therapies targeting the orexin pathway represents an important unmet clinical need.

## 3. Mechanism of action and approval status of oveporexton

Oveporexton (TAK-861; trade name ORZEYFUL) is an orally administered, highly selective orexin receptor 2 (OX2R) agonist developed by Takeda Pharmaceuticals. The orexin system plays a critical role in maintaining wakefulness stability, regulating sleep–wake transitions, and preventing inappropriate intrusion of REM sleep characteristics into wakefulness (*3*). Although patients with NT1 exhibit extensive loss of orexin-producing neurons, downstream OX2R signaling pathways remain preserved. Therefore, direct activation of OX2R represents a therapeutic strategy that bypasses neuronal loss and restores wakefulness regulation.

On July 23, 2026, the National Medical Products Administration (NMPA) of China announced that oveporexton tablets have been approved for the treatment of NT1 in adolescents and adults age 16 years and older, making it the first approved oral OX2R agonist globally (*10,11*). On August 5, 2026, the U.S. Food and Drug Administration (FDA) approved oveporexton tablets for the treatment of adult patients with NT1 (*12*). The approved indications differ between the two countries: China includes patients age ≥16 years, whereas in the U.S. the current indication is limited to adults. Compared to conventional wake-promoting medications, oveporexton directly restores orexin signaling and theoretically has the potential to alleviate multiple core symptoms of NT1, including EDS, cataplexy, and sleep–wake instability. Therefore, it represents an important transition from symptomatic management towards disease mechanism-based therapy.

## 4. Clinical evidence

The approval of oveporexton was primarily aided by two global phase 3 randomized, double-blind, placebo-controlled clinical trials. The FirstLight study (TAK-861-3001; NCT06470828) enrolled 168 patients with NT1 and evaluated the efficacy and safety of oveporexton at doses of 1 mg twice daily and 2 mg twice daily compared to a placebo over 12 weeks (*13*). Both doses significantly improved sleep latency in the Maintenance of Wakefulness Test (MWT), Epworth Sleepiness Scale (ESS) scores, and the weekly cataplexy rate (WCR). All primary and key secondary endpoints were met with significant improvement. At week 12, both oveporexton 1 mg and 2 mg twice daily significantly reduced the WCR, with an incidence ratio versus a placebo of 0.34 (95% CI, 0.20–0.57) and 0.38 (95% CI, 0.23–0.61), respectively (*13*).

The RadiantLight study (TAK-861-3002; NCT06505031) further evaluated the efficacy of oveporexton at 2 mg twice daily (*13*). This study enrolled 105 patients with NT1 who were randomized at a ratio of 2:1 to receive oveporexton or a placebo. Compared to a placebo, at week 12 the oveporexton group showed a 20.1-minute increase in MWT sleep latency, a 9.5-point greater reduction in ESS scores, and a significantly lower risk of cataplexy events (rate ratio, 0.25). All major efficacy outcomes were significant (*13*). The most frequently reported adverse events included insomnia, increased urinary frequency, urgency to urinate, and increased saliva production.

## 5. Clinical significance and future perspectives

The approval of oveporexton represents a major advance in the treatment of narcolepsy. Over the past several decades, NT1 management has relied primarily on wake-promoting agents and symptomatic therapies. Oveporexton is the first pharmacological intervention specifically targeting the core pathological defect of NT1, an orexin deficiency, and it represents an important breakthrough in mechanism-based treatment for sleep disorders.

Nevertheless, the long-term clinical value of oveporexton needs to be evaluated further. Orexin neuron loss in NT1 is generally irreversible, so whether OX2R activation can fully restore physiological sleep–wake regulation remains to be determined through long-term follow-up studies. In addition, further study needs to be performed to clarify the long-term safety, tolerability, and real-world efficacy of oveporexton and differences in treatment response among patients of different ages

and disease stages. Drug cost and accessibility may also influence its widespread clinical adoption.

Overall, oveporexton provides a novel therapeutic option for patients with NT1 based on disease mechanisms. Its approval represents a significant shift in the therapeutic paradigm of narcolepsy; however, its long-term clinical benefits need to be further assessed in clinical practice.

*Funding*: None.

*Conflict of Interest*: The authors have no conflicts of interest to disclose.

**References**

1. Bassetti CLA, Adamantidis A, Burdakov D, *et al*. Narcolepsy - Clinical spectrum, aetiopathophysiology, diagnosis and treatment. Nat Rev Neurol. 2019; 15:519-539.
2. Nishino S, Ripley B, Overeem S, Lammers GJ, Mignot E. Hypocretin (orexin) deficiency in human narcolepsy. Lancet. 2000; 355:39-40.
3. Rauf R, Asif S, AlSaafeen A, Dhantapaani KG, Nadeem MM, Rao ZK, Hameed ASS, Chintharala K, Anwar MF, Cheema AAA. Orexin deficiency in narcolepsy: Molecular mechanisms, clinical phenotypes, and emerging therapeutic frontiers. Brain Behav. 2025; 15:e70984.
4. Mignot E, Lammers GJ, Ripley B, Okun M, Nevsimalova S, Overeem S, Vankova J, Black J, Harsh J, Bassetti C, Schrader H, Nishino S. The role of cerebrospinal fluid hypocretin measurement in the diagnosis of narcolepsy and other hypersomnias. Arch Neurol. 2002; 59:1553-1562.
5. Blattner M, Maski K. Narcolepsy and idiopathic hypersomnia. Sleep Med Clin. 2023; 18:183-199.
6. Longstreth WT, Jr., Koepsell TD, Ton TG, Hendrickson AF, van Belle G. The epidemiology of narcolepsy. Sleep. 2007; 30:13-26.
7. Wang X, Xiao F, Wang Y, *et al*. Changed epidemiology of narcolepsy before, during, and after the 2009 H1N1 pandemic: A nationwide narcolepsy surveillance network study in mainland China, 1990-2017. Sleep. 2023; 46:zsac325..
8. Chinese Society of Sleep Disorders. Chinese guidelines for diagnosis and treatment of narcolepsy (2022). Zhonghua Shen Jing Ke Za Zhi. 2022; 55:406-420 (in Chinese).
9. Maski K, Trotti LM, Kotagal S, Robert Auger R, Rowley JA, Hashmi SD, Watson NF. Treatment of central disorders of hypersomnolence: An American Academy of Sleep Medicine clinical practice guideline. J Clin Sleep Med. 2021; 17:1881-1893.
10. Takeda Pharmaceuticals. Takeda's ORZEYFUL (oveporexton) Approved in China as First Orexin Agonist and Only Medicine to Treat Narcolepsy Type 1. *https://www.takeda.com/newsroom/newsreleases/2026/orzeyful-approved-china-narcolepsy/* (accessed August 6, 2026).
11. National Medical Products Administration. The National Medical Products Administration (NMPA) has granted marketing authorization for oveporexton tablets. *https://www.nmpa.gov.cn/zhuanti/cxylqx/cxypxx/20260723092018174.html* (accessed August 9, 2026) (in Chinese).
12. Food and Drug Administration. FDA Approves First Drug to Treat the Full Range of Narcolepsy Type 1 Symptoms. *https://www.fda.gov/news-events/press-announcements/fda-approves-first-drug-treat-full-range-narcolepsy-type-1-symptoms* (accessed August 7, 2026).
13. Orzeyful Prescribing Information. (*https://content.takeda.com/?contenttype=PI&product=ORZ&language=ENG&country=USA&documentnumber=1*) (accessed August 8, 2026).

Received August 12, 2026; Accepted August 16, 2026.

**Address correspondence to:*
Jianjun Gao, Department of Pharmacology, School of Pharmacy, Qingdao University, Qingdao, Shandong, China.
E-mail: xyz@st.kumamoto-u.ac.jp

Released online in J-STAGE as advance publication August 19, 2026.

DD&T
Drug Discoveries & Therapeutics

# Guide for Authors

**1. Scope of Articles**

***Drug Discoveries & Therapeutics*** (Print ISSN 1881-7831, Online ISSN 1881-784X) welcomes contributions in all fields of pharmaceutical and therapeutic research such as medicinal chemistry, pharmacology, pharmaceutical analysis, pharmaceutics, pharmaceutical administration, and experimental and clinical studies of effects, mechanisms, or uses of various treatments. Studies in drug-related fields such as biology, biochemistry, physiology, microbiology, and immunology are also within the scope of this journal.

**2. Submission Types**

**Original Articles** should be well-documented, novel, and significant to the field as a whole. An Original Article should be arranged into the following sections: Title page, Abstract, Introduction, Materials and Methods, Results, Discussion, Acknowledgments, and References. Original articles should not exceed 5,000 words in length (excluding references) and should be limited to a maximum of 50 references. Articles may contain a maximum of 10 figures and/or tables. Supplementary Data are permitted but should be limited to information that is not essential to the general understanding of the research presented in the main text, such as unaltered blots and source data as well as other file types.

**Brief Reports** definitively documenting either experimental results or informative clinical observations will be considered for publication in this category. Brief Reports are not intended for publication of incomplete or preliminary findings. Brief Reports should not exceed 3,000 words in length (excluding references) and should be limited to a maximum of 4 figures and/or tables and 30 references. A Brief Report contains the same sections as an Original Article, but the Results and Discussion sections should be combined.

**Reviews** should present a full and up-to-date account of recent developments within an area of research. Normally, reviews should not exceed 8,000 words in length (excluding references) and should be limited to a maximum of 10 figures and/or tables and 100 references. Mini reviews are also accepted, which should not exceed 4,000 words in length (excluding references) and should be limited to a maximum of 5 figures and/or tables and 50 references.

**Policy Forum** articles discuss research and policy issues in areas related to life science such as public health, the medical care system, and social science and may address governmental issues at district, national, and international levels of discourse. Policy Forum articles should not exceed 3,000 words in length (excluding references) and should be limited to a maximum of 5 figures and/or tables and 30 references.

**Case Reports** should be detailed reports of the symptoms, signs, diagnosis, treatment, and follow-up of an individual patient. Case reports may contain a demographic profile of the patient but usually describe an unusual or novel occurrence. Unreported or unusual side effects or adverse interactions involving medications will also be considered. Case Reports should not exceed 3,000 words in length (excluding references).

**Communications** are short, timely pieces that spotlight new research findings or policy issues of interest to the field of global health and medical practice that are of immediate importance. Depending on their content, Communications will be published as "Comments" or "Correspondence". Communications should not exceed 1,500 words in length (excluding references) and should be limited to a maximum of 2 figures and/or tables and 20 references.

**Editorials** are short, invited opinion pieces that discuss an issue of immediate importance to the fields of global health, medical practice, and basic science oriented for clinical application. Editorials should not exceed 1,000 words in length (excluding references) and should be limited to a maximum of 10 references. Editorials may contain one figure or table.

**News** articles should report the latest events in health sciences and medical research from around the world. News should not exceed 500 words in length.

**Letters** should present considered opinions in response to articles published in *Drug Discoveries & Therapeutics* in the last 6 months or issues of general interest. Letters should not exceed 800 words in length and may contain a maximum of 10 references. Letters may contain one figure or table.

**3. Editorial Policies**

For publishing and ethical standards, *Drug Discoveries & Therapeutics* follows the Recommendations for the Conduct, Reporting, Editing, and Publication of Scholarly Work in Medical Journals issued by the International Committee of Medical Journal Editors (ICMJE, *https://icmje.org/recommendations*), and the Principles of Transparency and Best Practice in Scholarly Publishing jointly issued by the Committee on Publication Ethics (COPE, *https://publicationethics.org/resources/guidelines-new/principles-transparency-and-best-practice-scholarly-publishing*), the Directory of Open Access Journals (DOAJ, *https://doaj.org/apply/transparency*), the Open Access Scholarly Publishers Association (OASPA, *https://oaspa.org/principles-of-transparency-and-best-practice-in-scholarly-publishing-4*), and the World Association of Medical Editors (WAME, *https://wame.org/principles-of-transparency-and-best-practice-in-scholarly-publishing*).

*Drug Discoveries & Therapeutics* will perform an especially prompt review to encourage innovative work. All original research will be subjected to a rigorous standard of peer review and will be edited by experienced copy editors to the highest standards.

**Ethical Approval of Studies and Informed Consent:** For all manuscripts reporting data from studies involving human participants or animals, formal review and approval, or formal review and waiver, by an appropriate institutional review board or ethics committee is required and should be described in the Methods section. When your manuscript contains any case details, personal information and/or images of patients or other individuals, authors must obtain appropriate written consent, permission and release in order to comply with all applicable laws and regulations concerning privacy and/or security of personal information. The consent form needs to comply with the relevant legal requirements of your particular jurisdiction, and please do not send signed consent form to *Drug Discoveries & Therapeutics* to respect your patient's and any other individual's privacy. Please instead describe the information clearly in the Methods (patient consent) section of your manuscript while retaining copies of the signed forms in the event they should be needed. Authors should also state that the study conformed to the provisions of the Declaration of Helsinki (as revised in 2013, *https://wma.net/what-we-do/medical-ethics/declaration-of-helsinki*). When reporting experiments on animals, authors should indicate whether the institutional and national guide for the care and use of laboratory animals was followed.

**Reporting Clinical Trials:** The ICMJE (*https:// icmje.org/recommendations/browse/publishing-and-editorial-issues/clinical-trial-registration.html*) defines a clinical trial as any research project that prospectively assigns people or a group of people to an intervention, with or without concurrent comparison or control groups, to study the relationship between a health-related intervention and a health outcome. Registration of clinical trials in a public trial registry

at or before the time of first patient enrollment is a condition of consideration for publication in *Drug Discoveries & Therapeutics*, and the trial registration number will be published at the end of the Abstract. The registry must be independent of for-profit interest and publicly accessible. Reports of trials must conform to CONSORT 2010 guidelines (*https://consort-statement.org/consort-2010*). Articles reporting the results of randomized trials must include the CONSORT flow diagram showing the progress of patients throughout the trial.

**Conflict of Interest:** All authors are required to disclose any actual or potential conflict of interest including financial interests or relationships with other people or organizations that might raise questions of bias in the work reported. If no conflict of interest exists for each author, please state "There is no conflict of interest to disclose".

**Submission Declaration:** When a manuscript is considered for submission to *Drug Discoveries & Therapeutics*, the authors should confirm that 1) no part of this manuscript is currently under consideration for publication elsewhere; 2) this manuscript does not contain the same information in whole or in part as manuscripts that have been published, accepted, or are under review elsewhere, except in the form of an abstract, a letter to the editor, or part of a published lecture or academic thesis; 3) authorization for publication has been obtained from the authors' employer or institution; and 4) all contributing authors have agreed to submit this manuscript.

**Initial Editorial Check:** Immediately after submission, the journal's managing editor will perform an initial check of the manuscript. A suitable academic editor will be notified of the submission and invited to check the manuscript and recommend reviewers. Academic editors will check for plagiarism and duplicate publication at this stage. The journal has a formal recusal process in place to help manage potential conflicts of interest of editors. In the event that an editor has a conflict of interest with a submitted manuscript or with the authors, the manuscript, review, and editorial decisions are managed by another designated editor without a conflict of interest related to the manuscript.

**Peer Review:** *Drug Discoveries & Therapeutics* operates a single-anonymized review process, which means that reviewers know the names of the authors, but the authors do not know who reviewed their manuscript. All articles are evaluated objectively based on academic content. External peer review of research articles is performed by at least two reviewers, and sometimes the opinions of more reviewers are sought. Peer reviewers are selected based on their expertise and ability to provide quality, constructive, and fair reviews. For research manuscripts, the editors may, in addition, seek the opinion of a statistical reviewer. Every reviewer is expected to evaluate the manuscript in a timely, transparent, and ethical manner, following the COPE guidelines (*https://publicationethics.org/files/cope-ethical-guidelines-peer-reviewers-v2_0.pdf*). We ask authors for sufficient revisions (with a second round of peer review, when necessary) before a final decision is made. Consideration for publication is based on the article's originality, novelty, and scientific soundness, and the appropriateness of its analysis.

**Suggested Reviewers:** A list of up to 3 reviewers who are qualified to assess the scientific merit of the study is welcomed. Reviewer information including names, affiliations, addresses, and e-mail should be provided at the same time the manuscript is submitted online. Please do not suggest reviewers with known conflicts of interest, including participants or anyone with a stake in the proposed research; anyone from the same institution; former students, advisors, or research collaborators (within the last three years); or close personal contacts. Please note that the Editor-in-Chief may accept one or more of the proposed reviewers or may request a review by other qualified persons.

**Language Editing:** Manuscripts prepared by authors whose native language is not English should have their work proofread by a native English speaker before submission. If not, this might delay the publication of your manuscript in *Drug Discoveries & Therapeutics*.

The Editing Support Organization can provide English proofreading, Japanese-English translation, and Chinese-English translation services to authors who want to publish in *Drug Discoveries & Therapeutics* and need assistance before submitting a manuscript. Authors can visit this organization directly at *https://www.iacmhr.com/iac-eso/support.php?lang=en. IAC-ESO* was established to facilitate manuscript preparation by researchers whose native language is not English and to help edit works intended for international academic journals.

**Copyright and Reuse:** Before a manuscript is accepted for publication in *Drug Discoveries & Therapeutics*, authors will be asked to sign a transfer of copyright agreement, which recognizes the common interest that both the journal and author(s) have in the protection of copyright. We accept that some authors (*e.g.*, government employees in some countries) are unable to transfer copyright. A JOURNAL PUBLISHING AGREEMENT (JPA) form will be e-mailed to the authors by the Editorial Office and must be returned by the authors by mail, fax, or as a scan. Only forms with a hand-written signature from the corresponding author are accepted. This copyright will ensure the widest possible dissemination of information. Please note that the manuscript will not proceed to the next step in publication until the JPA Form is received. In addition, if excerpts from other copyrighted works are included, the author(s) must obtain written permission from the copyright owners and credit the source(s) in the article.

**4. Cover Letter**

The manuscript must be accompanied by a cover letter prepared by the corresponding author on behalf of all authors. The letter should indicate the basic findings of the work and their significance. The letter should also include a statement affirming that all authors concur with the submission and that the material submitted for publication has not been published previously or is not under consideration for publication elsewhere. The cover letter should be submitted in PDF format. For an example of Cover Letter, please visit: Download Centre (*https://www.ddtjournal.com/downcentre)*.

**5. Submission Checklist**

The Submission Checklist should be submitted when submitting a manuscript through the Online Submission System. Please visit Download Centre (*https://www.ddtjournal.com/downcentre)* and download the Submission Checklist file. We recommend that authors use this checklist when preparing your manuscript to check that all the necessary information is included in your article (if applicable), especially with regard to Ethics Statements.

**6. Manuscript Preparation**

Manuscripts are suggested to be prepared in accordance with the "Recommendations for the Conduct, Reporting, Editing, and Publication of Scholarly Work in Medical Journals", as presented at *http://www.ICMJE.org*.

Manuscripts should be written in clear, grammatically correct English and submitted as a Microsoft Word file in a single-column format. Manuscripts must be paginated and typed in 12-point Times New Roman font with 24-point line spacing. Please do not embed figures in the text. Abbreviations should be used as little as possible and should be explained at first mention unless the term is a well-known abbreviation (*e.g.* DNA). Single words should not be abbreviated.

**Title page:** The title page must include 1) the title of the paper (Please note the title should be short, informative, and contain the major key words); 2) full name(s) and affiliation(s) of the author(s), 3) abbreviated names of the author(s), 4) full name, mailing address, telephone/fax numbers, and e-mail address of the corresponding author; 5) author contribution statements to specify the individual contributions of all authors to this manuscript, and 6) conflicts of interest (if you have an actual or potential conflict of interest to disclose, it must be included as a footnote on the title page of the manuscript; if no conflict of interest

exists for each author, please state "There is no conflict of interest to disclose").

**Abstract:** The abstract should briefly state the purpose of the study, methods, main findings, and conclusions. For article types including Original Article, Brief Report, Review, Policy Forum, and Case Report, a one-paragraph abstract consisting of no more than 250 words must be included in the manuscript. For Communications, Editorials, News, or Letters, a brief summary of main content in 150 words or fewer should be included in the manuscript. For articles reporting clinical trials, the trial registration number should be stated at the end of the Abstract. Abbreviations must be kept to a minimum and non-standard abbreviations explained in brackets at first mention. References should be avoided in the abstract. Three to six key words or phrases that do not occur in the title should be included in the Abstract page.

**Introduction:** The introduction should provide sufficient background information to make the article intelligible to readers in other disciplines and sufficient context clarifying the significance of the experimental findings.

**Materials/Patients and Methods:** The description should be brief but with sufficient detail to enable others to reproduce the experiments. Procedures that have been published previously should not be described in detail but appropriate references should simply be cited. Only new and significant modifications of previously published procedures require complete description. Names of products and manufacturers with their locations (city and state/country) should be given and sources of animals and cell lines should always be indicated. All clinical investigations must have been conducted in accordance with the Declaration of Helsinki (as revised in 2013, *https://wma.net/what-we-do/medical-ethics/declaration-of-helsinki*). All human and animal studies must have been approved by the appropriate institutional review board(s) and a specific declaration of approval must be made within this section.

**Results:** The description of the experimental results should be succinct but in sufficient detail to allow the experiments to be analyzed and interpreted by an independent reader. If necessary, subheadings may be used for an orderly presentation. All Figures and Tables should be referred to in the text in order, including those in the Supplementary Data.

**Discussion:** The data should be interpreted concisely without repeating material already presented in the Results section. Speculation is permissible, but it must be well-founded, and discussion of the wider implications of the findings is encouraged. Conclusions derived from the study should be included in this section.

**Acknowledgments:** All funding sources (including grant identification) should be credited in the Acknowledgments section. Authors should also describe the role of the study sponsor(s), if any, in study design; in the collection, analysis, and interpretation of data; in the writing of the report; and in the decision to submit the paper for publication. If the funding source had no such involvement, the authors should so state.

In addition, people who contributed to the work but who do not meet the criteria for authors should be listed along with their contributions.

**References:** References should be numbered in the order in which they appear in the text. Citing of unpublished results, personal communications, conference abstracts, and theses in the reference list is not recommended but these sources may be mentioned in the text. In the reference list, cite the names of all authors when there are fifteen or fewer authors; if there are sixteen or more authors, list the first three followed by *et al*. Names of journals should be abbreviated in the style used in PubMed. Authors are responsible for the accuracy of the references. The EndNote Style of *Drug Discoveries & Therapeutics* could be downloaded at **EndNote** (*https://www.ddtjournal.com/examples/Drug_Discoveries_Therapeutics.ens*).

Examples are given below:

*Example 1 (Sample journal reference):*

Nakata M, Tang W. Japan-China Joint Medical Workshop on Drug Discoveries and Therapeutics 2008: The need of Asian pharmaceutical researchers' cooperation. Drug Discov Ther. 2008; 2:262-263.

*Example 2 (Sample journal reference with more than 15 authors):*

Darby S, Hill D, Auvinen A, *et al*. Radon in homes and risk of lung cancer: Collaborative analysis of individual data from 13 European case-control studies. BMJ. 2005; 330:223.

*Example 3 (Sample book reference):*

Shalev AY. Post-traumatic stress disorder: Diagnosis, history and life course. In: Post-traumatic Stress Disorder, Diagnosis, Management and Treatment (Nutt DJ, Davidson JR, Zohar J, eds.). Martin Dunitz, London, UK, 2000; pp. 1-15.

*Example 4 (Sample web page reference):*

World Health Organization. The World Health Report 2008 – primary health care: Now more than ever. *https://apps.who.int/iris/handle/10665/43949* (accessed September 23, 2022).

**Tables:** All tables should be prepared in Microsoft Word or Excel and should be arranged at the end of the manuscript after the References section. Please note that tables should not in image format. All tables should have a concise title and should be numbered consecutively with Arabic numerals. If necessary, additional information should be given below the table.

**Figure Legend:** The figure legend should be typed on a separate page of the main manuscript and should include a short title and explanation. The legend should be concise but comprehensive and should be understood without referring to the text. Symbols used in figures must be explained. Any individually labeled figure parts or panels (A, B, *etc*.) should be specifically described by part name within the legend.

**Figure Preparation:** All figures should be clear and cited in numerical order in the text. Figures must fit a one- or two-column format on the journal page: 8.3 cm (3.3 in.) wide for a single column, 17.3 cm (6.8 in.) wide for a double column; maximum height: 24.0 cm (9.5 in.). Please make sure that artwork files are in an acceptable format (TIFF or JPEG) at minimum resolution (600 dpi for illustrations, graphs, and annotated artwork, and 300 dpi for micrographs and photographs). Please provide all figures as separate files. Please note that low-resolution images are one of the leading causes of article resubmission and schedule delays.

**Units and Symbols:** Units and symbols conforming to the International System of Units (SI) should be used for physicochemical quantities. Solidus notation (*e.g*. mg/kg, mg/mL, mol/mm$^2$/min) should be used. Please refer to the SI Guide *www.bipm.org/en/si/* for standard units.

**Supplemental data:** Supplemental data might be useful for supporting and enhancing your scientific research and *Drug Discoveries & Therapeutics* accepts the submission of these materials which will be only published online alongside the electronic version of your article. Supplemental files (figures, tables, and other text materials) should be prepared according to the above guidelines, numbered in Arabic numerals (*e.g*., Figure S1, Figure S2, and Table S1, Table S2) and referred to in the text. All figures and tables should have titles and legends. All figure legends, tables and supplemental text materials should be placed at the end of the paper. Please note all of these supplemental data should be provided at the time of initial submission and note that the editors reserve the right to limit the size

and length of Supplemental Data.

**7. Online Submission**

Manuscripts should be submitted to *Drug Discoveries & Therapeutics* online at *https://www.ddtjournal.com/login*. Receipt of your manuscripts submitted online will be acknowledged by an e-mail from Editorial Office containing a reference number, which should be used in all future communications. If for any reason you are unable to submit a file online, please contact the Editorial Office by e-mail at *office@ddtjournal.com*

**8. Accepted Manuscripts**

**Page Charge:** Page charges will be levied on all manuscripts accepted for publication in *Drug Discoveries & Therapeutics* (Original Articles / Brief Reports / Reviews / Policy Forum / Communications: $140 per page for black white pages, $340 per page for color pages; News / Letters: a total cost of $600).

**Misconduct:** *Drug Discoveries & Therapeutics* takes seriously all allegations of potential misconduct and adhere to the ICMJE Guideline (*https://icmje.org/recommendations*) and COPE Guideline (*https://publicationethics.org/files/Code_of_conduct_for_journal_editors.pdf*). In cases of suspected research or publication misconduct, it may be necessary for the Editor or Publisher to contact and share submission details with third parties including authors' institutions and ethics committees. The corrections, retractions, or editorial expressions of concern will be performed in line with above guidelines.

(As of August 2026)

**Drug Discoveries & Therapeutics**
Editorial and Head Office
Pearl City Koishikawa 603,
2-4-5 Kasuga, Bunkyo-ku,
Tokyo 112-0003, Japan.
E-mail: office@ddtjournal.com